Searches for Hadronization Modification in Small Collision Systems at the Large Hadron Collider Beauty Experiment

by

Desmond Mzamo Shangase

A dissertation submitted in partial fulfillment
of the requirements for the degree of
Doctor of Philosophy
(Physics)
in the University of Michigan
2025

Doctoral Committee:

Professor Christine Aidala, Chair
Professor Scott Haselschwardt
Professor Igor Jovanovic
Professor Chun Shen
Professor Junjie Zhu

Desmond Mzamo Shangase
dshangas@umich.edu
ORCID iD: 0000-0002-0287-6124

© Desmond Mzamo Shangase 2025

To Vusi, Dr. Nomava, A.C., and Alvinah Shangase
To Jules Loubeau

ACKNOWLEDGEMENTS

Listing all of the people responsible for getting me to the point where I could begin, let alone complete, this thesis would require me to double the length of this dissertation. Fortunately for the reader and unfortunately for me, I will have to select a few contributions to highlight here.

It should go without saying that the thesis advisor is central (an understatement) to the entire process. In addition to being my advisor, Christine Aidala has worn the hats of editor, co-proponent, advocate, and mentor while facilitating me through this degree process. Her passions for the physics of QCD, the scientific process, as well as conducting research honestly and thoroughly are not only admirable but contagious. I can say with confidence that my growth as a scientist would not have been nearly as rapid without our many discussions over the years; delving not only into the intricacies of nuclear and high-energy physics, but also the nuances of life as a researcher. For not only shepherding me through this incredibly tumultuous journey, but for also equipping me with the tools and vision to continue my growth as a physicist, she will always have my gratitude.

Given my description of Christine, it should be no surprise that the Aidala research group is constructed entirely of extremely motivated and thoughtful people. I have personally had extensive and insightful conversations with every member about our varied overlapping interests in and out of physics. The environment of the group is incredibly conducive to high-level research and scholarship without sacrificing a particularly friendly and supportive atmosphere. I will now highlight a few of the group members who mentored me throughout my time in the group. Jordan Roth and Kara Mattioli were the first members of the group I had met. Not only were their passion and enthusiasm major factors in my decision to join the group, but they continued to be valuable sources of knowledge to me along with our postdoctoral fellow Sookhyun Lee since we were all working on LHCb together. Despite losing Jordan in 2021, I still rely on his advice for my research and on his memory to keep me honest. Nicole Lewis and Joe Osborn helped me a great deal in my first years in the group with getting acclimated to research and the group structure. Nicole was my graduate student mentor, and gave me plenty of advice on classes, the degree process, and the city of Ann Arbor.

I have gotten the chance to cultivate strong friendships with my cohort members in the group (Dillon Fitzgerald and Cynthia Nuñez) as we managed to keep each other productive and sane throughout our degree processes. The community fostered in our cohort of physics graduate students as well as with students in the applied physics program has been pivotal in my mental well-being and allowed me to make the most of my time at the University of Michigan. It should also be noted that several student-led organizations helped provide community in addition to various resources for myself as well as other graduate students. These organizations include the Willie Hobbs Moore Chapter of the National Society of Black Physicists, the Graduate Employees Organization, the Community of Physicists for Inclusion and Equity, and others.

The LHCb collaboration is saturated with knowledgeable and welcoming people, particularly those that I have gotten to know in the Ions and Fixed Target working group (IFT). Working on an experiment at CERN had been a dream of mine since I was a student at Ramapo High School taking A.P. chemistry with Joanne Seche during the announcement of the Higgs Boson discovery. Teachers like Sharon Stephenson and Eileen Geiger fostered a work ethic that allowed me to step closer to that goal by getting into Stony Brook University. Alan Calder introduced me to the world of computational astrophysics (in additon to many programming tools that I rely on to this day) and was an extremely motivating research mentor who always reminded me to "shout him out when I eventually win a Nobel Prize". Thomas Hemmick introduced me to the world of QCD and got me started on the sPHENIX experiment, which I have had the pleasure of seeing evolve from the early R&D stages to a fully running experiment (that is currently taking data at RHIC). With the assistance of these people and many others, the dream of a 16-year-old from Rockland County, N.Y. has been realized.

On a personal note, I must thank the people that have been in my life throughout the entire doctoral process. I met Andrea Londoño when we were physics students at Stony Brook University. I have always had a susceptibility to workaholism, which Andrea has helped me manage. From finishing my undegraduate degree, to finishing my doctoral thesis, she has been instrumental in helping me maintain some level of work-life balance and without her I would have most likely burnt out before being able to complete this work. My greatest supporters have always been my family, in particular my sister Zama and my parents (Lee and Jocelyne). My parents have individually been through quite a lot in their lives, without considering the amount that was sacrificed to provide a stable household for me. They managed to emphasize the value of higher education and provide structure while still remaining open minded to my interests and passions. This dissertation is my meager attempt to repay them for their love and support.

Acknowledgment must be given to the National Science Foundation for funding the research presented in this dissertation. Further thanks to the Department of Physics at the University of Michigan. Additional thanks to the members of this doctoral committee, who were individually very accommodating and helpful.

TABLE OF CONTENTS

DEDICATION ii

ACKNOWLEDGEMENTS iii

LIST OF FIGURES viii

LIST OF TABLES xv

LIST OF APPENDICES xviii

LIST OF ACRONYMS xix

ABSTRACT xx

CHAPTER

1 Introduction 1

1.1 Quantum Chromodynamics 1
1.2 Factorization and Hadronization 3
1.2.1 Confinement 4
1.2.2 Hadronization 5
1.2.3 Factorization 5
1.3 The QCD phase diagram 7
1.3.1 Quark-Gluon Plasma 9
1.4 Modified Hadronization and Small Systems 13
1.4.1 Statistical Hadronization Model 13
1.4.2 Lund String Fragmentation 16
1.4.3 Evidence in Small Systems 18
1.5 Motivation and Objectives 20
1.5.1 Strangeness Enhancement 20
1.5.2 Baryon Enhancement 23

2 Experimental Setup 26

2.1 The Large Hadron Collider 26
2.2 The LHCb Experiment 27
2.2.1 Tracking 28
2.2.2 Calorimetry 30

2.2.3 Particle Identification . . . 30
2.2.4 Triggering . . . 32
2.2.5 Upgrades . . . 33

3 Description of Datasets . . . 37

3.1 Selection Criteria . . . 38
3.2 Monte-Carlo . . . 41

4 Analysis Details . . . 43

4.1 Event Activity Estimation . . . 43
4.1.1 Choice of Multiplicity Estimator . . . 43
4.2 Signal Extraction . . . 44
4.2.1 ϕ . . . 45
4.2.2 Λ & K^0_S . . . 45
4.2.3 π^+ & p . . . 48
4.3 Efficiencies and Corrections . . . 49
4.3.1 Particle Identification . . . 49
4.3.2 Tracking Performance Correction . . . 54
4.3.3 Corrections to Monte-Carlo . . . 55
4.3.4 Reconstruction and Selection Efficiency . . . 55
4.3.5 Acceptance Correction . . . 58
4.4 Systematic Uncertainties . . . 60
4.4.1 Signal Extraction . . . 60
4.4.2 Uncertainties from Efficiencies . . . 62
4.4.3 Acceptance Efficiency Systematics . . . 65

5 Results and Discussion . . . 66

5.1 Search for Strangeness Enhancement in pp at $\sqrt{s} = 13$ TeV . . . 72
5.2 Search for Baryon Enhancement in pp at $\sqrt{s} = 13$ TeV . . . 79
5.3 Discussion . . . 81
5.3.1 Agreement between Multiplicity Variables . . . 81
5.3.2 Experimental Comparisons . . . 82
5.3.3 Phenomenological Considerations . . . 89
5.3.4 Evidence for Medium Formation . . . 90
5.3.5 Prospective measurements . . . 91

6 Summary . . . 92

APPENDICES . . . 95

BIBLIOGRAPHY . . . 140

LIST OF FIGURES

FIGURE

1.1 Running of the QCD coupling constant, α_s, with respect to energy scale (1) . . 2
1.2 Deep scattering on a quark (*top*). s-channel quark-antiquark pair production. . 4
1.3 Factorized diagram for a hadron collision (h_a, h_b) which generates two new hadrons (h_1, h_2) via a hard scattering. 6
1.4 The phase diagram depicting the relative temperature and chemical potential (net baryon density) of various forms of QCD states(2) 7
1.5 Regions of the QCD phase diagram where constraints from heavy-ion collisions (HIC), lattice QCD (LQCD), perturbative QCD (pQCD), low-energy heavy-ion collisions (LENP), chiral effective field theory (CEFT), and astrophysics (neutron stars, NS) are available (3) 8
1.6 Schematic of a heavy-ion collision in which the impact parameter (b), participating, and spectating nucleons are depicted (4). 10
1.7 Illustration of a typical charged particle multiplicity distribution according to the Glauber model(5). The scales for average impact parameter (b(fm)) and average number of participating nucleons ($N_{\rm part}$) are also shown. 11
1.8 Collection of nuclear modification factor measurements of various particle species by the PHENIX experiment(6; 7). The direct photon results (Orange) are shown as a control since the direct photon production mechanism is independent of collision activity and QGP production. 12
1.9 Charged hadron nuclear modification factors measured by the ALICE experiment at high (Black) and low (Blue) event activity(8; 9). 12
1.10 Contributing Feynman diagrams for thermal quark production: a) pair production via s-channel quark annihilation b) gluon fusion pair production via t- (left), u- (center), and s- (right) channel(10) 14
1.11 Diagram of color reconnection between anti-parallel strings into either (Left) a new color topology, or (Right) string junctions(11). 17
1.12 Gradual enhancement in production with respect to charged pions ($\pi^+ + \pi^-$) in several hadrons of varying strangeness (12). 19
1.13 Observation of strangeness enhancement in B mesons from proton collisions in various transverse momentum bins(13). Comparisons are made to production ratios from non-hadronic collisions via the electroweak (dark blue) and bottom quark resonances (light blue). Monte Carlo predictions utilizing standard Lund String Fragmentation (green) and Color Recombination (red) are supplied. . . . 21

1.14 Observation of strangeness enhancement in D mesons from proton-lead collisions in various transverse momentum bins (black and red)(14). Comparisons are made to production ratios from ALICE (yellow and brown)(15; 16), integrated pp ratios from LHCb (green)(17), ALICE (cyan)(18) and e^+e^- (magenta)(19). Monte Carlo predictions utilizing standard Lund String Fragmentation (dashed red), Color Recombination (solid red), muti-parton interactions (solid blue), and coalescence (dashed blue) are supplied. 21
1.15 The measurement of various observables that are proportional to the relative probability of a b quark hadronizing into a strange vs non-strange meson in pp collision. The decay channel used to reconstruct the B meson, integrated luminosity of the dataset, and collision energy are provided for each measurement. 22
1.16 Baryon-to-meson ratios for charm (Circle), strange (Diamond), and light-flavored (Square) hadrons measured by the STAR experiment(20) 23
1.17 Baryon-to-meson ratio for bottom hadrons measured by the LHCb experiment (Blue)(21). The measurement from LEP (Pink) is provided as a reference(22). . 23
1.18 Baryon-to-meson ratio for protons and pions measured by the PHENIX experiment in various centrality Au+Au collisions and multiplicity-integrated pp collisions(23). 24

2.1 CERN Accelerator Complex as of 2022 26
2.2 Diagram of the LHCb experiment and sub-detectors during Runs I and II of the LHC (24) 28
2.3 Diagram of the R and Φ-type VELO sensors along with their corresponding sensing lines (25) 29
2.4 Diagram of various track types that can be reconstructed with the Run III LHCb detector along with the relevant tracking sub-detectors (26) 30
2.5 Cherenkov angle and track momentum correlation plots for muon and charged hadron tracks traversing the C_4F_{10} and aerogel radiators of RICH1. (27; 26) . . 31
2.6 Diagram of the LHCb experiment and sub-detectors during Runs III of the LHC (28) 33
2.7 Integrated luminosity recorded from pp collisions by the LHCb detector over the course of each year of operation(29) 34
2.8 Measurement of leakage current across several silicon layers in the TT detector. Leakage current is measured (Top) with respect to integrated LHC beam luminosity delivered to the LHCb detector and (Bottom) throughout Run II(30) 35
2.9 Exploded view of a module from the LHCb UT(31) 36

4.1 Multiplicity distributions of 2015 minibias events that meet the required primary vertex restriction. (Left) Backwards track distribution, (Right) VELO track distribution. 44
4.2 Representative simultaneous fit to the mass spectrum (left) and $\log \chi^2_{\mathrm{IP}}$ (right) distributions for ϕ candidates. The total fit (blue), prompt signal fit (green line), and background estimations (green shaded) are provided. 45
4.3 Example of a normalized $\log \chi^2_{\mathrm{IP}}$ distribution from the Λ mass background (Circles) and the corresponding KDE(32; 33; 34; 35) (Shaded). 47

4.4 Representative simultaneous fit to the mass spectrum (left) and $\log \chi^2_{\mathrm{IP}}$ (right) distributions for Λ candidates. The total fit (blue), prompt signal fit (green line), secondary signal fit (red shaded), and background estimations (green shaded) are provided. 47
4.5 Representative simultaneous fit to the mass spectrum (left) and $\log \chi^2_{\mathrm{IP}}$ (right) distributions for $\mathrm{K}^0_{\mathrm{S}}$ candidates. The total fit (blue), prompt signal fit (green line), secondary signal fit (red shaded), and background estimations (green shaded) are provided. 48
4.6 Representative plot of the mass distribution (left) and $\log \chi^2_{\mathrm{IP}}$ distribution (right) for $\pi^{\pm}$ candidates. The total fit (blue), prompt signal fit (green line), and secondary signal fit (red shaded) are provided. 49
4.7 Representative the $\log \chi^2_{\mathrm{IP}}$ distribution for p candidates. The total fit (blue), prompt signal fit (green line), and secondary signal fit (red shaded) are provided. 49
4.8 Particle identification efficiencies corresponding to the relevant charged pion cuts from section 3.1. 50
4.9 Particle identification efficiencies corresponding to the relevant proton cuts from section 3.1. 51
4.10 Particle identification efficiencies corresponding to the relevant charged kaon cuts from section 3.1. 52
4.11 Rebinned particle identification efficiencies for signal candidates matching the selection criteria written out in section 3.1. The listed species are the (Red) charged pion, (Dark Red) p, (Cyan) $\mathrm{K}^0_{\mathrm{S}}$, (Blue) Λ, and (Violet) ϕ 53
4.12 Table of tracking efficiency corrections for $2 \leq \eta_{\mathrm{track}} \leq 5$ and $2\ \mathrm{GeV}/c \leq p_{\mathrm{track}} \leq 200\ \mathrm{GeV}/c$ in MagDown pp collisions from 2015. 54
4.13 Table of tracking efficiency corrections for $2 \leq \eta_{\mathrm{track}} \leq 5$ and $2\ \mathrm{GeV}/c \leq p_{\mathrm{track}} \leq 200\ \mathrm{GeV}/c$ in MagUp pp collisions from 2015. 55
4.14 Reconstruction and selection efficiencies for signal candidates matching the selection criteria written out in section 3.1. The listed species are the (Red) charged pion, (Dark Red) p, (Cyan) $\mathrm{K}^0_{\mathrm{S}}$, (Blue) Λ, and (Violet) ϕ 57
4.15 Acceptance efficiencies for signal candidates matching the selection criteria written out in section 3.1. The listed species are (Cyan) $\mathrm{K}^0_{\mathrm{S}}$, (Blue) Λ, and (Violet) ϕ 59
4.16 Relative systematic errors originating from the fits to the mass and/or $\log \chi^2_{\mathrm{IP}}$ distributions. The listed species are the (Red) charged pion, (Dark Red) p, (Cyan) $\mathrm{K}^0_{\mathrm{S}}$, (Blue) Λ, and (Violet) ϕ 61
4.17 Relative systematic errors originating from final state tracking corrections. The listed species are the (Red) charged pion, (Dark Red) p, (Cyan) $\mathrm{K}^0_{\mathrm{S}}$, (Blue) Λ, and (Violet) ϕ 63
4.18 Relative systematic errors originating from the uncertainties on the particle identification efficiency from PIDCalib. The listed species are the (Red) charged pion, (Dark Red) p, (Cyan) $\mathrm{K}^0_{\mathrm{S}}$, (Blue) Λ, and (Violet) ϕ 64
4.19 Relative systematic errors originating from the uncertainties on the Monte-Carlo acceptance fractions for signal candidates. The listed species are (Cyan) $\mathrm{K}^0_{\mathrm{S}}$, (Blue) Λ, and (Violet) ϕ 65

5.1 Multiplicity-dependent per-event yields of prompt charged pions with respect to (left) backwards tracks and (right) all VELO tracks. 66
5.2 Multiplicity-dependent per-event yields of prompt protons with respect to (left) backwards tracks and (right) all VELO tracks. 67
5.3 Multiplicity-dependent per-event yields of prompt K^0_S mesons with respect to (left) backwards tracks and (right) all VELO tracks. 68
5.4 Multiplicity-dependent per-event yields of prompt Λs with respect to (left) backwards tracks and (right) all VELO tracks. 69
5.5 Multiplicity-dependent per-event yields of prompt ϕ mesons with respect to (left) backwards tracks and (right) all VELO tracks. 70
5.6 Combined multiplicity-dependent per-event yields of prompt hadrons with respect to (left) backwards tracks and (right) all VELO tracks. The listed species are the (Red) charged pion, (Dark Red) p, (Cyan) K^0_S, (Blue) Λ, (Violet) ϕ and the corresponding antiparticles. 71
5.7 Multiplicity-dependent $\frac{K^0_S}{\pi^+ + \pi^-}$ yield ratios with respect to (left) backwards tracks and (right) all VELO tracks. 73
5.8 Multiplicity-dependent $\frac{\Lambda + \bar{\Lambda}}{\pi^+ + \pi^-}$ yield ratios with respect to (left) backwards tracks and (right) all VELO tracks. 74
5.9 Multiplicity-dependent $\frac{\Lambda + \bar{\Lambda}}{p + \bar{p}}$ yield ratios with respect to (left) backwards tracks and (right) all VELO tracks. 75
5.10 Multiplicity-dependent $\frac{\phi}{\pi^+ + \pi^-}$ yield ratios with respect to (left) backwards tracks and (right) all VELO tracks. 76
5.11 Summary of strangeness production ratios to charged pions in pp collisions at $\sqrt{s} = 13$ TeV. The listed species are (Cyan) K^0_S, (Blue) Λ, (Violet) ϕ and the corresponding antiparticles. 77
5.12 Multiplicity-dependent $\frac{p + \bar{p}}{\pi^+ + \pi^-}$ yield ratios with respect to (left) backwards tracks and (right) all VELO tracks. 79
5.13 Combined multiplicity-dependent baryon-to-meson ratios with respect to (left) backwards tracks and (right) all VELO tracks. The listed species are the (Dark Red) p and (Blue) Λ along with the corresponding antiparticles. 80
5.14 Correlation between all VELO tracks and backwards VELO tracks in minimum bias collider events. 81
5.15 Yield ratios to charged pions for (Dark Red) p, (Cyan) K^0_S, (Blue) Λ, (Violet) ϕ binned by multiplicity class. Results with respect to N_{BACK} (solid, filled) and N_{VELO} (open, dashed) are shown. 82
5.16 Absolute (left) and normalized (right) multiplicity-dependent (Dark Red) $\frac{p + \bar{p}}{\pi^+ + \pi^-}$ yield ratios with respect to charged track density. Results with respect to N_{BACK} (solid, filled) and N_{VELO} (open, dashed) are provided along with results from ALICE(12) (Black) in pp collisions at $\sqrt{s} = 13$ TeV. 84
5.17 Absolute (left) and normalized (right) multiplicity-dependent (Cyan) $\frac{K^0_S}{\pi^+ + \pi^-}$ yield ratios with respect to charged track density. Results with respect to N_{BACK} (solid, filled) and N_{VELO} (open, dashed) are provided along with results from ALICE(12) (Black) in pp collisions at $\sqrt{s} = 13$ TeV. 85

5.18 Absolute (left) and normalized (right) multiplicity-dependent (Blue) $\frac{\Lambda+\bar{\Lambda}}{\pi^+ + \pi^-}$ yield ratios with respect to charged track density. Results with respect to N_{BACK} (solid, filled) and N_{VELO} (open, dashed) are provided along with results from ALICE(12) (Black) in pp collisions at $\sqrt{s} = 13$ TeV. 86
5.19 Absolute (left) and normalized (right) multiplicity-dependent (Violet) $\frac{\phi}{\pi^+ + \pi^-}$ yield ratios with respect to charged track density. Results with respect to N_{BACK} (solid, filled) and N_{VELO} (open, dashed) are provided along with results from ALICE(15) (Black) in pp collisions at $\sqrt{s} = 7$ TeV. 87
5.20 Baryon-to-meson ratios measured by BRAHMS at various pseudorapidities(36). Ratios between protons and π^+ (left) as well as antiprotons and π^- (right) are shown in central Au + Au (blue filled square), peripheral Au + Au (green empty square), and multiplicity-integrated pp (red triangle) collisions at $\sqrt{s_{\mathrm{NN}}} = 200$ GeV. 88
5.21 Simulations of string fragmentations in Pythia for pp (top), pPb (middle), and PbPb (bottom) collisions. The charged track multiplicity increases to the right, and the value of the effective string constant relative to the nominal string constant is represented by the colormap(37). 90

6.1 Summary of strangeness and baryon enhancement results in pp collisions at $\sqrt{s}$ = 13 TeV from Run II LHCb data. Yield ratios with respect to charged pions are displayed with respect to (left) backwards tracks and (right) all VELO tracks. The listed species are (Dark Red) p, (Cyan) $\mathrm{K}^0_{\mathrm{S}}$, (Blue) Λ, (Violet) ϕ and the corresponding antiparticles. 93

D.1 Rebinned particle identification efficiencies for pion candidates matching the selection criteria written out in section 3.1. 103
D.2 Rebinned particle identification efficiencies for proton candidates matching the selection criteria written out in section 3.1. 104
D.3 Rebinned particle identification efficiencies for Λ candidates with daughter particles matching the selection criteria written out in section 3.1. 105
D.4 Rebinned particle identification efficiencies for $\mathrm{K}^0_{\mathrm{S}}$ candidates with daughter particles matching the selection criteria written out in section 3.1. 106
D.5 Rebinned particle identification efficiencies for ϕ candidates with daughter particles matching the selection criteria written out in section 3.1. 107
D.6 Reconstruction and selection efficiencies corresponding to the relevant π^+ cuts from section 3.1. 108
D.7 Reconstruction and selection efficiencies corresponding to the relevant p cuts from section 3.1. 109
D.8 Reconstruction and selection efficiencies corresponding to the relevant Λ cuts from section 3.1. 110
D.9 Reconstruction and selection efficiencies corresponding to the relevant $\mathrm{K}^0_{\mathrm{S}}$ cuts from section 3.1. 111
D.10 Reconstruction and selection efficiencies corresponding to the relevant ϕ cuts from section 3.1. 112

D.11 Acceptance efficiencies corresponding to the daughter track geometric and kinematic distributions for Λ candidates. . . . 113
D.12 Acceptance efficiencies corresponding to the daughter track geometric and kinematic distributions for K^0_S candidates. . . . 114
D.13 Acceptance efficiencies corresponding to the daughter track geometric and kinematic distributions for ϕ candidates. . . . 115

E.1 Relative systematic errors originating from the fits to the charged pion $\log\chi^2_{IP}$ distributions. . . . 117
E.2 Relative systematic errors originating from the fits to the p $\log\chi^2_{IP}$ distributions. 118
E.3 Relative systematic errors originating from the fits to the Λ mass and $\log\chi^2_{IP}$ distributions. . . . 119
E.4 Relative systematic errors originating from the fits to the K^0_S mass and $\log\chi^2_{IP}$ distributions. . . . 120
E.5 Relative systematic errors originating from the fits to the ϕ mass and $\log\chi^2_{IP}$ distributions. . . . 121
E.6 Relative systematic errors originating from the uncertainties on the tracking efficiency corrections from TrackCalib. . . . 122
E.7 Relative systematic errors originating from the uncertainties on the tracking efficiency corrections from TrackCalib. . . . 123
E.8 Relative systematic errors originating from the uncertainties on the tracking efficiency corrections from TrackCalib. . . . 124
E.9 Relative systematic errors originating from the uncertainties on the tracking efficiency corrections from TrackCalib. . . . 125
E.10 Relative systematic errors originating from the uncertainties on the tracking efficiency corrections from TrackCalib. . . . 126
E.11 Relative systematic errors originating from the uncertainties on the particle identification efficiency from PIDCalib. . . . 127
E.12 Relative systematic errors originating from the uncertainties on the particle identification efficiency from PIDCalib. . . . 128
E.13 Relative systematic errors originating from the uncertainties on the particle identification efficiency from PIDCalib. . . . 129
E.14 Relative systematic errors originating from the uncertainties on the particle identification efficiency from PIDCalib. . . . 130
E.15 Relative systematic errors originating from the uncertainties on the particle identification efficiency from PIDCalib. . . . 131
E.16 Relative systematic errors originating from the uncertainties on the Monte-Carlo acceptance fractions for Λ candidates. . . . 132
E.17 Relative systematic errors originating from the uncertainties on the Monte-Carlo acceptance fractions for K^0_S candidates. . . . 133
E.18 Relative systematic errors originating from the uncertainties on the Monte-Carlo acceptance fractions for ϕ candidates. . . . 134

F.1 Absolute (left) and normalized (right) multiplicity-dependent (Dark Red) $\frac{\mathrm{p}+\bar{\mathrm{p}}}{\pi^+ + \pi^-}$ yield ratios with respect to multiplicity percentile. Results with respect to N_{BACK} (solid, filled) and N_{VELO} (open, dashed) are provided along with results from ALICE(12) (Black) in pp collisions at $\sqrt{s} = 13$ TeV. Charged track density and average event activity is increasing from left to right. 136

F.2 Absolute (left) and normalized (right) multiplicity-dependent (Cyan) $\frac{\mathrm{K}^0_{\mathrm{S}}}{\pi^+ + \pi^-}$ yield ratios with respect to multiplicity percentile. Results with respect to N_{BACK} (solid, filled) and N_{VELO} (open, dashed) are provided along with results from ALICE(12) (Black) in pp collisions at $\sqrt{s} = 13$ TeV. Charged track density and average event activity is increasing from left to right. 137

F.3 Absolute (left) and normalized (right) multiplicity-dependent (Blue) $\frac{\Lambda+\bar{\Lambda}}{\pi^+ + \pi^-}$ yield ratios with respect to multiplicity percentile. Results with respect to N_{BACK} (solid, filled) and N_{VELO} (open, dashed) are provided along with results from ALICE(12) (Black) in pp collisions at $\sqrt{s} = 13$ TeV. Charged track density and average event activity is increasing from left to right. 138

F.4 Absolute (left) and normalized (right) multiplicity-dependent (Cyan) $\frac{\phi}{\pi^+ + \pi^-}$ yield ratios with respect to multiplicity percentile. Results with respect to N_{BACK} (solid, filled) and N_{VELO} (open, dashed) are provided along with results from ALICE(15) (Black) in pp collisions at $\sqrt{s} = 7$ TeV. Charged track density and average event activity is increasing from left to right. 139

LIST OF TABLES

TABLE

3.1 Selection criteria for non-decaying particle candidates. 38
3.2 Summary of Minimum Bias candidates passing the initial reconstruction and selection criteria. 42

4.1 Definitions of multiplicity classes with respect to the multiplicity estimators N_{BACK} and N_{VELO}. The corresponding event activity percentiles and average charged track multiplicities per class are provided. 44
4.2 Summary of representative particle identification efficiencies for signal candidates. The provided efficiencies are for the dataset taken with downward magnet polarity and with respect to N_{BACK} specifically. The complete summary of efficiencies is provided in appendix D. 53
4.3 Summary of representative reconstruction and selection efficiencies for signal candidates. The provided efficiencies are for the dataset taken with downward magnet polarity and with respect to N_{BACK} specifically. The complete summary of efficiencies is provided in appendix D. 57
4.4 Summary of representative acceptance efficiencies for signal candidates. The provided efficiencies are for the dataset taken with downward magnet polarity and with respect to N_{BACK} specifically. The complete summary of efficiencies is provided in appendix D. 59
4.5 Summary of representative systematic uncertainties originating from the fit templates for signal candidates. The provided uncertainties are for the dataset taken with downward magnet polarity and with respect to N_{BACK} specifically. The complete summary of systematic uncertainties is provided in appendix E. 61
4.6 Summary of representative systematic uncertainties originating from tracking efficiency corrections provided by TrackCalib. The provided uncertainties are for the dataset taken with downward magnet polarity and with respect to N_{BACK} specifically. The complete summary of systematic uncertainties is provided in appendix E. 63
4.7 Summary of representative systematic uncertainties originating from particle identification efficiencies provided by PIDCalib. The provided uncertainties are for the dataset taken with downward magnet polarity and with respect to N_{BACK} specifically. The complete summary of systematic uncertainties is provided in appendix E. 64

4.8 Summary of representative systematic errors originating from uncertainties on daughter acceptance fractions. The provided efficiencies are for the dataset taken with downward magnet polarity and with respect to N_{BACK} specifically. The complete summary of efficiencies is provided in appendix E. 65

A.1 Summary of corrected yields for signal species with respect to multiplicity (relevant antiparticles are included). For each entry, the first error is from the statistical uncertainty and the second error is from the systematic uncertainty. . 96
A.2 Summary of corrected yields for signal species with respect to multiplicity (relevant antiparticles are included). For each entry, the first error is from the statistical uncertainty and the second error is from the systematic uncertainty. . 97

B.1 Summary of corrected yields per event for signal species with respect to multiplicity (relevant antiparticles are included). For each entry, the first error is from the statistical uncertainty and the second error is from the systematic uncertainty. 99
B.2 Summary of corrected yields per event for signal species with respect to multiplicity (relevant antiparticles are included). For each entry, the first error is from the statistical uncertainty and the second error is from the systematic uncertainty.100

C.1 Summary of corrected yield ratios to charged pions for signal species with respect to multiplicity (relevant antiparticles are included). For each entry, the first error is from the statistical uncertainty and the second error is from the systematic uncertainty. 101
C.2 Summary of corrected yield ratios to charged pions for signal species with respect to multiplicity (relevant antiparticles are included). For each entry, the first error is from the statistical uncertainty and the second error is from the systematic uncertainty. 102

D.1 Summary of particle identification efficiencies for charged pions. 104
D.2 Summary of particle identification efficiencies for protons. 105
D.3 Summary of particle identification efficiencies for reconstructed Λ candidates. . 106
D.4 Summary of particle identification efficiencies for reconstructed $\mathrm{K}^0_{\mathrm{S}}$ candidates. . 107
D.5 Summary of particle identification efficiencies for reconstructed ϕ candidates. . 108
D.6 Summary of Reconstruction and Selection Efficiencies for π candidates. 109
D.7 Summary of Reconstruction and Selection Efficiencies for p candidates. 110
D.8 Summary of Reconstruction and Selection Efficiencies for Λ candidates. 111
D.9 Summary of Reconstruction and Selection Efficiencies for $\mathrm{K}^0_{\mathrm{S}}$ candidates. 112
D.10 Summary of Reconstruction and Selection Efficiencies for ϕ candidates. 113
D.11 Summary of Acceptance Efficiencies for Λ candidates. 114
D.12 Summary of Acceptance Efficiencies for $\mathrm{K}^0_{\mathrm{S}}$ candidates. 115
D.13 Summary of Acceptance Efficiencies for ϕ candidates. 116

E.1 Summary of systematic errors from pion candidate signal extraction. 118
E.2 Summary of systematic errors from p candidate signal extraction. 119
E.3 Summary of systematic errors from Λ candidate signal extraction. 120
E.4 Summary of systematic errors from $\mathrm{K}^0_{\mathrm{S}}$ candidate signal extraction. 121
E.5 Summary of systematic errors from ϕ candidate signal extraction. 122

E.6 Summary of systematic errors corresponding to tracking corrections on π^+ Long Tracks. . . . 123
E.7 Summary of systematic errors corresponding to tracking corrections on p Long Tracks. . . . 124
E.8 Summary of systematic errors corresponding to tracking corrections on Λ candidates from the p and π^+ daughters. . . . 125
E.9 Summary of systematic errors corresponding to tracking corrections on K^0_S candidates from the charged pion daughters. . . . 126
E.10 Summary of systematic errors corresponding to tracking corrections on ϕ candidates from the charged kaon daughters. . . . 127
E.11 Summary of systematic errors corresponding to PID efficiencies on π^+ candidates. 128
E.12 Summary of systematic errors corresponding to PID efficiencies on p candidates. 129
E.13 Summary of systematic errors corresponding to PID efficiencies on Λ candidates from the p and π^+ daughters. . . . 130
E.14 Summary of systematic errors corresponding to PID efficiencies on K^0_S candidates from the π^+ and π^- daughters. . . . 131
E.15 Summary of systematic errors corresponding to PID efficiencies on ϕ candidates from the K^+ and K^- daughters. . . . 132
E.16 Summary of systematic errors originating from uncertainties on p and π^+ daughter acceptance fractions. . . . 133
E.17 Summary of systematic errors originating from uncertainties on π^+ and π^- daughter acceptance fractions. . . . 134
E.18 Summary of systematic errors originating from uncertainties on K^+ and K^- daughter acceptance fractions. . . . 135

LIST OF APPENDICES

A Summary of Yields **95**

B Summary of Yields per Event **98**

C Summary of Ratios **101**

D Summary of Efficiencies **103**

E Summary of Systematic Uncertainties **117**

F ALICE Comparison Plots With Respect to Multiplicity Percentile **136**

LIST OF ACRONYMS

LHC Large Hadron Collider

LHCb Large Hadron Collider Beauty Experiment

ALICE A Large Ion Collider Experiment

CERN Organisation Européenne pour la Recherche Nucléaire (tl. *European Organization for Nuclear Research*)

RHIC Relativistic Heavy Ion Collider

STAR Solenoidal Tracker At RHIC

PHENIX Pioneering High Energy Nuclear Interaction Experiment

LEP Large Electron-Positron Collider

QCD Quantum Chromodynamics

QED Quantum Electrodynamics

QGP Quark-Gluon Plasma

PDF Parton Distribution Function

FF Fragmentation Function

TMD Transverse Momentum Dependent-Distribution

MeV Mega Electron-Volts

GeV Giga Electron-Volts

TeV Tera Electron-Volts

IP Impact Parameter

PID Particle Identification

RICH Ring-Imaging Cherenkov Detector

ABSTRACT

Due to a variety of experimental results over the past decade, historical assumptions regarding particle production and QCD emergent phenomena in hadron collisions have come under scrutiny. Hadronization effects that have been tightly associated with QCD phase transitions expected exclusively in heavy-ion collisions (e.g. Pb-Pb) have been observed in the smallest and simplest of the hadronic collision systems, proton-proton collisions. Strangeness enhancement and baryon enhancement are among the modified hadronization signatures in which pp collisions were initially used as null-hypothesis measurements. In this thesis, a suite of light-flavor hadronic species of varying strangeness are used to measure strangeness and baryon enhancement using minimum bias data from pp collisions at $\sqrt{s} = 13$ TeV recorded by the LHCb detector. Track-multiplicity-dependent particle ratios between proton, K^0_S, ϕ, and Λ yields to charged pion yields are calculated and display a positive correlation with event activity. Due to the unique geometry and layout of the LHCb spectrometer, two multiplicity estimators were used to characterize the abundance of tracks in the backwards (N_{BACK}) and inclusive (N_{VELO}) LHCb pseudorapidity acceptance in order to probe hadronization dependencies on global or local event activity respectively. Unlike in previous measurements in heavy-flavor species, no significant discrepancies in trends are observable between the two activity estimators for either strangeness enhancement or baryon enhancement. This supports the conclusion that for specifically light-flavor hadrons in small-systems, the hadronization mechanism(s) at play are equally dependent on global and local event activity. Through comparisons with results at midrapidity it is established that the rate of enhancement with respect to event activity is not significantly dependent on pseudorapidity. It is also observed that the relative statistics of strange hadrons to charged pions is significantly suppressed at forward rapidity, whereas protons display a relative enhancement. These findings are consistent with a coalescence framework in which proton and Λ hadronization are dominated by kinematic and chemical effects respectively.

CHAPTER 1

Introduction

1.1 Quantum Chromodynamics

The stability of non-radioactive nuclei as well as the observation of particle decays with very fast characteristic times required the existence of a strong nuclear force, which could generate an attractive potential between nucleons at hadronic length scales ($O(1 \sim 10)$ fm) and also account for scattering interactions at short distances and high energy. Following the postulation of quarks, which are also bound together by this force, three types of charges for this force to interact with were necessitated by the observation of particular baryons (e.g. Ω^-, Δ^{++}) that would be impossible to form otherwise due to Pauli exclusion. To describe this force, a quantum field theory based on three distinct *color* charges (as opposed to one charge in electromagnetism) was developed and named Quantum Chromodynamics, or QCD. Like the other field theories of the standard model, QCD is described by a lagrangian:

$$\mathcal{L}_{QCD} = \bar{\psi}(i\gamma^\mu D_\mu - m)\psi - \frac{1}{4}G^a_{\mu\nu}G^{\mu\nu}_a \tag{1.1}$$

The first portion of the lagrangian is reminiscent of the other standard model field theories as it encodes the mass, kinematic and field interaction terms for spin-1/2 fermions (ψ); in this case, quarks and antiquarks. The uniqueness of QCD comes when the second portion describing the field strength is expanded as follows:

$$G^a_{\mu\nu} = \partial_\mu A^a_\nu - \partial_\nu A^a_\mu + g f^{abc} A^b_\mu A^c_\nu \tag{1.2}$$

Here, A_μ represents the field and therefore the carrier for the strong nuclear force, the gluon. The g term is the coupling strength for QCD and f^{abc} is the structure coefficient for

the Lie Group corresponding to QCD, SU(3). Rewriting the field strength tensor in terms of the field vectors produces terms proportional to A^2, A^3, and A^4, thus allowing for up to 4-gluon interaction vertices in QCD. This is possible due to the gluons carrying color charge themselves and therefore being capable of self-interaction at first order.

The number of color charges and thus the self-interacting nature of the field has an effect on how the interaction strength, or coupling constant, evolves with energy and distance scales. Unlike in electromagnetism and the weak nuclear force, the coupling constant for the strong force (α_s) decreases significantly with energy (see Figure 1.1). This uniquely negative slope for the strong force among the Standard Model theories is the result of the renormalization group evolution (or β-function) for a field theory of type SU(N) with three (or more) fundamental charges(38; 39). Consequently, QCD is the only force in the Standard Model to experience *asymptotic freedom* at high energies, in which quark and gluon dynamics increasingly approach the behavior of free particles at increasing energy scales. The explicit β-function for QCD is provided in equation 1.3, in which μ, N_c, and N_f represent the energy scale, the number of colors (3), and the number of quark flavors respectively.

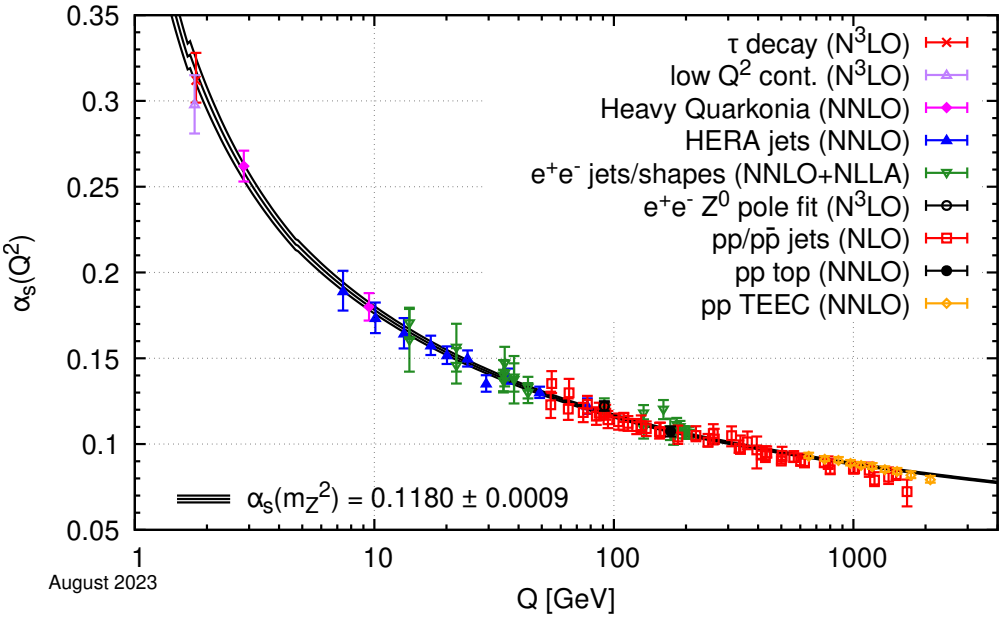


Figure 1.1: Running of the QCD coupling constant, α_s, with respect to energy scale (1)

$$\beta(\alpha_s) = \frac{d\alpha_s}{d\,\ln(\mu^2)} = \frac{\alpha_s}{4\pi}\left(-\frac{11}{3}N_c\ +\ \frac{2}{3}N_f\right) \tag{1.3}$$

This means that at high energy, quark and gluon interactions are easily calculable and the application of perturbation theory is more obviously appropriate. However, when taking the low-energy limit the coupling constant diverges dramatically and perturbation theory calculations are no longer reasonable. α_s enters this non-perturbative regime when the relevant energy scale decreases below Λ_{QCD} (between approximately 90 MeV to 340 MeV based on the number of interacting quark species considered). This poses an interesting problem for understanding the structure and formation of hadrons since these are low energy scale processes and thus governed by non-perturbative QCD. The solution for understanding how to depict high energy hadronic processes (i.e. hadron collisions) is called factorization and will be discussed in the following section.

1.2 Factorization and Hadronization

In high-energy hadronic collisions like the interactions that take place at the Large Hadron Collider, LHC, non-perturbative dynamics play a significant role in the initial and final states. As alluded to earlier, non-perturbative dynamics govern the behavior of gluons and quarks in the hadron interior. For a hard scattering to occur, two partons (quark or gluon constituent to a hadron) from the colliding hadrons must come into contact. The type of hard scattering process is largely determined by the species and kinematics of the participating partons, thus the kinematic distributions for each of the quark and gluon species inside the hadron can significantly suppress or enhance the probabilities of particular processes. The dynamics interior to a hadron are governed by non-perturbative QCD interactions and any estimation of the parton distributions must be done by either non-analytic calculations (this method is referred to as Lattice QCD) or extraction from experimentally derived cross-sections.

Additionally, non-perturbative effects are also at play if the interaction(s) result in the ejection of a parton from one of the hadronic species or the generation of new color charged objects. It has been observed that free color charges, while allowable in the field theory of QCD, are not found in reality due to a phenomenon known as confinement.

1.2.1 Confinement

The QCD potential is constructed of two components. One component is analogous to the Coulombic potential in electromagnetism and is inversely proportional to the distance between charges.

$$V_{QCD,\text{Coulomb}} \sim -\frac{\alpha_s}{r} \tag{1.4}$$

Due to the self-interacting nature of the QCD force carrier, the strong nuclear force field lines concentrate between the source charges. By mostly restricting the field to one spatial dimension, the potential energy stored in said field increases with size along this axis and generates an elastic potential. It then becomes convenient to represent the connection between source charges as *Lund strings*, with some Hooke's constant κ.

$$V_{QCD,\text{Elastic}} \sim \kappa \cdot r \tag{1.5}$$

From this potential it can be ascertained that following either a hard scattering with a parton or a quark-antiquark pair creation process (depicted in Figure 1.2), it would take infinite energy to completely separate the color charges involved.

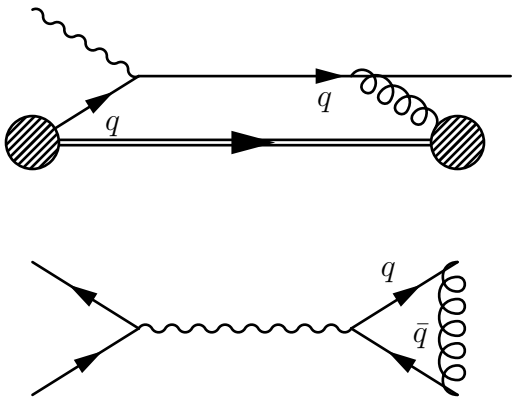


Figure 1.2: Deep scattering on a quark (*top*). s-channel quark-antiquark pair production.

In these cases, the charges either recombine into a single, color-neutral bound state or new bound states are generated.

1.2.2 Hadronization

In particularly energetic parton interactions, the potential energy stored in the field between two charges before restorative forces take over can grow to be significantly larger than the masses of the charges. It then becomes energetically favorable for the field to produce two new charges via gluon splitting to disconnect the field lines between the initial charges, thus generating two new neutral states. The splitting of these field lines can be represented by the rupturing of Lund strings into fragments (40; 41), and is appropriately named *fragmentation*. The scenario that was just described is the simplest picture of *hadronization*, or the process of generating new hadrons, and is often seen in non-hadronic collisions when quark-antiquark pairs are produced. It should be noted that the term 'hadronization' is often used in two senses.

1. The explicitly non-perturbative process by which high-momentum quarks join into bound states. This depiction is motivated by existence of fragmentation functions (to be discussed in section 1.2.3), which encode the probabilities of escaping partons generating particular hadronic final states into matrix element calculations. It is important to note that in this picture, hadronization does not depict the generation of new color charges and thus fragmentation is considered a precursor to hadronization rather than a stage in the process.

2. The entire process by which new hadrons are generated following a collision. This includes the previous definition in addition to any process which generates new color charges (e.g. Lund string fragmentation). This definition is more useful in situations where particular areas of the QCD phase diagram are being probed and new quark generating processes might be at play.

As will be discussed towards the end of this chapter, the processes that are of interest to the analyses undergone concern the generation of new color charges in addition to their combination into hadronic final states. Thus, for the purposes of this dissertation, the default definition will be the latter unless explicitly stated otherwise.

1.2.3 Factorization

The choice of definition for the term 'hadronization' in this dissertation is also motivated by *factorization* and its applicability in varying collisions. Factorization is the solution to simultaneously representing perturbative and non-perturbative processes when calculating cross-sections for events in hadron collisions. This is accomplished by modeling the parton content of the hadronic initial and final states probabilistically. As discussed earlier,

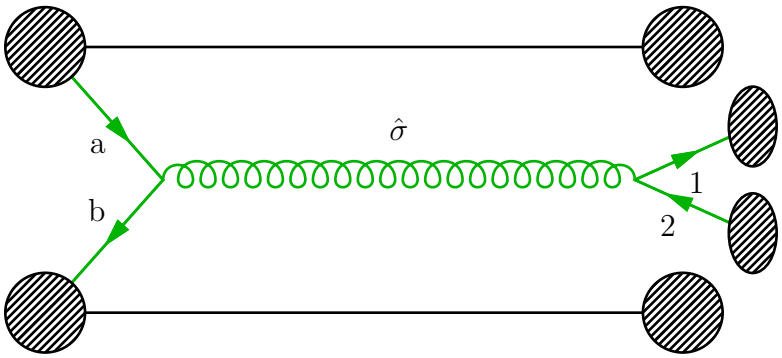


Figure 1.3: Factorized diagram for a hadron collision (h_a, h_b) which generates two new hadrons (h_1, h_2) via a hard scattering.

kinematic distributions for specific parton species can be estimated by measuring the cross-section of particular scattering processes. The distributions calculated by this method are called *parton distribution functions* (PDFs) and will be represented as $f(x)_{p/h}$, where f encodes (at leading order) the probability distribution of finding a parton p in hadron h carrying momentum fraction x ($x = \frac{p_p}{p_h}$). The particles entering the hard scattering process can be interpreted as stochastically selected partons based on the distribution functions of the hadronic initial states.

The method for characterizing the final state is effectively identical. Cross-sections have been measured for various scattering processes and collected across several collision systems in order to extract probability distributions for hadrons emerging out of particular quarks or gluons. This generates the *fragmentation functions* (FFs) discussed earlier which will be represented as $D(z)_{h'/p'}$, where D encodes the probability distribution of a parton p' hadronizing into hadron h' carrying momentum fraction z ($z = \frac{p'_h}{p'_p}$).

With this prescription, the hard scattering process (represented by $\hat{\sigma}$ in the diagram) is calculated analytically via perturbation theory and the initial and/or final hadronic states can be represented probabilistically based on experimental data. Generally, a full hadronic cross-section can be calculated by the following.

$$\sigma_{total} = \int dx_a dx_b \int dz_1 dz_2 f(x_a)_{p/h,a} f(x_b)_{p/h,b} \cdot \hat{\sigma}_{a,b\to 1,2} \cdot D(z_1)_{h/p,1} D(z_2)_{h/p,2} \tag{1.6}$$

This methodology is generally very successful for calculating cross-sections for hadron collider events, however there are scenarios in which the stages of a collision cannot be neatly segmented and the assumption of a factorized picture is inappropriate.

Depending on the parton density and energy of the initial state, different processes for

parton (and ultimately hadron) generation can occur. The purpose of this thesis is to investigate the presence or absence of such processes and is ultimately the primary factor in the choice of hadronization definition from section 1.2.2. A partial, theoretical understanding of which processes may be at play in a particular collision can be accomplished by mapping the initial state of said interaction onto the *QCD phase diagram*.

1.3 The QCD phase diagram

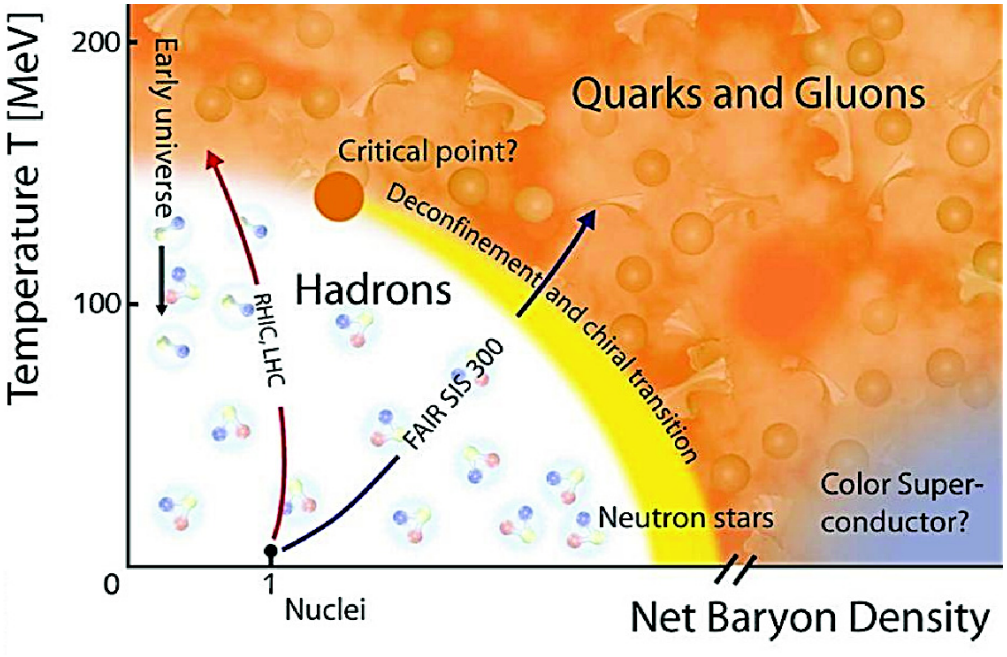


Figure 1.4: The phase diagram depicting the relative temperature and chemical potential (net baryon density) of various forms of QCD states(2)

Depicted in Figure 1.4 are the approximate locations in temperature-potential space of some forms of QCD-sensitive matter. It should be known that the exact structure and granularity of the phase diagram is yet to be verified, therefore the example provided is non-exhaustive of the potential phases of QCD matter and the location of particular transition regions should be considered estimations. It is important to note that several different choices of axes to represent the QCD phase diagram exist. Net baryon density, net quark density, baryochemical potential (μ_B), and quark chemcial potential (μ_Q), while technically different system observables, are strongly correlated and mappable onto each other, thus they can be used interchangeably when depicting the phase diagram. These variables all map onto the effective QCD potential in a system related to the net abundance of baryons or quarks as

opposed to antibaryons or antiquarks. Zero chemical potential (or net density) is approached when a system is either sparse of QCD matter or is in equilibrium between QCD matter and antimatter.

The approximate areas in which the phase diagram can be characterized are shown in Figure 1.5. It can be seen that events in hadron colliders may cover a breadth of the low potential region (low with respect to the net densities found in neutron stars) and temperatures ranging from standard hadronic matter to beyond the deconfinement transition. It is in this realm of the phase diagram that the new parton production mechanisms alluded to in section 1.2.3 can be found.

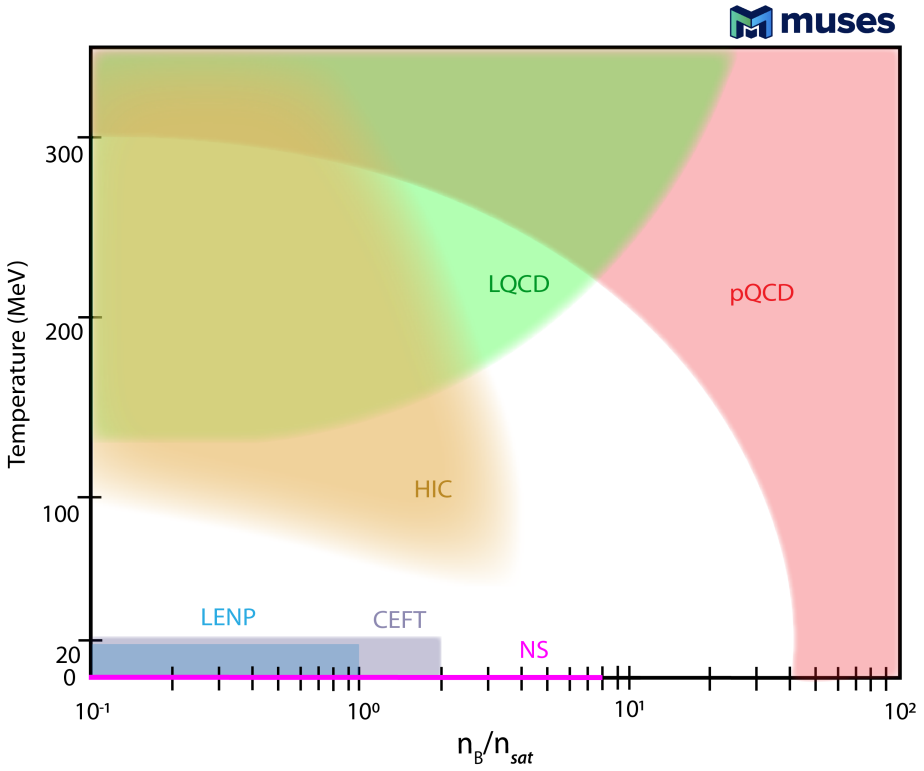


Figure 1.5: Regions of the QCD phase diagram where constraints from heavy-ion collisions (HIC), lattice QCD (LQCD), perturbative QCD (pQCD), low-energy heavy-ion collisions (LENP), chiral effective field theory (CEFT), and astrophysics (neutron stars, NS) are available (3)

1.3.1 Quark-Gluon Plasma

The deconfinement transition refers to a system in which non-perturbative effects such as confinement are no longer applicable to the QCD matter inside. This can be understood by referring to the running of the QCD coupling constant (Figure 1.1) which implies that as the energy scales of QCD degrees of freedom increase (or as the corresponding distance scales decrease), the effective strength of any QCD interaction decreases asymptotically. At sufficiently high energies, the behavior of individual quarks and gluons approach that of free particles and confinement is effectively ignored at small distance scales. This phenomenon is referred to as 'asymptotic freedom' and is exclusive to QCD. When collisions occur between hadrons such that large numbers of the participating partons interact at the energy scales just described, the confining potential maintaining hadron stability is weakened (in the region of the collision) and collective behavior between individual quark and gluon degrees of freedom emerges. The phase of matter generated in these collisions is referred to as a *Quark-Gluon Plasma* (QGP).

Much like how electrons and nuclei are freed from their atomic bound states in electromagnetic plasmas, quarks and gluons are effectively freed from their corresponding hadronic bound states in a QGP. In both scenarios, a characteristic temperature associated with a phase transition at a particular chemical potential must be reached for the deconfinement to occur. The discovery of this temperature for QGPs is the product of research coming out of the mid 1960s to the 1980s, in which the Statistical Bootstrap Model (SBM)(42; 43) was used to approximate the limiting temperature of a finite hadronic system. This temperature is the highest that can be experienced by normal hadronic matter (hadron gasses) and is referred to as the *Hagedorn Temperature* (T_H). The Hagedorn Temperature is where the deconfinement transition occurs at low chemical potential and is currently estimated to be between approximately 130 MeV and 170 MeV ($O(10^{12}\,K)$). In order for QGPs to be studied experimentally, only the most violent among the heavy-ion collisions should be investigated. Historically the way to do this is to select for collisions with low impact parameter (b). Impact parameter, in this context, is defined as the transverse spatial separation between colliding nuclei and thus selecting for heavy-ion collisions where b is small is equivalent to maximizing the overlap of incident nuclei in the transverse plane. It should be noted that the term 'impact parameter' is also used in a variety of ways between various experiments and collaborations, as will be evident in the discussion of an LHCb-specific term in chapter 4. For the purposes of this chapter, 'impact parameter' will continue to refer to b as defined previously and in Figure 1.6.

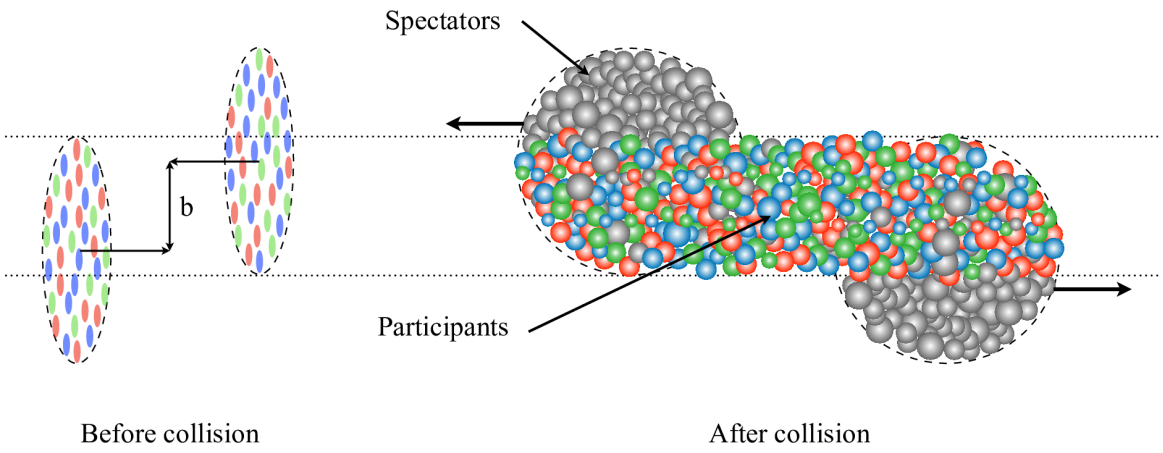


Figure 1.6: Schematic of a heavy-ion collision in which the impact parameter (b), participating, and spectating nucleons are depicted (4).

As the impact parameter in heavy-ion collisions decreases, the average amount of nucleons that participate in an interaction (commonly represented by $\langle N_{part} \rangle$) increases until there are effectively no spectating nucleons. With each scattering, a number of charged particles are produced and potentially recorded by a detector. This produces a monotonically positive relation between N_{part} and the multiplicity of final state particles observed. Given that impact parameter and N_{part} are not directly accessible or tuneable, the method for experimentally investigating QGP production (or any other phenomena dependent on collision event activity) is to sort events by detectable, final state particle multiplicity observables. In most analyses of this nature, the multiplicity (i.e. event activity) observable is either a count of the charged particle trajectories observed and reconstructed in a detector volume (N_{ch}) or the total energy deposited in a calorimeter. Once a large enough dataset of collisions is acquired, the multiplicity distribution can be used to sort events into classes of event activity. For heavy-ion collisions this is often accomplished by fitting a negative binomial distribution to the multiplicity observable and creating percentiles of event activity based on the fit result. This choice of lineshape is motivated by the Glauber model(44; 5), which represents colliding nuclei as spheres comprised of spherical nucleons with scattering probabilities directly dependent on impact parameter b.

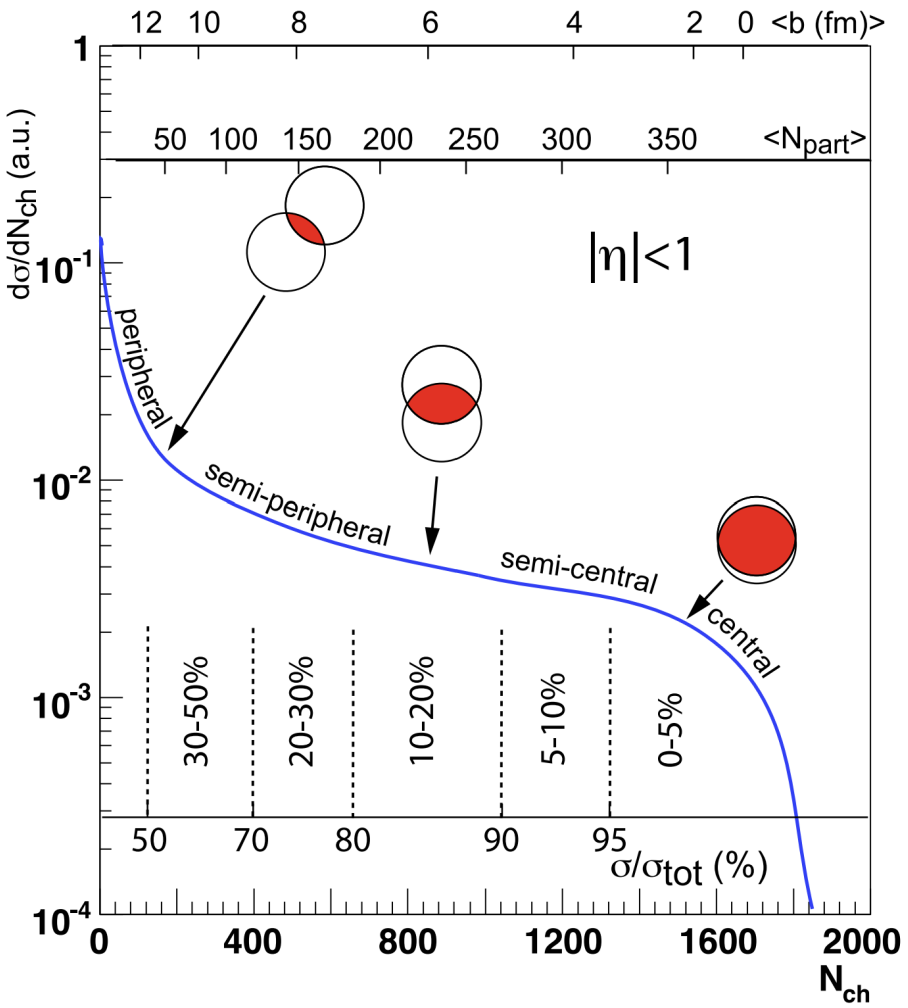


Figure 1.7: Illustration of a typical charged particle multiplicity distribution according to the Glauber model(5). The scales for average impact parameter (b(fm)) and average number of participating nucleons (N_{part}) are also shown.

After grouping collisions by measured event activity in this way, searches for QGP-related phenomena can be performed in each percentile bin, which is commonly described as a centrality class (see Figure 1.7). A measurement is generally considered to have strong evidence for QGP production when a clear dependence on event activity is established in a medium-sensitive observable. Many of these observables are types of nuclear modification factors (depicted as R_{AA} for ion-ion collisions), in which a yield of a particular signal (usually a hadron or jet) is compared between heavy-ion collisions and proton collisions in the form of a ratio.

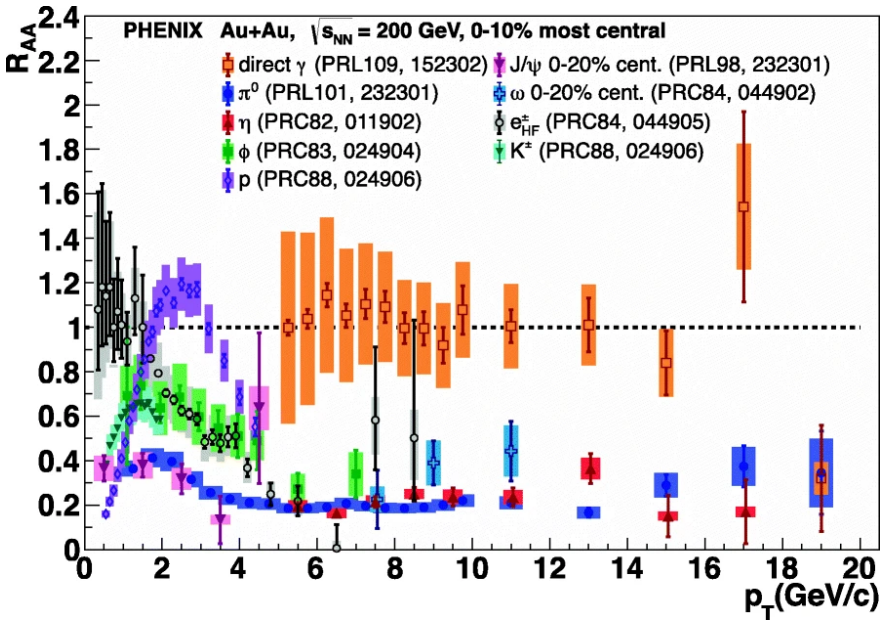


Figure 1.8: Collection of nuclear modification factor measurements of various particle species by the PHENIX experiment(6; 7). The direct photon results (Orange) are shown as a control since the direct photon production mechanism is independent of collision activity and QGP production.

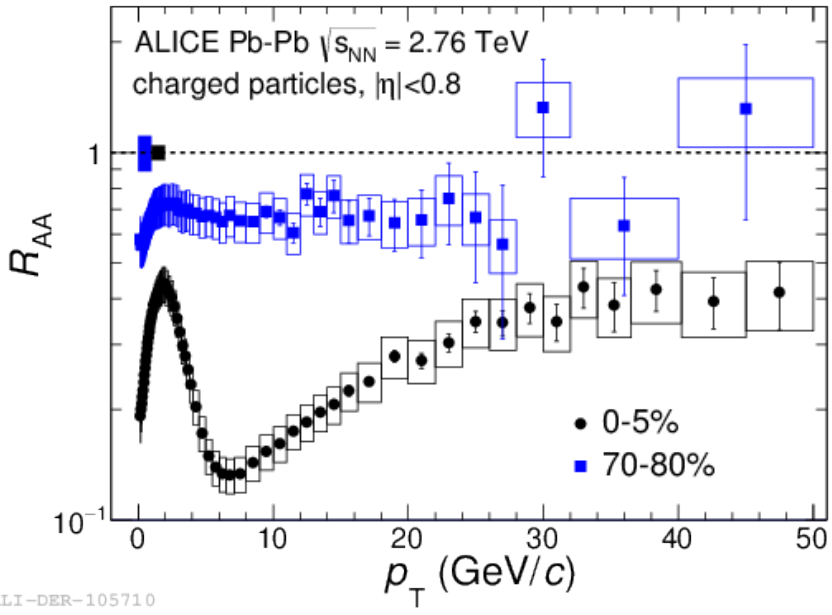


Figure 1.9: Charged hadron nuclear modification factors measured by the ALICE experiment at high (Black) and low (Blue) event activity(8; 9).

The collection of evidence using these observables has constructed a strong case for the production of QGP in heavy-ion collisions, however there are initial state and cold nuclear effects that could contribute to the results that have been recorded thus far. For this reason, it has been very fruitful to also investigate using observables that are directly sensitive to the chemistry and kinematics expected in an evolving QCD medium. It had been postulated and then experimentally verified that the chemical evolution and high parton densities present in a QGP allow for the existence of mechanisms in which the hadronization of new species is modified beyond the original Lund string fragmentation picture. Two observables in which these modifications were apparent are the centrality-dependent production rates of baryons and strange hadrons respectively. By utilizing these observables, not only can QGP production be probed to higher precision, but new collision-system dependent hadronization mechanisms can be characterized.

1.4 Modified Hadronization and Small Systems

The Lund string fragmentation model as discussed so far does not account for any changes in production rates for particular species (e.g. baryons and strange hadrons) stemming from higher collision densities or event activities. Microscopic models for how hadronization can be modified in dense collision systems to produce baryon or strangeness abundances date back to the 1970s(45), yet still remain an active area of research in theory and phenomenology.

1.4.1 Statistical Hadronization Model

Following the work done to establish the concept of the Hagedorn temperature, it became natural to represent the volumes of high-temperature (and density) regions in the collision to be QCD matter at some unspecified chemical potential. Given a large enough volume, the interior of a QGP should approach some thermal and chemical equilibria after some characteristic times. The evolution of the equilibrium and pre-equilibrium phases of a QGP can be modeled with canonical and microcanoncial ensembles respectively, hence the *Statistical Hadronization Model* (SHM)(46; 47; 48; 49). Thermal equilibrium (or thermalization as it is often described) can be achieved via the high frequency of partonic scatterings and the production of thermal quarks in the medium. Given that the initial heavy-ion collision consists of several nucleons of non-zero baryon density (exactly 1 per nucleon), the initial chemical potential of the system is non-zero. The production of quark flavors not present in the initial state is independent of the baryo-chemical potential, whereas the thermal production of *up* and *down* quarks is suppressed with respect to the potential. The *strange* on-shell

quark mass is approximately 93.5 MeV/c^2, which is lower than the estimated minimum of the Hagedorn temperature ($T_H \gtrsim 130$ MeV). This means that the average kinetic energy in the medium is sufficient to produce strange quark-antiquark pairs via gluon fusion.

It should be noted that initially only quark annihilation processes were considered and as a result the chemical equilibration time was significantly longer than the expected QGP lifetime for accessible heavy-ion collisions, thus any QGP produced would always exist in a pre-chemical equilibrium phase(50; 51; 52; 53). Eventually, Rafelski and Muller introduced the gluon terms and saw that the strange quark pair creation rates increased at least an order of magnitude, greatly reducing the chemical equilibration time, meaning that strangeness production in medium is also a probe for thermal gluon densities(10). This is not the case for heavier species produced in-medium (i.e. *charm*) since the on-shell mass threshold is approximately an order of magnitude higher (at least) than T_H, thus making the pair-annihilation process the primary production mechanism which leads to non-zero but significantly shallower effects in comparison to strange quark production.

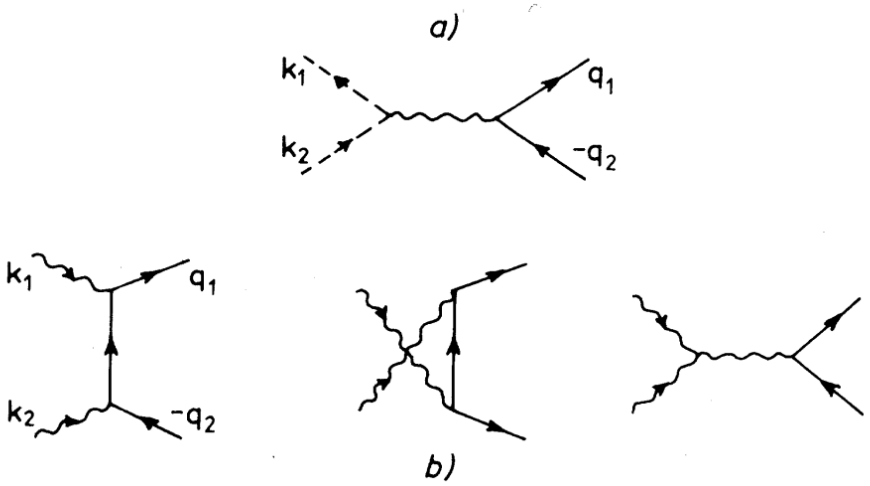


Figure 1.10: Contributing Feynman diagrams for thermal quark production: a) pair production via s-channel quark annihilation b) gluon fusion pair production via t- (left), u- (center), and s- (right) channel(10)

This leads to a relative thermal production rate that favors (anti-)strange quark production with respect to chemical potential. The primary constraints for strange quark yield are the peak temperature of the system as well as the medium lifetime since the production mechanism described will contribute to strange quark abundance as long as energetic gluons above the strange quark mass threshold exist in an asymptotically free region.

As the medium evolves and the volume of material above the deconfinement temperature decreases, hadronic states are formed out of clusters of neighboring partons in phase space.

The increased relative abundance of strange quarks in the plasma translates to a relative enhancement of strange hadrons in the immediate final state. This is due to the clustering of quarks with their phase-space neighbors to form new hadrons as the temperature of the now strange quark-doped medium lowers below that of the deconfinement regime. It is important to note that while the amount of strange quarks and antiquarks produced is enhanced in the Statistical Hadronization Model, the strangeness quantum number (S) of the collision system remains unchanged. This can be seen by recalling that any pair production mechanism will yield a strange quark ($S = -1$) and antiquark ($S = +1$). Despite this symmetry, the nearest phase-space neighbor to any thermally produced strange quark may not be its corresponding antiquark (or vice versa) at the time of clustering since in-medium scatterings and potential hydrodynamics may separate them spatially and/or kinematically. For this reason, it is expected that (anti-)strange hadron production should increase relative to non-strange yields as a function of medium lifetime and temperature, which is experimentally mappable onto event activity.

On the kinematic side, the p_{T} spectra for hadrons produced by a thermalized (or near thermal equilibrium) QGP is expected to fall sharply(54; 55; 56). There is broad agreement between the SHM, the SBM, and experimental results in this regard which allows for the peak medium temperature to be measured from the yield slope with respect to p_{T} (57; 58). This is indicative of there being a relatively high concentration of soft (low-momentum) partons in the later stages of the QGP due to either energy loss to multiple scatterings or low p_{T} thermally produced pairs. Another prediction of the SHM is that baryon production at intermediate transverse momenta for GeV- TeV scale collisions ($1\ \mathrm{GeV}/c \leq p_{\mathrm{T}} \leq 5\ \mathrm{GeV}/c$) should see a relative enhancement due to the accumulation of low-p_{T} partons. The reasoning dictates that for a particular hadronic p_{T} ($p_{T,h}$) in the final state, the average transverse momentum of the progenitor (anti)quarks at the time of clustering is $\sim \frac{1}{2}p_{T,h}$ for mesons and $\sim \frac{1}{3}p_{T,h}$ for baryons. The density of low momentum quarks in the equilibrated QGP increases the production probability for baryons with respect to mesons in the final state. Several experimental results in heavy-ion collisions have confirmed enhancements of baryon-to-meson ratios in the p_{T} range stated previously for a variety of species as well as the effect's dependence on centrality(59; 20).

While the SHM and post-QGP clustering (or more commonly *coalescence*) mechanisms generally agree with experimental results, there are often discrepancies that arise for higher p_{T} hadrons. This suggests that additional modifications to hadronization may be occurring in the harder part of the p_{T} spectrum.

1.4.2 Lund String Fragmentation

The original Lund String Fragmentation model discussed earlier was developed to describe the dynamics of hadron production in parton-sparse environments. Given the strong performance record of the model in replicating hadronization rates for e^+e^- and small hadronic collision systems (e.g. pp), it is likely that the string fragmentation picture has a non-zero contribution to the hadronization process in high event activity collisions. Given that the SHM is not mutually exclusive with Lund String Fragmentation, the questions of precisely how fragmentation may be used to either modify or supplement hadronization mechanisms in high-density environments remains an area of active research. In particular:

- Is the Lund String Fragmentation model modified by any parton density-dependent processes or conditions?
- Do SHM and string fragmentation effects (modified or otherwise) work in concert in high-centrality heavy-ion collisions?

Various models to address these questions have been generated and shall be coarsely described here.

When applying the concept of Lund strings to very quark and antiquark dense environments, the interplay between overlapping strings can lead to new effects in quark production. Regarding high-density modifications to the fragmentation picture, the two most common processes considered are *Color Rope* hadronization(60; 61; 62) and *Color Recombination*(63). When two Lund strings overlap in space, their interaction can be represented by the Lie algebra of the SU(3) group. Similar to quarks and antiquarks, individual strings can carry one of three color charges at a time and are thus representable as color triplets or anti-triplets. When modeling these interactions the choice of triplet or anti-triplet representation relies on whether the flow of color charge is parallel or anti-parallel between the two strings. This leads to four scenarios for possible interactions between two Lund strings. Firstly, for parallel strings

$$3 \otimes 3 = \bar{3} + 6 \tag{1.7}$$

and then for anti-parallel strings.

$$3 \otimes \bar{3} = 1 + 8 \tag{1.8}$$

The anti-triplet result for parallel strings implies that two different color charges flowing in the same direction is equivalent to the remaining color charge flowing in the opposite

direction (e.g. $|rb\rangle = |\bar{g}\rangle$). This is consistent with the behavior of quarks as color charges since they can only hadronize with an antiquark of the same color to form a meson or a di-quark of the two adjacent colors to form a baryon.

The singlet scenario results in an attraction between the Lund strings of corresponding color and anti-color. Anti-triplet strings can now experience attractive interactions with triplet strings, which would lead to the formation of 3-string junctions or Color Recombination (also known as Color Reconnection). This process is how baryon enhancements are expected to be accounted for in purely string-based models since fragmentations around these junctions would simultaneously produce quarks of all three colors.

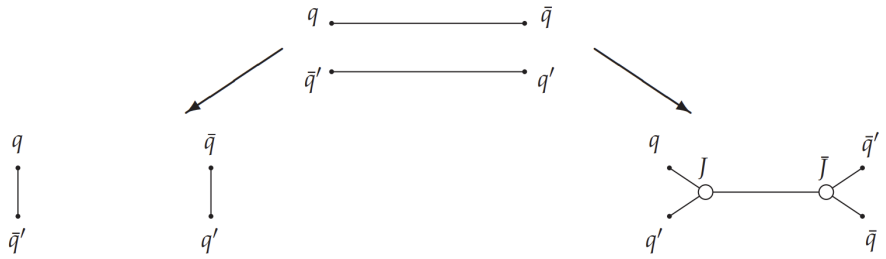


Figure 1.11: Diagram of color reconnection between anti-parallel strings into either (Left) a new color topology, or (Right) string junctions(11).

For the cases of the sextet and octet representations, the chromo-electric interactions are repulsive rather than attractive and create transverse *string shoving*. Additionally, the overlapping color fields in these higher multiplet scenarios result in an effective elastic constant which is larger than the original (anti-)triplet elastic constant (see section 1.2.1). For example, in the sextet case

$$\kappa_{\text{original}} \propto C_2^3 \tag{1.9}$$

$$\kappa_{\text{effective}} \propto C_2^6 - C_2^3 = \frac{3}{2}C_2^3 \tag{1.10}$$

where C_2^3 and C_2^6 are the relevant Casimir terms for the triplet and sextet representations respectively. The implication of this is that color strings can act collectively to form higher-tension Color Ropes. The average energy stored in these ropes is larger than for individual strings due to the enhanced κ and thus higher internal energy. Due to this, the probability of a fragmentation occurring at a string (or in this case rope) energy greater than the strange quark mass threshold is increased and an enhancement of previously mass-suppressed quarks is possible.

Critically, it must be discussed that Color Recombination, Color Ropes, individual Lund string fragmentations, and coalescence hadronization with the SHM are not necessarily mutually inclusive or exclusive. The Color Recombination and Color Rope models do not require the formation of a QGP (or similar QCD medium) in the way that the SHM does and are therefore possible alternatives to the SHM. Many phenomenological models, however, also take the approach of combining the SHM with Lund fragmentation (modified or unmodified). This is generally accomplished by assuming that not all of the participating partons in the collision will be included in a produced QGP. The partons in the high-density region of the collision are considered to be in the QGP proper (or *core*) and are subject to the SHM and coalescence, whereas the remaining partons at lower densities surrounding the QGP exist in the corona and hadronize via fragmentation. In some models, Lund string-specific modifications (i.e. Color Recombination and Color Ropes) are generally applied close to the core-corona interface. These frameworks are collectively known as *Core-Corona* models(64; 65) due to the distinct density regions considered or *Coalescence+Fragmentation* models(66; 67; 68) on account of the two hadronization mechanisms employed. Several of these models exhibit high-performance in replicating the hadron spectra and relative yields produced in heavy-ion collisions, however, additional scrutiny is required to distinguish what the balance of individual mechanisms should be.

This necessitates the experimental community to expand its scope of possible measurements.

1.4.3 Evidence in Small Systems

Given the use of pp collisions as baselines for many QGP results, it was widely accepted that the energy and parton densities accessible in proton collisions were too low to produce a QGP or modify the hadronization mechanisms present. The strong nuclear modification factors in central heavy-ion collisions(6; 7; 8; 9) along with the lack of jet-quenching(69; 70; 71) in proton collisions were considered evidence enough that activity-dependent modified hadronization effects should not be present in small collision systems.

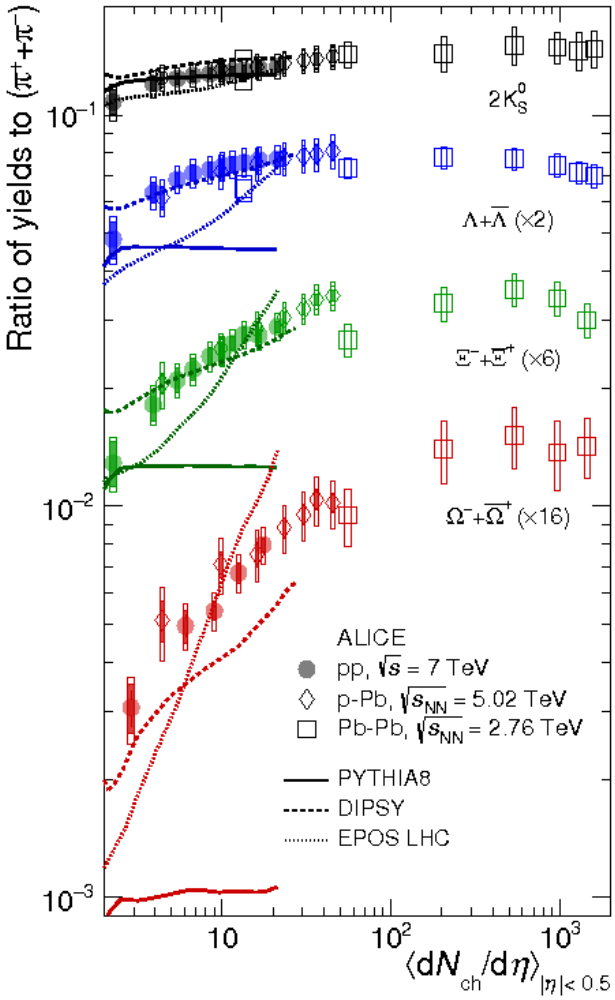


Figure 1.12: Gradual enhancement in production with respect to charged pions $(\pi^+ + \pi^-)$ in several hadrons of varying strangeness (12).

Experimental measurements of activity-dependent hadron production rates in pp events contradict this historical sentiment. In the results from the ALICE collaboration shown in Figure 1.12, the enhancement of strange hadrons with event activity is not only evident in pp and collisions but appears to smoothly approach and overlap with the results from heavy-ion collisions. The absence of large discontinuities between collision systems implies that the enhancements occurring in high-density proton collisions are likely due to the same hadronization modification mechanisms present in central heavy-ion collisions. These results necessitate a finer understanding of the aforementioned hadronization schemes and how they apply to small-systems, which in turn requires significantly more experimental observations.

1.5 Motivation and Objectives

The motivation for the work described in this dissertation is to provide experimental data for the purposes of understanding the onset of activity-dependent hadronization modifications in small systems.

Both historical observations in heavy-ion collisions and newer results in small systems are dominated (almost exclusively) by measurements taken at mid-rapidity with respect to the beam direction. This has allowed for a general consensus in this kinematic and geometric region on the qualitative existence of these hadronization effects. However, a drawback emerges from this. In the restricting of phenomenological models to the mid-rapidity region (usually $|y| \lesssim 1$) it has been challenging for theorists to model rapidity-dependencies for hadronization observables. This limits the collective understanding on the kinematics of these processes (this is particularly detrimental for models that utilize hydrodynamics in their QGP phase simulations). What is unique about the measurements taken in this thesis is that signal particles are all measured in the 'forward' rapidity region ($2 < \eta < 5$ or $1.5 \lesssim y \lesssim 5$). In addition, the impact of final-state event geometry on the hadronization rates is also investigated. These aspects will provide significant constraining power for the geometric and kinematic dependencies of hadronization modification, which in turn will constrain the kinds of models at play in small systems. This discriminating and constraining power is afforded by the unique acceptance and capabilities of the LHCb detector at CERN, to be discussed in chapter 2.

1.5.1 Strangeness Enhancement

One measurement of interest is the search for strangeness enhancement in pp collisions. As discussed earlier, the activity-dependent processes by which strange (anti)quarks are generated is via an in-medium chemical evolution or modification of the color field strength, either of which is categorically absent in the original fragmentation picture. The observation of event activity-dependent strangeness enhancement in proton collisions is an unambiguous signal of additional hadronization mechanisms existing in small collision systems.

The LHCb collaboration has contributed to the effort of measuring small-system strangeness enhancement in recent years. This includes recent measurements of enhancement in the $\frac{B_s^0}{B^0}$ ratio(13) and the $\frac{D_s^+}{D^+}$ ratio(14) shown in figures 1.13 and 1.14 respectively.

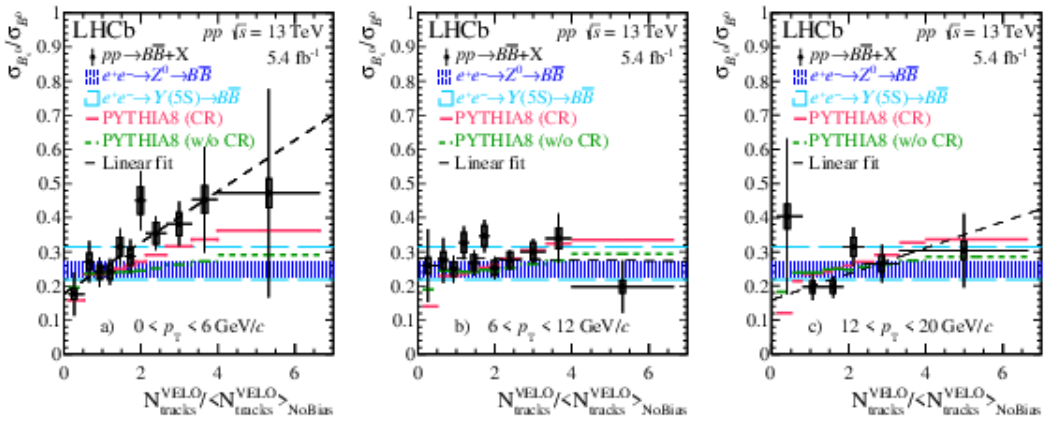


Figure 1.13: Observation of strangeness enhancement in B mesons from proton collisions in various transverse momentum bins(13). Comparisons are made to production ratios from non-hadronic collisions via the electroweak (dark blue) and bottom quark resonances (light blue). Monte Carlo predictions utilizing standard Lund String Fragmentation (green) and Color Recombination (red) are supplied.

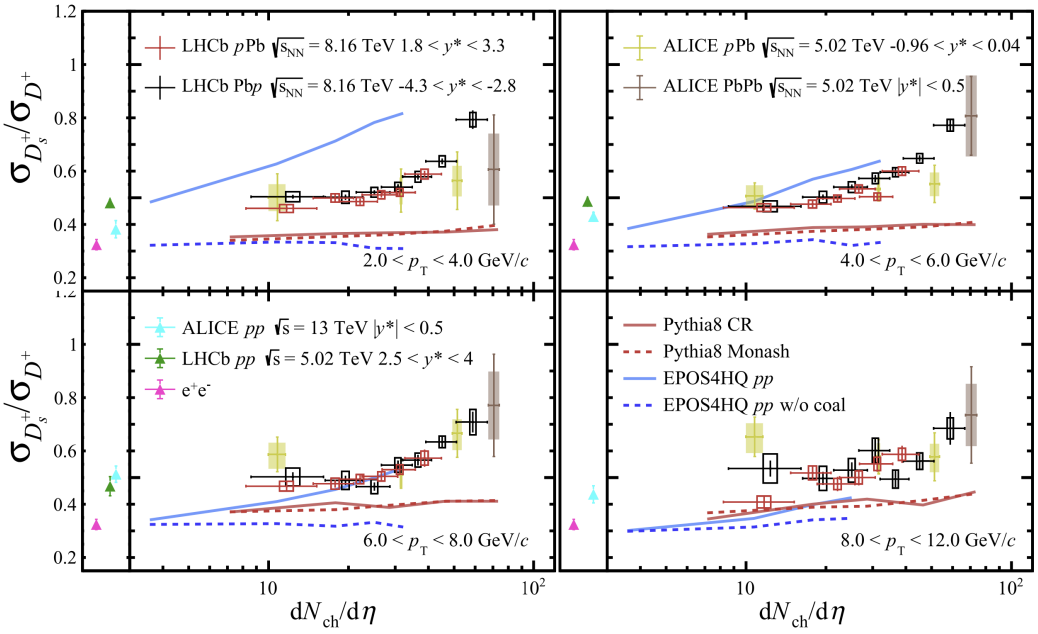


Figure 1.14: Observation of strangeness enhancement in D mesons from proton-lead collisions in various transverse momentum bins (black and red)(14). Comparisons are made to production ratios from ALICE (yellow and brown)(15; 16), integrated pp ratios from LHCb (green)(17), ALICE (cyan)(18) and e^+e^- (magenta)(19). Monte Carlo predictions utilizing standard Lund String Fragmentation (dashed red), Color Recombination (solid red), mutiparton interactions (solid blue), and coalescence (dashed blue) are supplied.

These results are in qualitative agreement in the case of the bottom mesons, and quantitative agreement in the case of charm mesons with previous mid-rapidity results. It should be noticed, however, that these results have been exclusively measured with heavy-flavor mesons. Like with strange quark generation, there are modifications that impact the rate of production for b and c quarks. Previous measurements at LHCb have established a lack of universality in the probability of b quarks generated in pp collisions to hadronize into mesons containing strange quarks (B_s^0) as opposed to down quarks (B^0)(72).

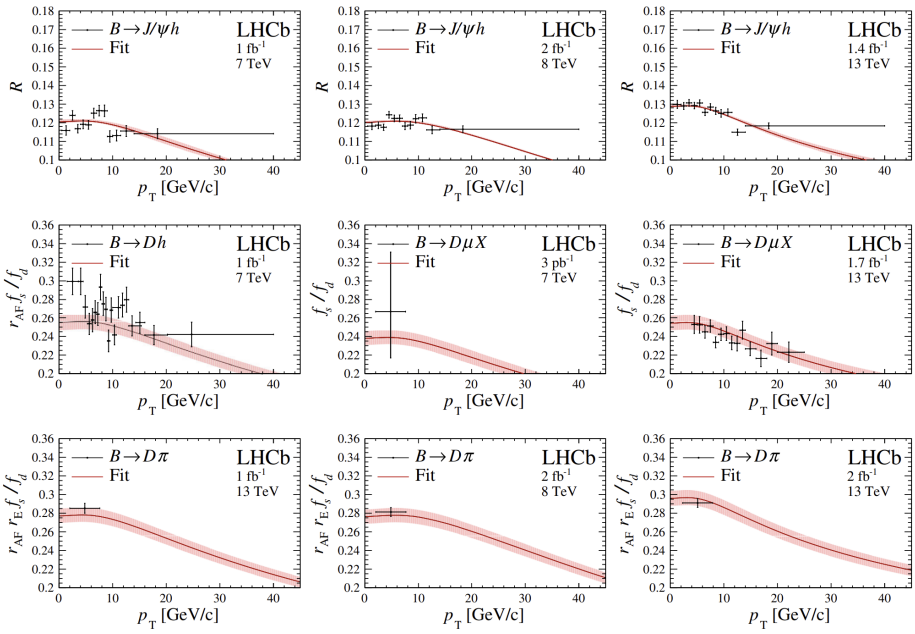


Figure 1.15: The measurement of various observables that are proportional to the relative probability of a b quark hadronizing into a strange vs non-strange meson in pp collision. The decay channel used to reconstruct the B meson, integrated luminosity of the dataset, and collision energy are provided for each measurement.

As discussed in sections 1.4.1 and 1.4.2, weak but non-zero pair production effects are possible for heavy quarks in either model. Additionally, initial and final state effects with potential contributions to heavy flavor hadronization could be acting in concert, against, or agnostically to the previously depicted mechanisms. Increasing the number of potentially contributing processes to the measurements reduces constraining power on the relative contribution of individual mechanisms, meaning that the accumulation of measurements utilizing strictly light-flavored hadrons is particularly useful at this time to discern the relevance of specific hadronization models. To address this demand, multiple light flavor species of varying strangeness are studied (similar to the results from ALICE (12)) in this analysis.

1.5.2 Baryon Enhancement

Similarly to strangeness enhancement, LHCb along with other experiments have performed measurements of baryon-to-meson ratios with heavy-flavor species at mid and forward rapidities, and with light flavor at exclusively mid-rapidity.

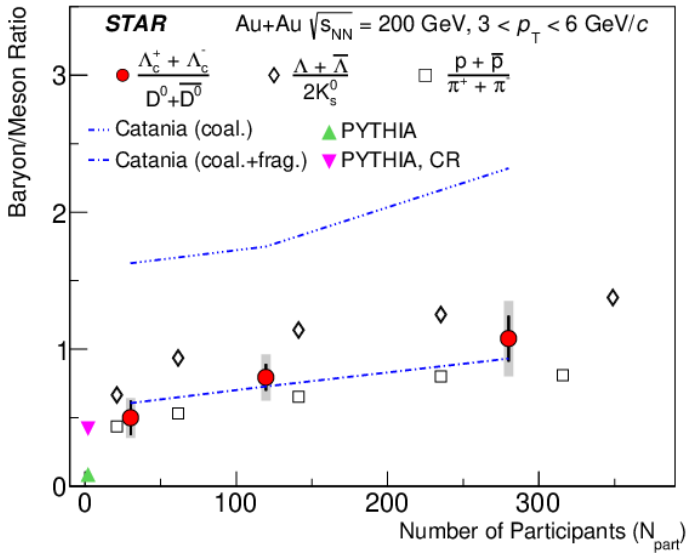


Figure 1.16: Baryon-to-meson ratios for charm (Circle), strange (Diamond), and light-flavored (Square) hadrons measured by the STAR experiment(20)

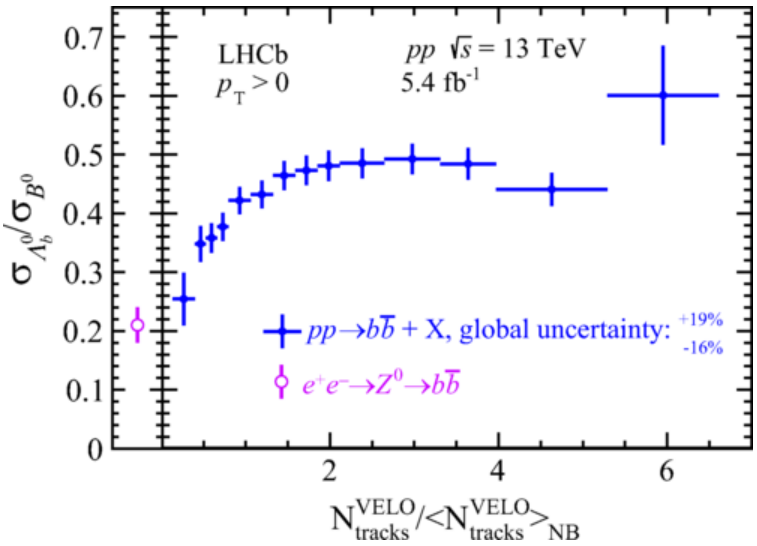


Figure 1.17: Baryon-to-meson ratio for bottom hadrons measured by the LHCb experiment (Blue)(21). The measurement from LEP (Pink) is provided as a reference(22).

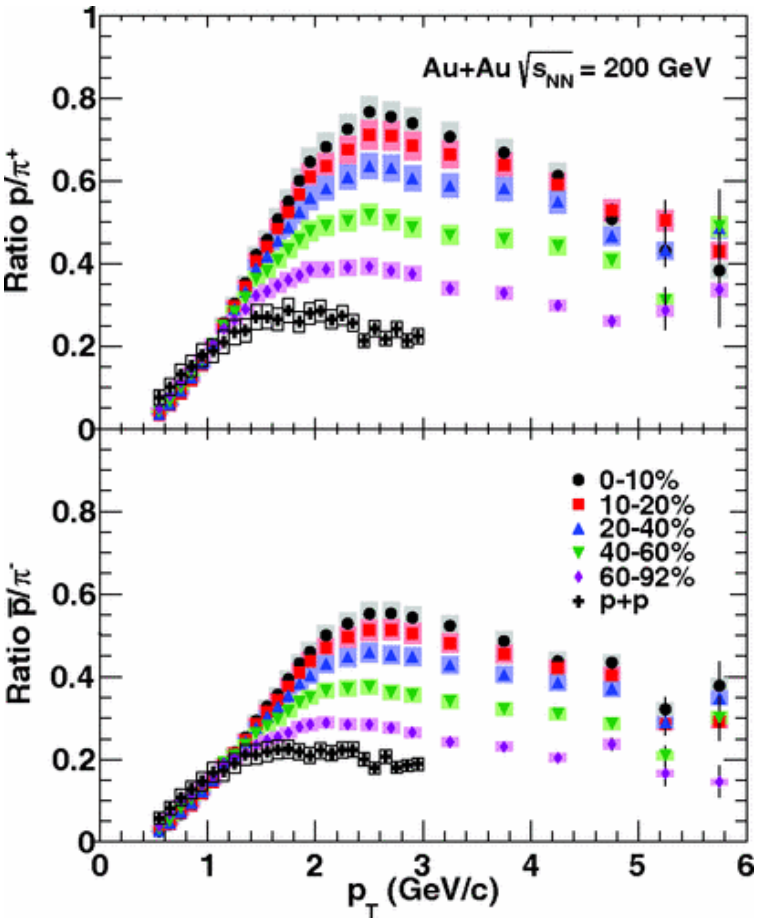


Figure 1.18: Baryon-to-meson ratio for protons and pions measured by the PHENIX experiment in various centrality Au+Au collisions and multiplicity-integrated pp collisions(23).

By carefully selecting the species of interest for this project, it is possible to simultaneously study strangeness and baryon enhancement with the same hadrons and datasets. This is achieved by measuring at least:

- A strange baryon: Λ (uds)
- A strange meson: K^0_S ($\bar{d}s$)
- A non-strange baryon: p (uud)
- A non-strange meson: π^+ ($u\bar{d}$)

In addition, a meson of hidden strangeness, ϕ ($s\bar{s}$), is measured to study the relationship between hadronization modification, strange quark content, and the strangeness quantum number ($S(\phi) = 0$). The added utility in this methodology (besides analysis efficiency) is that direct comparisons between strangeness and baryon ratios can be made, allowing

investigations into whether the effects are correlated (likely from the same hadronization mechanism) or independent (likely from separate mechanisms).
Aside from choice of hadronic species, the measurement of these ratios in pp collisions using the LHCb detector provides another axis of granularity. Due to the construction of the spectrometer, it is possible to probe not only how the geometric and rapidity distributions of the species of interest impact the results, but also how the geometry of the final state with respect to the species of interest correlates to the hadronization effects observed. This is due in particular to the tracking system of the LHCb detector (section 2.2.1) and will be described in chapter 4.

CHAPTER 2

Experimental Setup

2.1 The Large Hadron Collider

Following the conclusion of the eleven year run of the Large Electron-Position Collider (LEP) in the year 2000, the European Council for Nuclear Research (CERN) installed a 26.6 km (16.6 mi) circumference hadron collider into the pre-existing CERN accelerator complex.

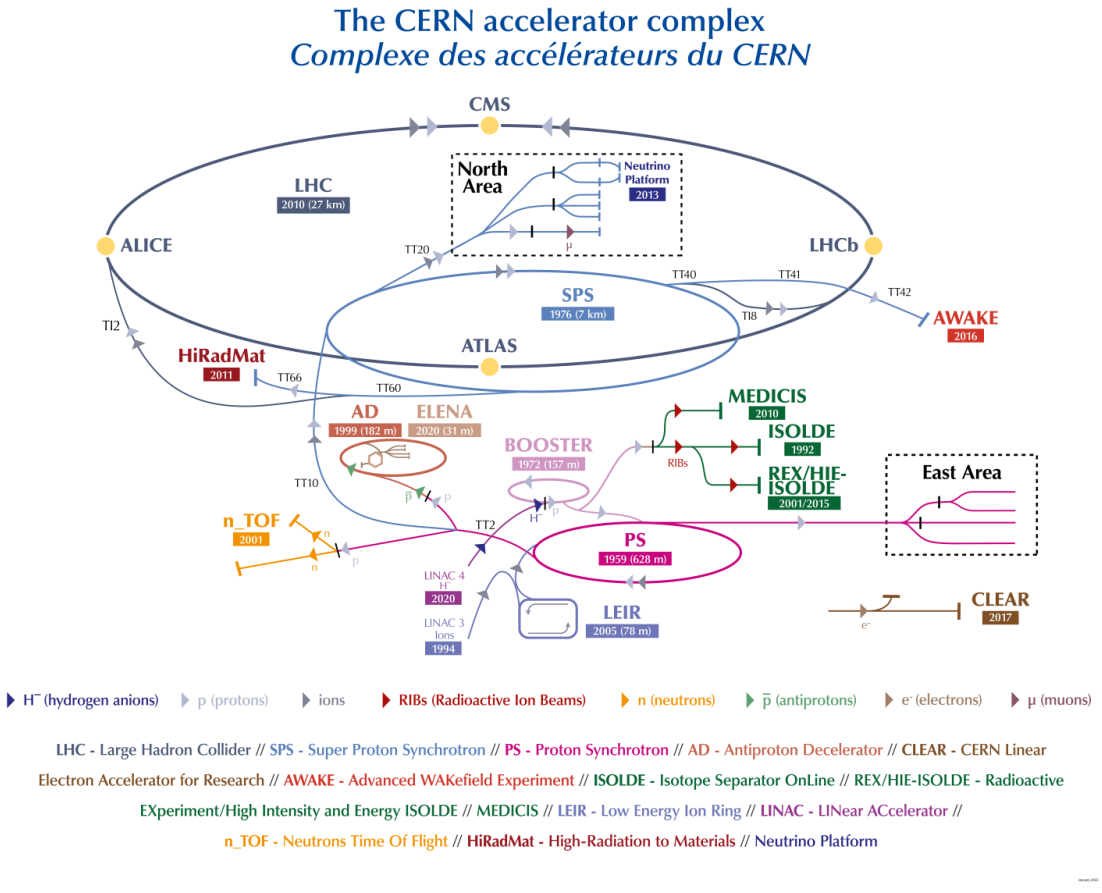


Figure 2.1: CERN Accelerator Complex as of 2022

The motivation for this was to create a multipurpose, high-luminosity, energy-frontier collider which would be sensitive to a myriad of outstanding physics questions, including the existence of the Higgs boson. By utilizing the older proton synchrotrons (the Proton Synchrotron (PS) and Super Proton Synchrotron (SPS) to accelerate proton beams up to 26 and 450 GeV respectively), the maximum operating beam energy possible at the Large Hadron Collider (LHC) is 7 TeV which corresponds to a maximum center of mass energy of $\sqrt{s} = 14$ TeV. For Run II of the LHC (2015-2018), the operating proton-proton (pp) collision energy was set to $\sqrt{s} = 13$ TeV, with both beams operating at 6.5 TeV.

2.2 The LHCb Experiment

The Large Hadron Collider Beauty Experiment (LHCb) (Figure 2.2) is a single-arm forward spectrometer with a fiducial pseudorapidity range of $2 < \eta < 5(24)$ (roughly $77^\circ \sim 15^\circ$). The LHCb detector is unique among the four detectors operating at LHC collision points due to this geometric coverage. The initial purpose of the experiment was to study *CP* violation in heavy quark systems (beauty and charm; top is excluded due to its short lifetime). The cross-section of heavy quark production experiences a local minimum at mid-rapidity, thus it was statistically advantageous to cover a large range biased towards one of the beam directions. Despite the initial intentions for the experiment, this configuration allows for a variety of robust QCD related measurements due to the unique phase-space covered by the spectrometer and excellent hadron identification.

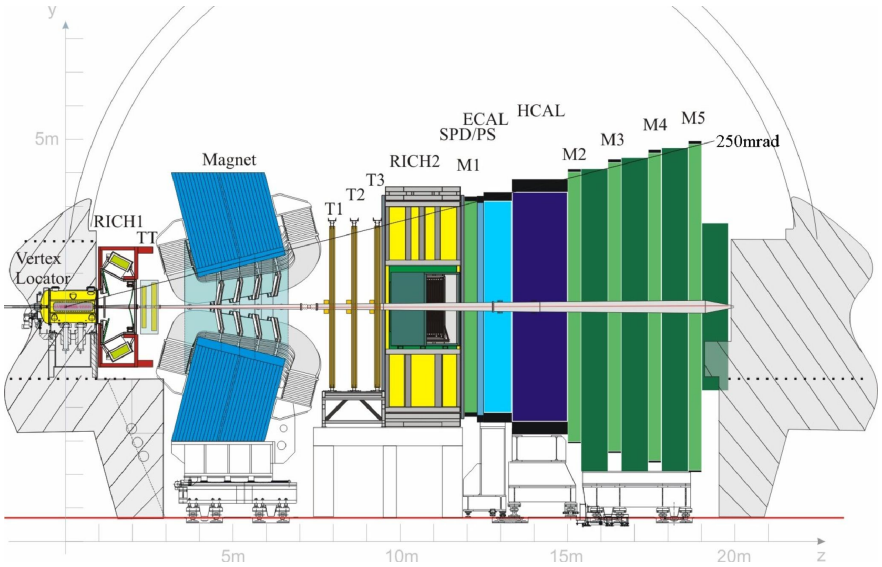


Figure 2.2: Diagram of the LHCb experiment and sub-detectors during Runs I and II of the LHC (24)

2.2.1 Tracking

The LHCb detector includes a high-precision tracking system consisting of several sub-detectors. Surrounding the nominal *pp* interaction region is the vertex locator (VELO), a large-area silicon-strip detector (TT) located upstream of a dipole magnet with a bending power of about 4 Tm, and four stations of silicon-strip detectors and straw drift tubes placed before and after the magnet (T-stations).

VELO tracks are reconstructed from hits in the VELO and are not subjected to kinematic constraints. The VELO is installed within the LHC beam-pipe and thus was built to resolve tracks at high granularity. To achieve this, layers of silicon-strip panels are oriented in alternating radial and azimuthal strip patterns (see Figure 2.3). Hits (or *clusters*) in three consecutive radial-strip sensors are grouped into *triplets* based on the level of agreement between the interpolated position and size of the middle cluster from the two outer clusters with the measured position and size of the middle cluster(73). These triplets are used as the seeds for complete VELO tracks, which are constructed by matching clusters of monotonically increasing size to the trajectory of the original triplet. Due to the VELO surrounding the *pp* interaction point, there is VELO track acceptance in both the forward ($1.6 < \eta < 4.9$) and backward ($-3.5 < \eta < -1.5$) regions.

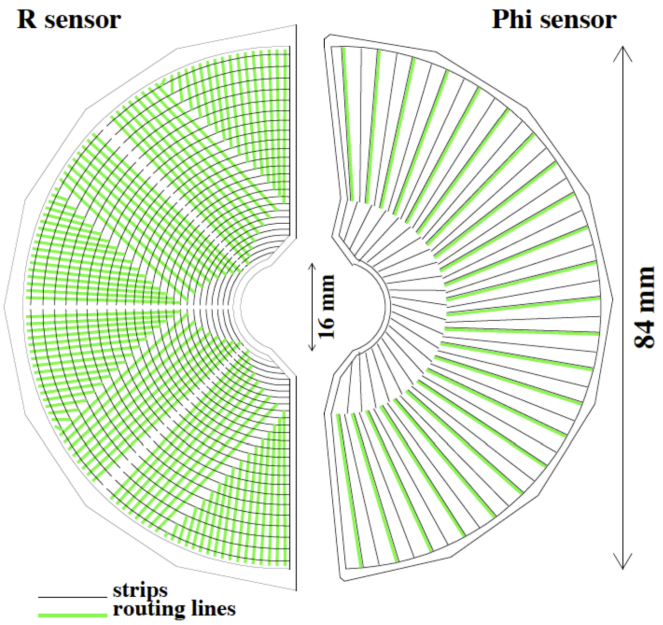


Figure 2.3: Diagram of the R and Φ-type VELO sensors along with their corresponding sensing lines (25)

Long tracks are reconstructed by matching observed hits in the downstream tracking detectors (T1-T3) with trajectories based on extrapolations of tracks from the upstream detectors, VELO and TT (replaced by the UT or Upstream Tracker after Run II), through the local magnetic field. This combination of track segments (or tracklets) before and after being deflected by the dipole magnet allows for kinematic information about the reconstructed tracks to be extracted from the trajectory.

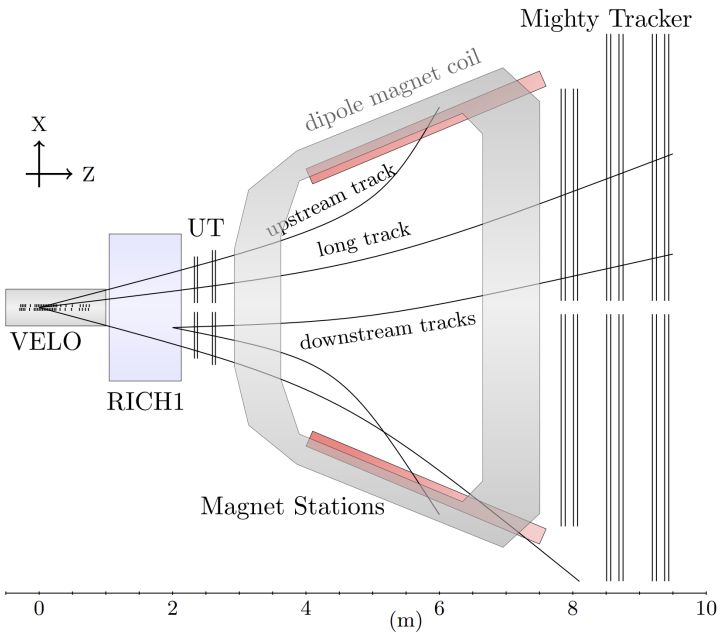


Figure 2.4: Diagram of various track types that can be reconstructed with the Run III LHCb detector along with the relevant tracking sub-detectors (26)

In order for a Long track to be detected by all relevant sub-detector components the charged particle trajectory must be within the fiducial η acceptance of the LHCb detector following deflection by the magnetic field. This creates additional constraints on the total particle momentum as well as the momentum component transverse to the LHC beamline ($p > 2$ GeV/c, $p_T > 200$ MeV/c).

2.2.2 Calorimetry

The energies of matched tracks and neutral particles are measured by the calorimetry system, which is composed of a Scintillating Pad Detector (SPD), a Preshower Detector (PS), an Electromagnetic Calorimeter (ECAL), and Hadronic Calorimeter (HCAL). Particle candidates with high transverse momentum in the calorimetry system are utilized for the low-level triggering system (L0).

2.2.3 Particle Identification

Different types of charged hadrons are distinguished by information from two ring-imaging Cherenkov detectors which combined, provide particle identification capabilities over the range of 2 GeV/c $< p_{track} <$ 100 GeV/c. The first Cherenkov station (RICH1) is located

between the VELO and the Tracker Turicensis (TT) to measure the Cherenkov angle and intensity prior to the magnetic deflection. RICH1 utilizes C_4F_{10} gas and an aerogel radiator to measure the Cherenkov angle at a resolution of 1.618 ± 0.002 mrad with maximal separating power at the lower end of the momentum acceptance. RICH2 implements CF_4 gas to separate the higher momentum tracks by measuring the Cherenkov angle at a resolution of 0.68 ± 0.02 mrad. The separation in Cherenkov angle trends for $\mu,\ \pi,\ K,$ and p tracks can be observed in the following RICH1 performance plot (see Figure 2.5).

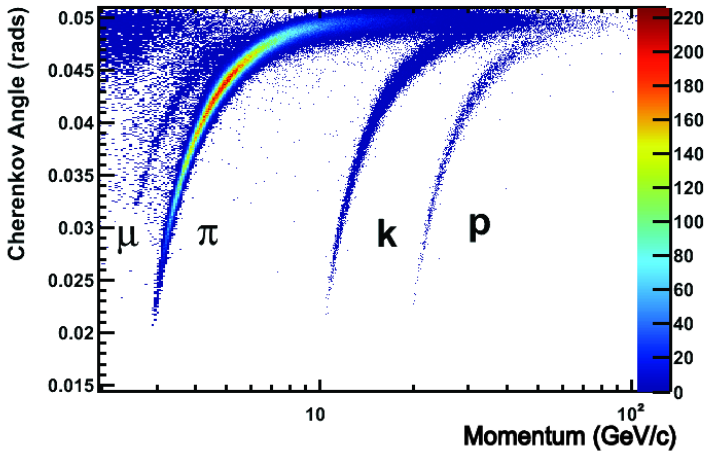


Figure 2.5: Cherenkov angle and track momentum correlation plots for muon and charged hadron tracks traversing the C_4F_{10} and aerogel radiators of RICH1. (27; 26)

This information is combined with measurements from the calorimeter to generate particle identification variables to the user. This is typically accomplished by utilizing the kinematic information obtained from the RICH and calorimetry systems to construct likelihoods for a particular charged track to match the mass hypotheses for the possible species ($e,\ \mu,\ \pi,\ K,\ p$). The relative probability for a candidate to be of species X ($e,\ \mu,\ K,\ p$) as opposed to a pion is represented by the difference in the logarithms of the mass hypothesis likelihoods for the given track ($\Delta\log\mathcal{L}(X-\pi)$ or DLL_X). Alternatively, a convolution neural network can be used instead of a likelihood function to produce a parameter that is correlated with low misidentification rates (ProbNNX). Since the previous method is not applicable to pion candidates, the ProbNNπ parameter is typically used for the selection of charged pion tracks.

2.2.4 Triggering

The Run II Triggering Framework consists of low-level (L0) and high-level (HLT) stages. The LHCb experiment utilizes tracking and calorimetry input to trigger an event selection, usually by reconstructing a particle candidate, which leads to a variety of datasets triggered by particular decays or scatterings. This structure is how the LHCb experiment has managed to record datasets of heavy-flavor hadrons large enough for studies into heavy-flavor decay channels and their connections to *CP*-violation.

When dealing with signal species with larger cross-sections, triggering on specific decay channels may not be necessary for accruing large statistics depending on the measurement. This method of data taking is used for an analyzer that is particularly concerned with introducing biases into their reconstructed signals, or that are interested in various signal species simultaneously. These minimum-bias (referred to as minibias or minbias internally) datasets are recorded by running the L0 trigger in *passthrough* mode, which accepts all incoming events that have passed a Global Event Cut (GEC) for event quality. For Run II pp collisions, this GEC is for the VELO detector to have at least three reconstructed tracklets for a particular event. Since there is no trigger decay in use during passthrough mode, the data taking is dependent on a trigger coming from the LHC beam clock which signals that a collision has occurred. For storage and bandwidth concerns, the passthrough data is scaled and then saved to disk.

2.2.5 Upgrades

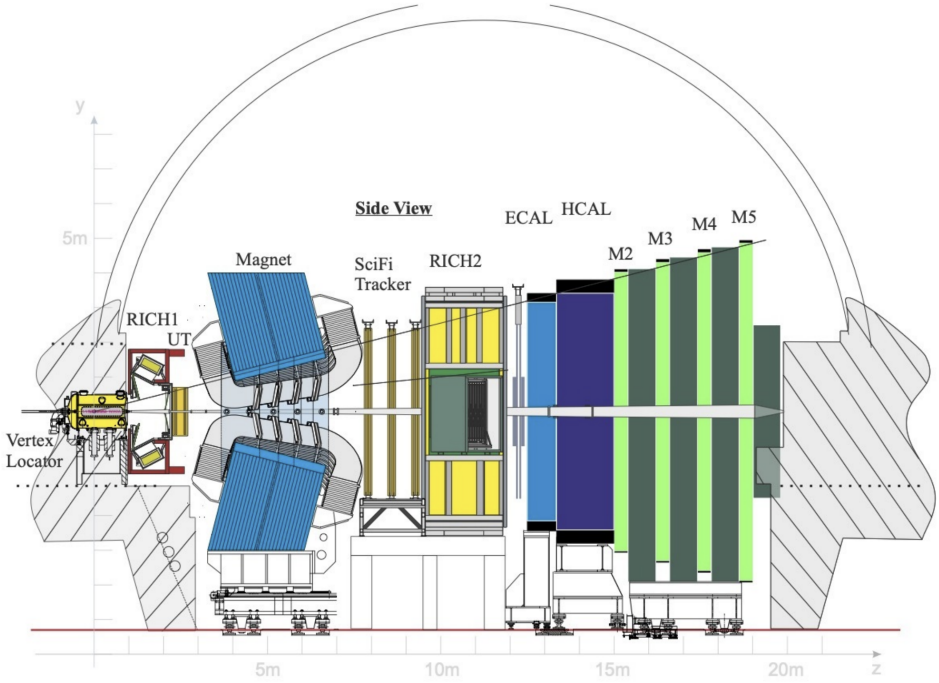


Figure 2.6: Diagram of the LHCb experiment and sub-detectors during Runs III of the LHC (28)

To improve the quality and precision of future measurements, upgrades were made to the LHCb detector to meet the demands of the Run III program. The LHCb experiment has amassed a significantly larger dataset over Run III as opposed to Run II, greatly in part due to the higher rate of data acquisition and improved radiation hardness of the instrumentation.

With larger volumes of high-quality datasets, future measurements of flavor and baryon production can be performed at higher precision. Additionally, species of interest with lower statistics can be added to the current list of measurements, especially mesonic resonances (e.g. K^{*0}), higher mass light-flavor baryons (e.g. Σ^0), and multi-strange or multi-heavy-flavor baryons (e.g. Ξ, Ω). Measurements of this kind rely heavily on the tracking system, which saw significant upgrades over Long Shutdown II (LS2) in preparation for Run III. Significant effort from the group at the University of Michigan has been supplied to the assembly and operation of the newly installed Upstream Tracker (UT) which has replaced the Tracker Turicensis (TT) as can be seen in Figure 2.6.

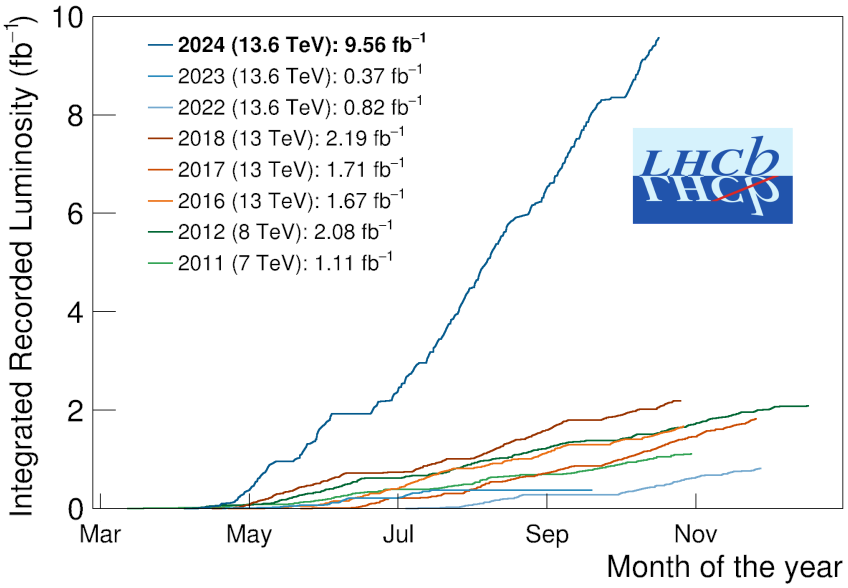


Figure 2.7: Integrated luminosity recorded from pp collisions by the LHCb detector over the course of each year of operation(29)

2.2.5.1 Upstream Tracker

The Upstream Tracker plays a vital role in the track reconstruction algorithm of the LHCb spectrometer since the hits found in the detector are used to match the VELO tracklets (from the Primary Vertex or PV) to the tracks downstream (final state charged particles). From a kinematic lens, this can also be appreciated as matching the in-flight trajectories of particles before and after deflection from passing through the magnet station.

The maximum readout rate for the front-end electronics of the Tracker Turicensis (TT) detector among other LHCb components was 1.1 MHz during Run II. This is a noticeably small percentage of the of the LHC collision frequency (40 MHz), meaning that a sizeable amount of collider data was inaccessible based on the timing resolution of the detector. For Run II and beyond, all relevant detector electronics (including the tracking front-end and peripherals) were replaced such that operation at the full 40 MHz collision rate was possible. Additionally, replacements for the the silicon-strip detectors (e.g. TT) were necessary due to displayed signs of deterioration from radiation fluence over the course of the first two LHC runs (see Figure 2.8).

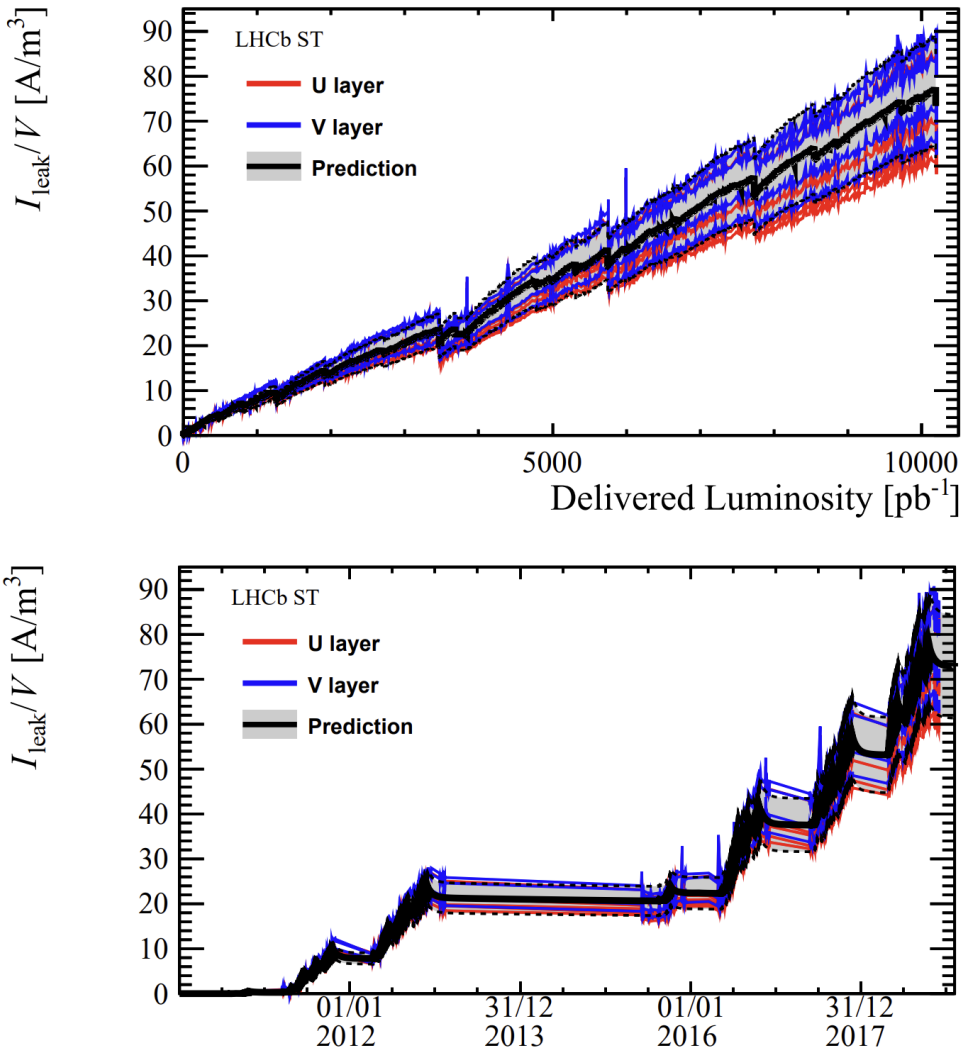


Figure 2.8: Measurement of leakage current across several silicon layers in the TT detector. Leakage current is measured (Top) with respect to integrated LHC beam luminosity delivered to the LHCb detector and (Bottom) throughout Run II(30)

The University of Michigan group has assisted in the characterization, assembly, installation, and operation of the Upstream Tracker. The core electronics for the current iteration of the Upstream Tracker consists of:

- 128-channel Silicon ASIC for LHCb Tracking (SALT) to readout the electric signal coming from the Silicon microstrip sensors. The front end contains an ADC operating at 40 MHz to match the LHC beam frequency(28).
- New Si-strip detector modules. Most of the modules are comprised of 512 strips with a pitch of 187.5 µm. The strip pitch is approximately halved (93.5 µm) for modules

closer to the beam-line (10 cm-34 mm), allowing for double the strip granularity (1024) for the inner region. The outer and inner modules are each outfitted with 4 and 8 SALTs respectively(28).

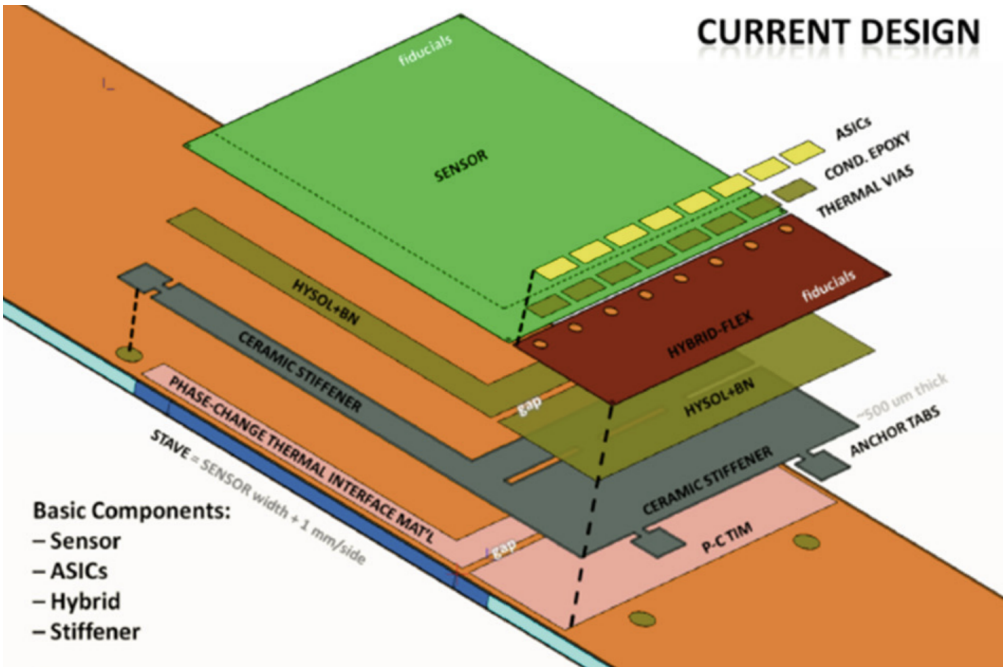


Figure 2.9: Exploded view of a module from the LHCb UT(31)

Peripheral electronics for data acquisition and detector operation were built and installed to meet the output frequency of the SALT chips. The impact of the newly integrated UT (along with the other new tracking components installed as a part of Upgrade I) can be seen in the significant jump in recorded luminosity observed in the LHCb detector over Run III thus far (see Figure 2.7).

CHAPTER 3

Description of Datasets

A suite of five hadronic species are used in these analyses of strangeness and baryon production. In order to meet the criteria laid out in section 1.5.2 the species of interest for this dissertation include the Λ (strange baryon), K^0_S (strange meson), p (non-strange baryon), and $\pi^{\pm}$ (non-strange meson). Additionally, the $\phi(1020\ \text{MeV})$ (or simply ϕ) meson is included due to it's hidden strangeness and comparable mass to the proton.

Compared to heavy-flavor species often recorded by LHCb (e.g. D^0, B^0) or larger mass hadrons with decay chains that are low-probability and/or difficult to reconstruct (e.g. Σ, Ξ), the hadrons chosen have significantly larger statistics and are easily reconstructed by the detector. This means that the implementation of high-level triggers is unnecessary to study the production rates of these species from Run II data. To ensure the accuracy of numerical comparisons between hadronic species yields without needing to correct for triggering efficiency or data prescale factors, this analysis is performed exclusively with minibias (see sec 2.2.4) data from recorded or simulated pp collisions. 2015 saw the largest accumulation of recorded collider and Monte-Carlo data from pp events (from Run II), therefore the collider and Monte-Carlo datasets used in this analysis were both from the 2015 data taking period. The yields of candidates for each hadronic species are extracted from the same minibias datasets by applying particle selection and reconstruction algorithms specific to each species. No distinctions are made between the listed criteria and their charge conjugate scenarios, meaning that the antiparticles to the signal hadrons are reconstructed as well. Unless otherwise stated, any discussion on the signal species will implicitly include the corresponding antiparticle.

3.1 Selection Criteria

In order to preserve the candidate quality, event quality, and confidence in the multiplicity distribution, some selection criteria are applied universally. Minimum momentum and transverse momentum cuts of 2 GeV/c and 0.2 GeV/c respectively are applied to all reconstructed charged signal or daughter tracks to match the acceptance criteria discussed in chapter 2.2.1. An additional global event quality cut (GEC) requiring at least one backward track in the VELO detector is implemented. Finally, all events are required to have exactly one reconstructed primary vertex (PV). The significance of the latter two criteria will be discussed in chapter 4.

3.1.0.1 π^+

Given the long lifetime of charged pions, candidates will traverse the entirety of the detector before decay and thus leave behind tracks in every stage of the tracking system (i.e. Long Tracks). A particle identification (PID) cut using the ProbNNπ (a neural network trained on RICH and Calorimetry information for pions specifically) is applied to distinguish pion candidates from other long-lifetime particles (e.g. protons).

3.1.0.2 p

Similarly to the charged pions, proton tracks traverse the entire detector volume. For PID in this case, a likelihood parameter is used to distinguish proton tracks ($\mathrm{DLL_p}$). Additionally, due to lack of true proton tracks with low-momentum, a higher kinematic cut is placed on all proton candidates.

Summary of Reconstruction and Selection Criteria		
	π^+	p
Track Type	Long	Long
p	$p > 2\,\mathrm{GeV}/c$	$p > 5\,\mathrm{GeV}/c$
p_T	$0.25\,\mathrm{GeV}/c < p_\mathrm{T} < 6.5\,\mathrm{GeV}/c$	$0.25\,\mathrm{GeV}/c < p_\mathrm{T} < 6.5\,\mathrm{GeV}/c$
η	$2 < \eta < 5$	$2 < \eta < 5$
y	$2.3 < y < 4.5$	$2.3 < y < 4.5$
PID	ProbNN$\pi > 0.9$	$\mathrm{DLL_p} > -5$
PV	nPV $= 1$	nPV $= 1$

Table 3.1: Selection criteria for non-decaying particle candidates.

3.1.0.3 Λ

For reconstructing neutral particles, a particular decay channel is chosen and the corresponding daughter tracks are used to construct a signal candidate. The $\Lambda \to \mathrm{p} + \pi^-$ decay has a branching ratio of approximately 64% and is chosen for this analysis. The cuts on the pion and proton daughter tracks are mostly identical to the selection criteria for the prompt pion and proton candidates above. To construct Λ candidates, the reconstruction algorithm combines daughter candidates into a neutral signal candidates. Additional cuts are applied to the signal candidates to enhance the reconstruction of genuine Λ decays.

- ADMASS: After combining the momentum vectors of the daughter tracks, a mass hypothesis can be calculated for the Λ candidate. To be considered as a potential signal candidate, a maximum discrepancy between the hypothesis and the value provided by the Particle Data Group(1) ($M_\Lambda = 1115.683\,\mathrm{MeV}/c^2 \pm 0.006\,\mathrm{MeV}/c^2$) is applied.

- Vertex-χ^2 (χ^2_{vtx}): The daughter track trajectories are extrapolated to a singular point of origin, the Decay Vertex (DV). Higher precision on daughter trajectories and on the projected overlap region reduces the χ^2_{vtx} quantity, corresponding to higher confidence in decay vertex reconstruction.

- IP-χ^2 (χ^2_{IP}): candidates have lifetimes on the order of 10^{-10} s, which is enough time (at the LHC energy scale) for the Vrimary vertex and Decay Vertex to be separated by some measurable distance ($O(\,\mathrm{cm})$). A minimum cut on the likelihood for each daughter track to have originated from the PV are applied such prompt particles are not misinterpreted as daughter tracks. This corresponds to a minimum χ^2_{IP} placed on each daughter candidate.

Summary of Reconstruction and Selection Criteria	
$\Lambda \to \mathrm{p} + \pi^-$	
Λ	
Mass	ADMASS $< 35\,\mathrm{MeV}/c^2$
p	$p > 2\,\mathrm{GeV}/c$
p_T	$0.25\,\mathrm{GeV}/c < p_\mathrm{T} < 6.5\,\mathrm{GeV}/c$
η	$2 < \eta < 5$
y	$2.3 < y < 4.5$
PV	nPV $= 1$
DV	$\chi^2_\mathrm{vtx} < 30$
Daughter p	
Track Type	Long
IP	$\chi^2_\mathrm{IP} > 9$
p	$p > 5\,\mathrm{GeV}/c$
p_T	$p_\mathrm{T} > 0.2\,\mathrm{GeV}/c$
η	$2 < \eta < 5$
PID	$\mathrm{DLL_p} > -5$
Daughter π^-	
Track Type	Long
IP	$\chi^2_\mathrm{IP} > 9$
p	$p > 2\,\mathrm{GeV}/c$
p_T	$p_\mathrm{T} > 0.2\,\mathrm{GeV}/c$
η	$2 < \eta < 5$
PID	ProbNN$\pi > 0.9$

3.1.0.4 K^0_S

The reconstruction of the K^0_S candidate is mostly identical to the Λ reconstruction algorithm and cuts. The $\mathrm{K}^0_\mathrm{S} \to \pi^+ + \pi^-$ decay has a branching ratio of approximately 69% and is chosen for this analysis.

3.1.0.5 ϕ

The $\phi \to \mathrm{K}^+ + \mathrm{K}^-$ decay has a branching ratio of approximately 49% and is chosen for this analysis.

Summary of Reconstruction and Selection Criteria		
	$K^0_S \to \pi^+ + \pi^-$	$\phi \to K^+ + K^-$
	K^0_S	ϕ
Mass	ADMASS $< 35\,\mathrm{MeV}/c^2$	ADMASS $< 35\,\mathrm{MeV}/c^2$
p	$p > 2\,\mathrm{GeV}/c$	$p > 2\,\mathrm{GeV}/c$
p_T	$0.25\,\mathrm{GeV}/c < p_\mathrm{T} < 6.5\,\mathrm{GeV}/c$	$0.25\,\mathrm{GeV}/c < p_\mathrm{T} < 6.5\,\mathrm{GeV}/c$
η	$2 < \eta < 5$	$2 < \eta < 5$
y	$2.3 < y < 4.5$	$2.3 < y < 4.5$
PV	nPV $= 1$	nPV $= 1$
DV	$\chi^2_\mathrm{vtx} < 25$	$\chi^2_\mathrm{vtx} < 25$
	$\pi^\pm$	$K^\pm$
Track Type	Long	Long
IP	$\chi^2_\mathrm{IP} > 9$	$\chi^2_\mathrm{IP} > 9$
p	$p > 2\,\mathrm{GeV}/c$	$p > 2\,\mathrm{GeV}/c$
p_T	$p_\mathrm{T} > 0.2\,\mathrm{GeV}/c$	$p_\mathrm{T} > 0.2\,\mathrm{GeV}/c$
η	$2 < \eta < 5$	$2 < \eta < 5$
PID	ProbNN$\pi > 0.9$	DLL$_\mathrm{K} > 7$

3.2 Monte-Carlo

Minimum Bias Monte-Carlo data sets are used in this analysis in order to study potential biases introduced in the reconstruction and selection process, as well as to account for true signal particles that did not pass the selection criteria. Two types of Monte-Carlo data are utilized to this end:

- Generated: Utilizing known hadronic cross-sections, parton distribution functions, and fragmentation functions, simulated pp collisions are tuned to match the energies and multiplicities observed at the LHCb detector. Particle candidates in these data sets are used as representations of the underlying physics of a collision event, thus these data sets are referred to as 'MCGen' or 'MCTruth'.

- Reconstructed: The reconstruction and selection algorithms utilized in collider data are simulated based on interactions between the generated Monte-Carlo particles (MCGen) and a rendition of the LHCb detector produced by GEANT4. The cuts applied to these candidates must match the criteria previously applied to the collider data candidates to ensure an accurate reproduction of the experimental data. For the purposes of this

analysis, particle identification cuts are not applied since the particle identification efficiency will be characterized by a dedicated software package.

Over the course of a data taking run, the polarity of the superconducting magnet is flipped such that at least two data sets of comparable size and opposite magnetic fields are recorded. The purpose of this is to mitigate potential biases that may arise from effect of the magnetic field direction on the particle acceptances, tracking, and particle identification. In order to properly characterize the detector, the same steps are taken for Monte-Carlo simulations. Each particle candidate is reconstructed and selected from a data set of a particular magnet polarity. The yields are calculated per polarity data set following the procedures outlined in chapter 4 and then combined to provide the final results. The summary of overall candidate statistics is provided in table 3.1.

Summary of Data Set Statistics						
	Collider		MC Reconstructed		MC Generated	
	Mag Up	Mag Down	Mag Up	Mag Down	Mag Up	Mag Down
π^+	$1.167 * 10^8$	$1.653 * 10^8$	$2.610 * 10^6$	$2.677 * 10^6$	$3.956 * 10^6$	$4.046 * 10^6$
p	$5.907 * 10^7$	$7.988 * 10^7$	$2.958 * 10^5$	$3.039 * 10^5$	$4.243 * 10^5$	$4.352 * 10^5$
ϕ	$1.923 * 10^6$	$2.833 * 10^6$	$4.990 * 10^3$	$4.972 * 10^3$	$7.112 * 10^3$	$7.176 * 10^3$
K^0_S	$5.014 * 10^5$	$7.258 * 10^5$	$1.180 * 10^4$	$1.220 * 10^4$	$4.637 * 10^4$	$4.748 * 10^4$
Λ	$1.478 * 10^5$	$2.153 * 10^5$	$1.478 * 10^4$	$1.487 * 10^4$	$3.153 * 10^3$	$3.119 * 10^3$

Table 3.2: Summary of Minimum Bias candidates passing the initial reconstruction and selection criteria.

CHAPTER 4

Analysis Details

4.1 Event Activity Estimation

In order to properly study hadronization modification in pp collisions, a suitable proxy for event activity must be determined. Rather than applying a Glauber fit to the energy distribution in the calorimetry system, which is common among similar studies in heavy-ion collisions, the multiplicity of tracks in the VELO subdetector are used. This is done for primarily two reasons: the Glauber model was developed for use in heavy-ion collisions where the focus was on multiple interactions for central collisions and nucleons were effectively considered degrees of freedom; the tracks detected in the VELO detector are the same tracks used to determine the number and location of primary vertices (PVs), meaning that these are inherently correlated to prompt particle production.

4.1.1 Choice of Multiplicity Estimator

An added feature of using VELO tracks is that, due to the detector's tracking acceptance in backwards pseudorapidity, event activity can be probed in a distinct geometric region from the signal particles. In order to investigate how this impacts multiplicity dependencies, two sets of event activity classes are used in this analysis. Five multiplicity classes are determined by dividing the distribution of Minimum Bias events into percentiles for multiplicities of inclusive VELO tracks (N_{VELO}) and backward rapidity VELO tracks (N_{BACK}). Only events with exactly one primary vertex per bunch crossing are considered for this analysis to ensure that multiplicity corresponds only to event activity. Additionally, a quality cut requiring that $N_{\mathrm{BACK}} > 0$ is applied. The standard minibias GEC already necessitates that $N_{\mathrm{VELO}} > 0$, so this secondary requirement makes the two multiplicity distributions more comparable and avoids any contaminations in the analysis that may arise from poor Monte-Carlo modeling of $N_{\mathrm{BACK}} = 0$ events.

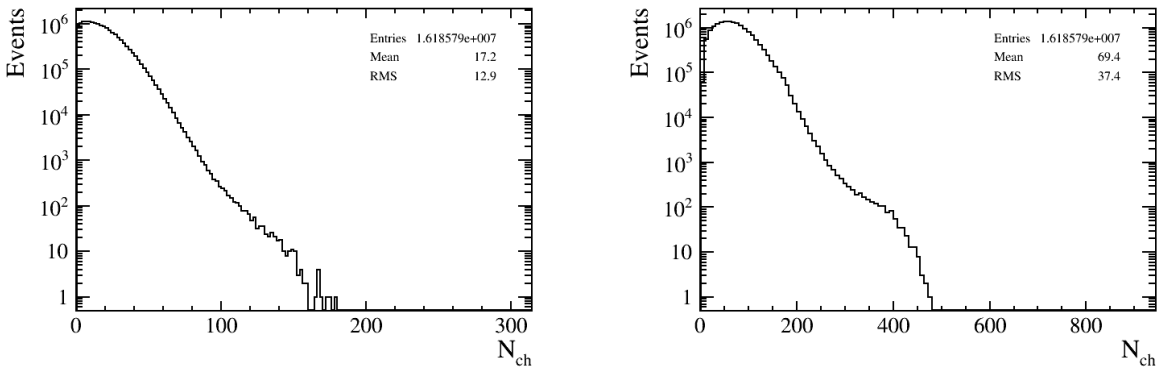


Figure 4.1: Multiplicity distributions of 2015 minibias events that meet the required primary vertex restriction. (Left) Backwards track distribution, (Right) VELO track distribution.

Based on the 2015 minibias event distributions, the multiplicity classes are defined as follows:

Multiplicity Class	Percentile Range	N_{BACK}	$\langle N_{\mathrm{BACK}} \rangle$	N_{VELO}	$\langle N_{\mathrm{VELO}} \rangle$
V	100%-70%	$N_{\mathrm{ch}} < 9$	4.187	$N_{\mathrm{ch}} < 46$	29.818
IV	70%-50%	$9 \leq N_{\mathrm{ch}} < 15$	11.446	$46 \leq N_{\mathrm{ch}} < 65$	55.498
III	50%-30%	$15 \leq N_{\mathrm{ch}} < 22$	18.290	$65 \leq N_{\mathrm{ch}} < 86$	74.587
II	30%-10%	$22 \leq N_{\mathrm{ch}} < 35$	27.718	$86 \leq N_{\mathrm{ch}} < 119$	100.599
I	10%-0%	$35 \leq N_{\mathrm{ch}}$	43.959	$119 \leq N_{\mathrm{ch}}$	145.052

Table 4.1: Definitions of multiplicity classes with respect to the multiplicity estimators N_{BACK} and N_{VELO}. The corresponding event activity percentiles and average charged track multiplicities per class are provided.

To construct the multiplicity-dependent measurements, the signal species yields are in each multiplicity class for both multiplicity estimators.

4.2 Signal Extraction

The goal of this analysis is to probe hadronization effects that may exist at the point of collision, meaning that only prompt candidates should be included in the signal yield estimation. The ϕ and V^0 (Λ and $\mathrm{K}^0_{\mathrm{S}}$) species have combinatoric backgrounds in their mass spectra, thus requiring multiplicity-binned mass fits to extract total yields. The V^0 and long lifetime particles (π^+ and p) have significant contributions of secondary particles (candidates produced by feed-down decays) to their total yields, so care must be taken to separate the prompt and non-prompt candidates. For the most part, this is achieved by performing a fit

to a distribution of the variable $\log \chi^2_{\text{IP}}$ (also written as IPCHI2_OWNPV internal to LHCb). This variable is a measurement of the quality of the reconstructed primary vertex candidate if the signal candidate trajectory is included, which is also proportional to the separation of the signal origin vertex to the primary vertex of the collision. As such, the distribution of prompt candidates (candidates originating from the primary vertex) should be centered close to 0. The prompt signal extraction procedure varies slightly based on the particle species, as such there are three methods used in the course of this analysis.

4.2.1 ϕ

A dearth of secondary ϕ candidates is apparent in this data sample due to the rarity of feed-down decays into $s\bar{s}$ pairs, which is observed in the lack of a secondary peak when plotting the $\log \chi^2_{\text{IP}}$ distribution. This provides the analysis with a clear sample of promptly produced ϕ candidates. For this case, a fit to the mass spectra is required but the prompt fraction (very close to 100%) can be extracted directly from truth-matched Monte-Carlo.

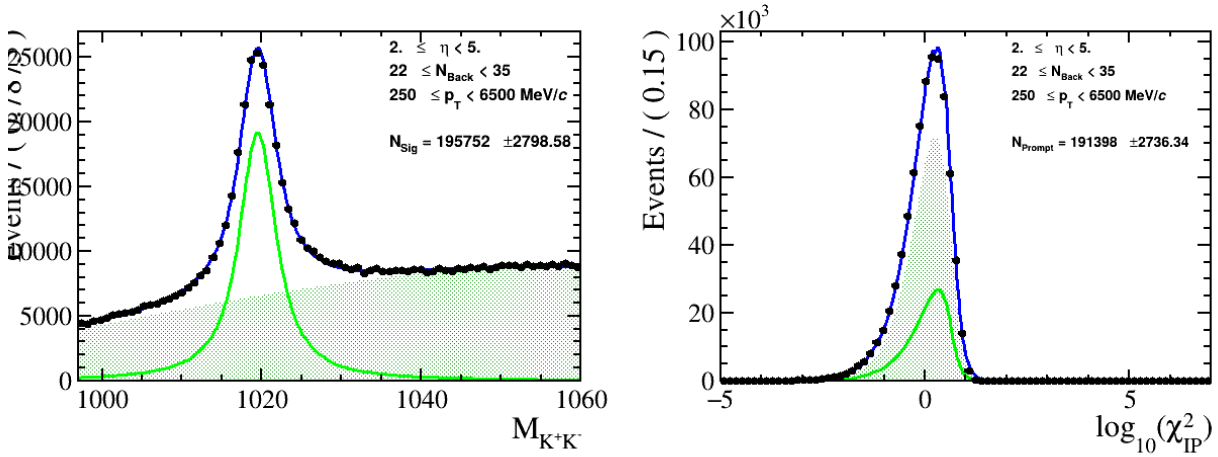


Figure 4.2: Representative simultaneous fit to the mass spectrum (left) and $\log \chi^2_{\text{IP}}$ (right) distributions for ϕ candidates. The total fit (blue), prompt signal fit (green line), and background estimations (green shaded) are provided.

4.2.2 Λ & K^0_{S}

Extracting prompt signal V^0 candidates requires simultaneously fitting to the mass and $\log \chi^2_{\text{IP}}$ distributions. First, fits are performed on each contribution to the mass and $\log \chi^2_{\text{IP}}$ distributions in Monte-Carlo to ascertain the most appropriate functions.

- **Prompt Signal**. The mass signal peaks for both Λ and K^0_{S} can be represented well with a Voigtian fit.

A Bukin distribution centered close to 0 is used to fit the prompt candidates with respect to $\log \chi^2_{\text{IP}}$.

- **Non-prompt Signal**. Voigtian line-shapes using the same means as the prompt signal fits are generated to characterize the secondary signal candidates. A (Two-) Gaussian line-shape, generally centered above 0 in $\log \chi^2_{\text{IP}}$, is used to fit the secondary components for (K^0_S) Λ.

- **Background**. The combinatoric background for the mass distributions of both V^0 species can be represented by third-order Chebychev polynomial functions.

  Since the combinatoric background is made up of improperly matched daughter candidates, these V^0 candidates generally have very little impact on PV reconstruction, and therefore exist further out in $\log \chi^2_{\text{IP}}$ and correspond to a very irregular line-shape. To account for this, a Gaussian Kernel-Density Estimation(32; 33; 34; 35) (KDE) is performed simultaneously with the mass background fit.

4.2.2.1 Kernel Density Estimation

In order to model the distribution of the combinatoric background with respect to the $\log \chi^2_{\text{IP}}$ variable, non-parametric methods are utilized. For the purposes of this analysis, the V^0 sidebands are approximated with a Gaussian Kernel-Density Estimation. This is accomplished by representing the individual $\log \chi^2_{\text{IP}}$ entries of the V^0 candidates outside of the mass peak region as Gaussians of fixed width (ρ). By normalizing the sum of the Gaussians, a smoothed probability distribution is generated and can be used as a template when fitting to the entire data set.

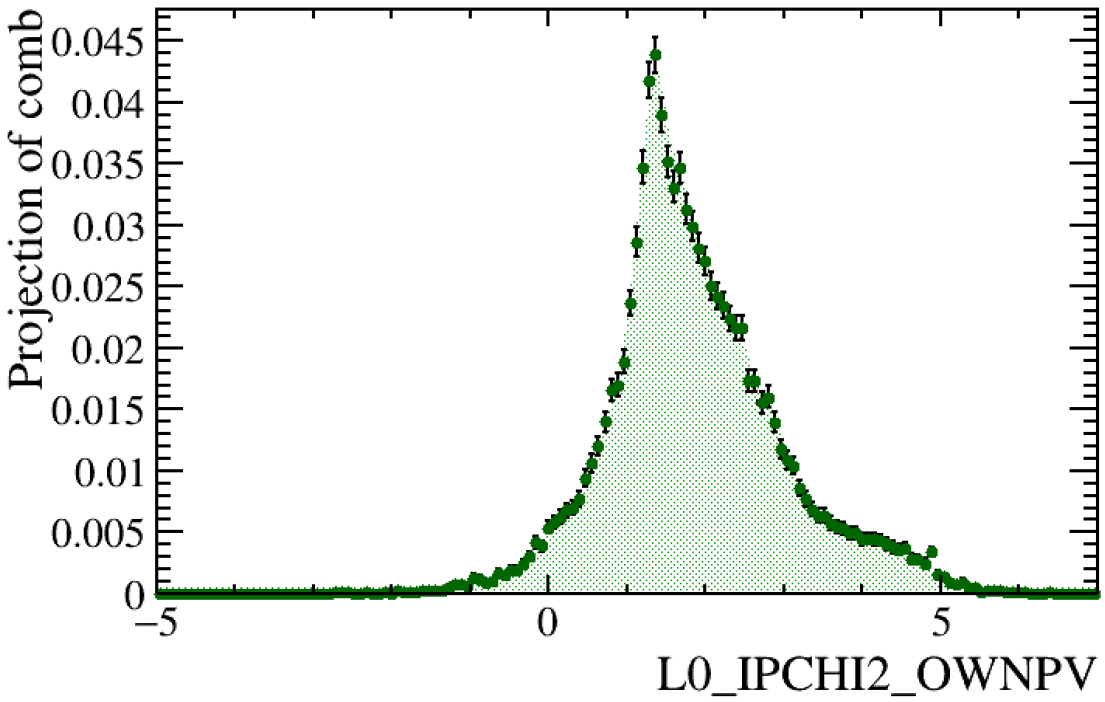


Figure 4.3: Example of a normalized $\log \chi^2_{\text{IP}}$ distribution from the Λ mass background (Circles) and the corresponding KDE(32; 33; 34; 35) (Shaded).

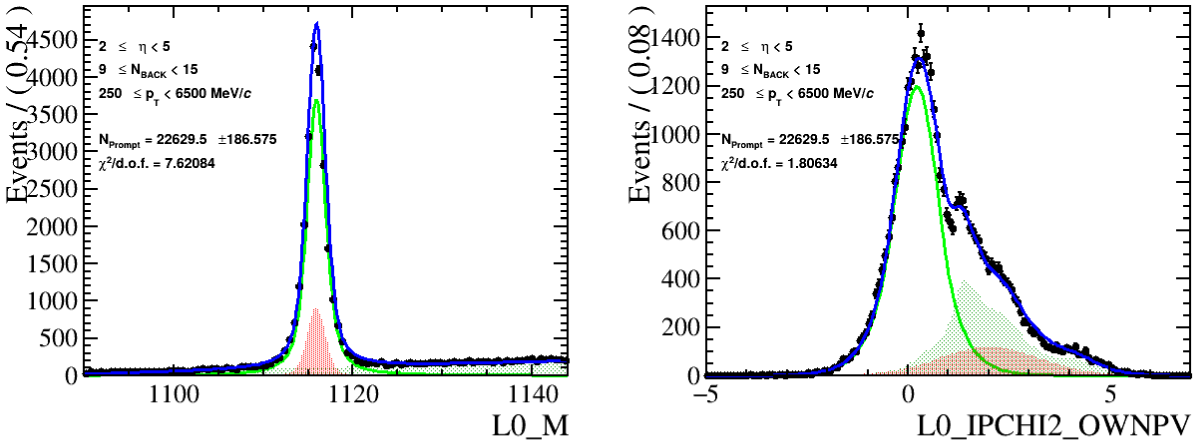


Figure 4.4: Representative simultaneous fit to the mass spectrum (left) and $\log \chi^2_{\text{IP}}$ (right) distributions for Λ candidates. The total fit (blue), prompt signal fit (green line), secondary signal fit (red shaded), and background estimations (green shaded) are provided.

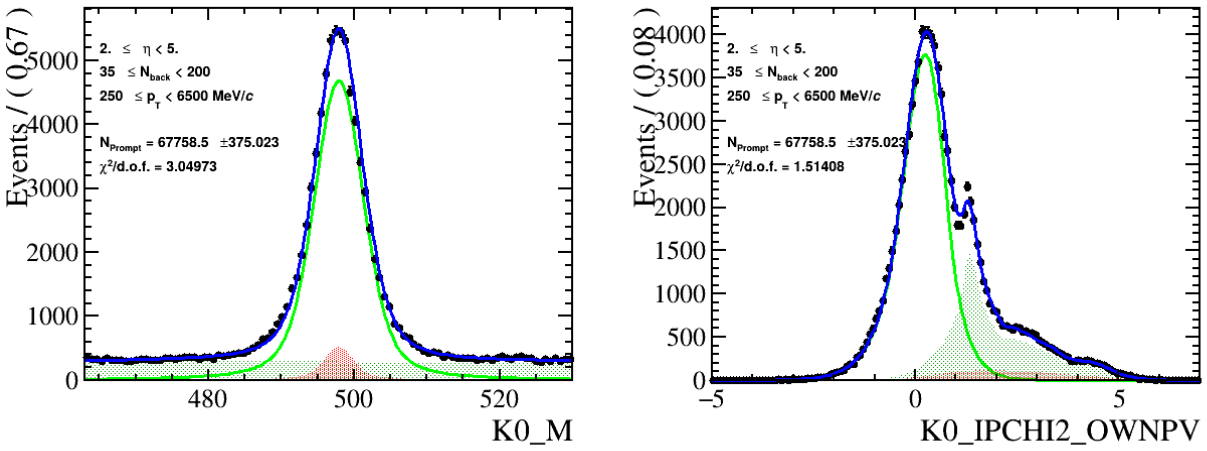


Figure 4.5: Representative simultaneous fit to the mass spectrum (left) and $\log \chi^2_{\text{IP}}$ (right) distributions for K^0_S candidates. The total fit (blue), prompt signal fit (green line), secondary signal fit (red shaded), and background estimations (green shaded) are provided.

4.2.3 π^+ & p

Since π^+ and p candidates do not decay within the detector, there is no combinatoric background to be concerned with (mis-ID contamination is addressed with PID selection and efficiency corrections). Similar to the case of the ϕ candidates, only one fit is required to extract a prompt signal estimate. A fit to the $\log \chi^2_{\text{IP}}$ distribution is performed in a similar fashion to the V^0 candidates, without the inclusion of a KDE estimate for the combinatoric background.

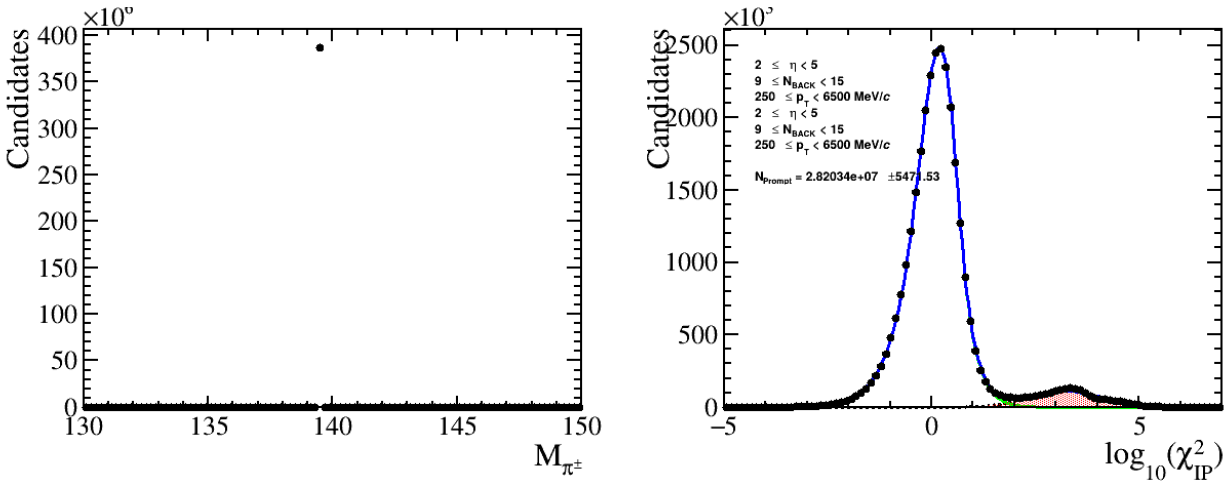


Figure 4.6: Representative plot of the mass distribution (left) and $\log \chi^2_{\text{IP}}$ distribution (right) for $\pi^\pm$ candidates. The total fit (blue), prompt signal fit (green line), and secondary signal fit (red shaded) are provided.

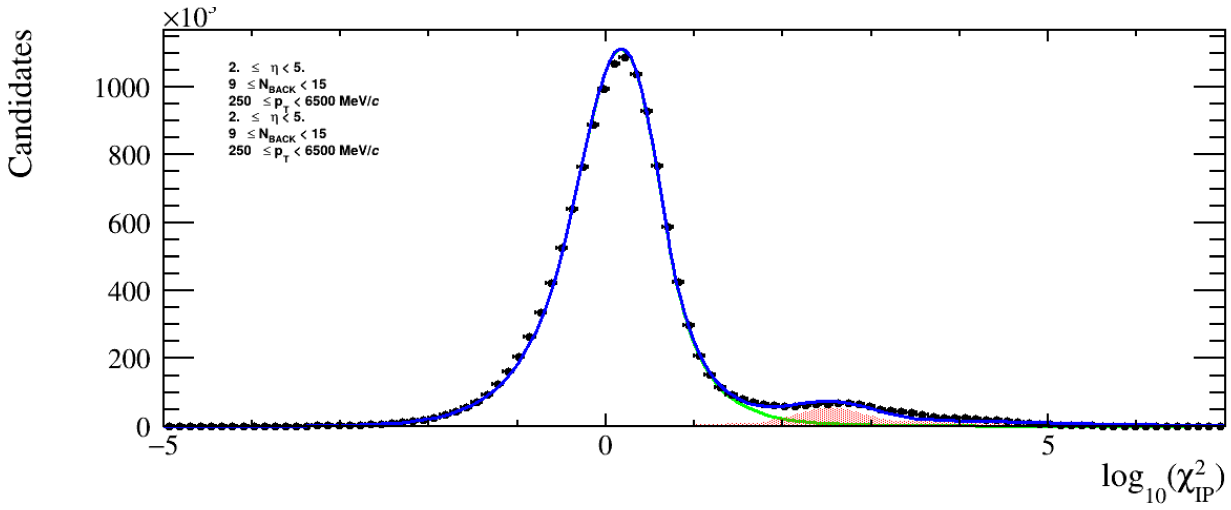


Figure 4.7: Representative the $\log \chi^2_{\text{IP}}$ distribution for p candidates. The total fit (blue), prompt signal fit (green line), and secondary signal fit (red shaded) are provided.

4.3 Efficiencies and Corrections

4.3.1 Particle Identification

To account for misidentified tracks as well as true particle candidates that missed the particle identification criteria, particle identification efficiencies (ε_{PID}) must be generated for the final state particles. Since major contributors to PID performance are related to

subdetector saturation, the relevant PID efficiencies are calculated with respect to detector occupancy. The default efficiencies produced from the dedicated LHCb package, PIDCalib, are calculated with respect to the number of hits in the SPD (i.e. SPDHits).

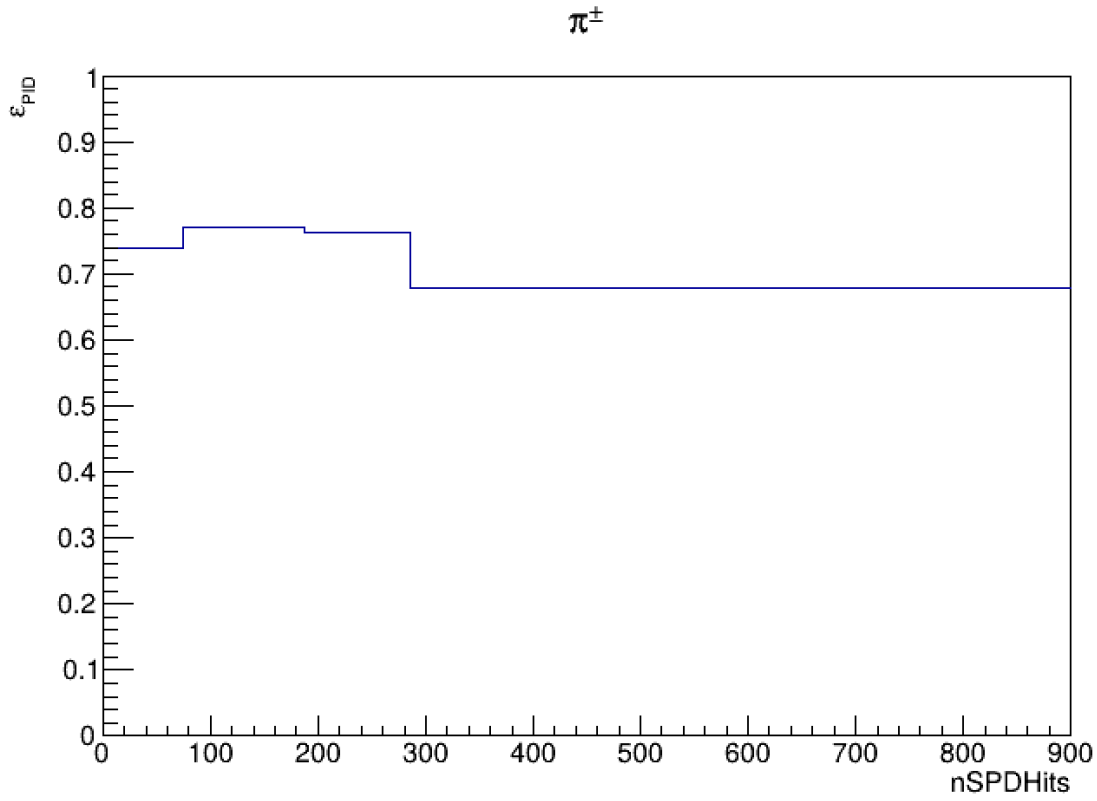


Figure 4.8: Particle identification efficiencies corresponding to the relevant charged pion cuts from section 3.1.

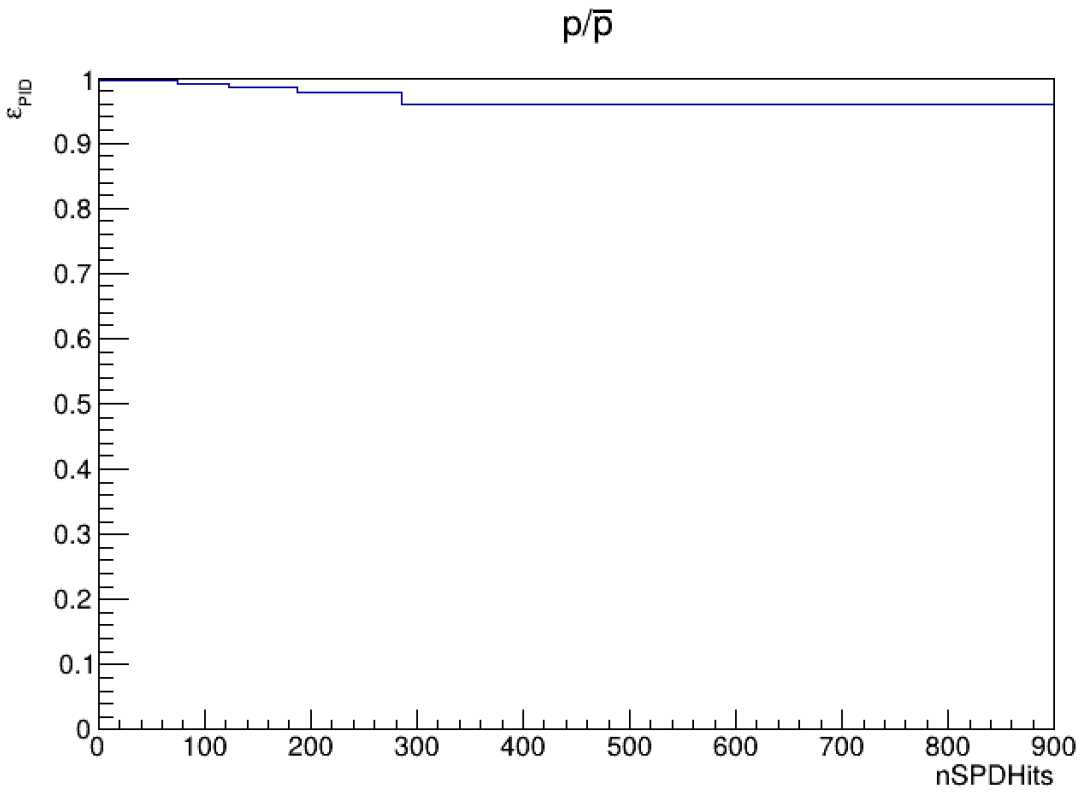


Figure 4.9: Particle identification efficiencies corresponding to the relevant proton cuts from section 3.1.

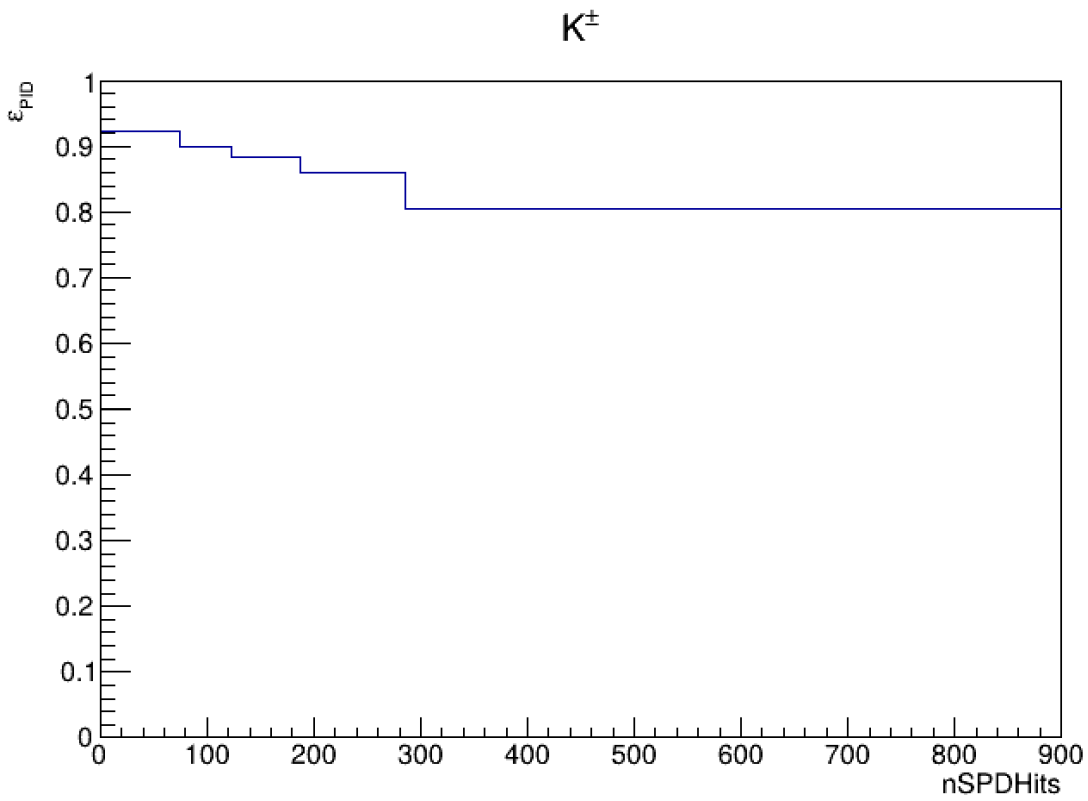


Figure 4.10: Particle identification efficiencies corresponding to the relevant charged kaon cuts from section 3.1.

Since the yield ratio measurements will be provided with respect to backwards and VELO tracks, these $\varepsilon_{\mathrm{PID}}$ distributions are rebinned into the relevant multiplicity distributions. For the decaying species (Λ, $\mathrm{K}^0_{\mathrm{S}}$, ϕ) the PID efficiency is calculated by averaging the combined daughter PID efficiencies over the total number of decay candidates.

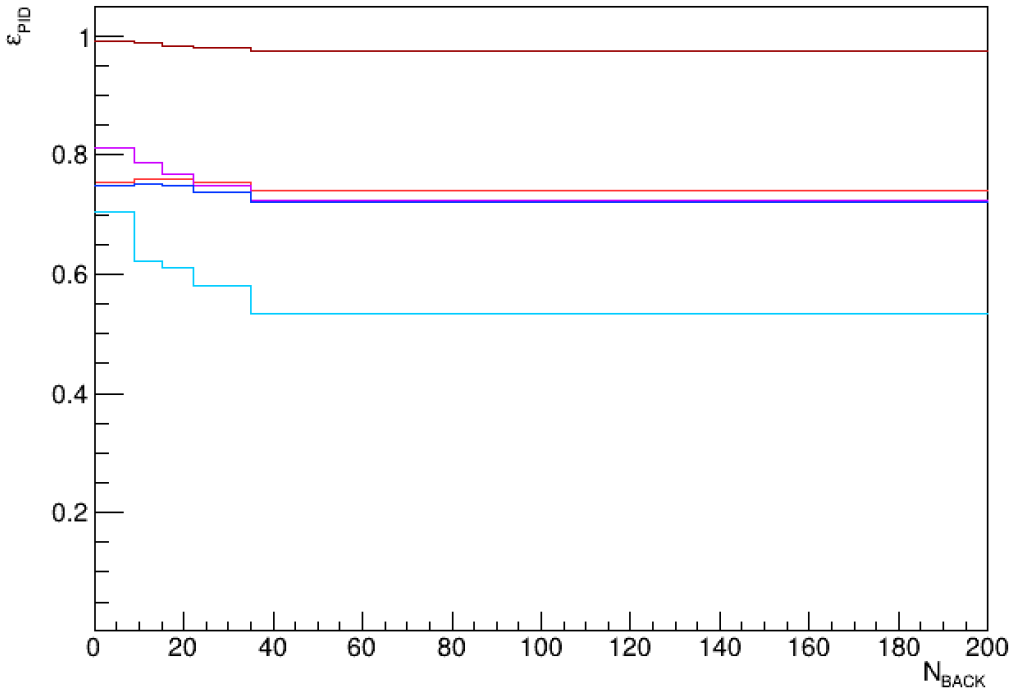


Figure 4.11: Rebinned particle identification efficiencies for signal candidates matching the selection criteria written out in section 3.1. The listed species are the (Red) charged pion, (Dark Red) p, (Cyan) K^0_S, (Blue) Λ, and (Violet) ϕ

ε_{PID}					
Multiplicity Class	π^+	p	Λ	K^0_S	ϕ
V	0.754	0.991	0.748	0.704	0.811
IV	0.760	0.988	0.751	0.623	0.788
III	0.760	0.984	0.749	0.612	0.769
II	0.754	0.980	0.738	0.581	0.750
I	0.740	0.975	0.720	0.535	0.725

Table 4.2: Summary of representative particle identification efficiencies for signal candidates. The provided efficiencies are for the dataset taken with downward magnet polarity and with respect to N_{BACK} specifically. The complete summary of efficiencies is provided in appendix D.

4.3.2 Tracking Performance Correction

Generally Monte-Carlo simulations of the LHCb detector and its reconstruction algorithms are reliable, however there have been known discrepancies between tracking performance in real and simulated events. To account for this, tracking efficiencies for common final state particles are calculated in Monte-Carlo and with data-driven methods in collider events using to a standard LHCb procedure. Ratios of these efficiencies, $w_{tracking}$, are obtained from the trackcalib package to match the tracking performance of Monte-Carlo to that of real events before calculating a reconstruction and selection efficiency as depicted in equation 4.1 . These weights are applied per bin of multiplicity and per final state track in acceptance.

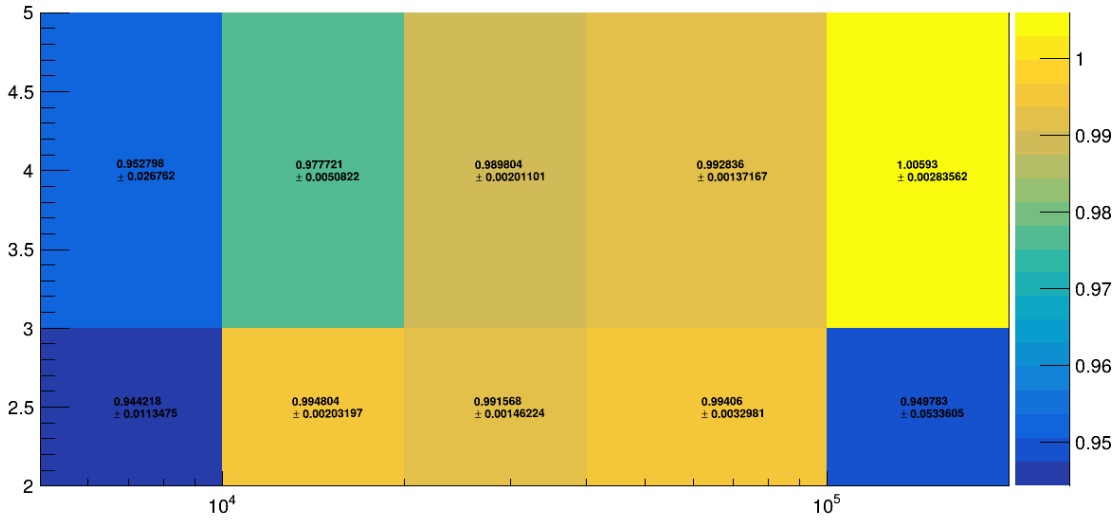


Figure 4.12: Table of tracking efficiency corrections for $2 \leq \eta_{\text{track}} \leq 5$ and $2\ \text{GeV}/c \leq p_{\text{track}} \leq 200\ \text{GeV}/c$ in MagDown pp collisions from 2015.

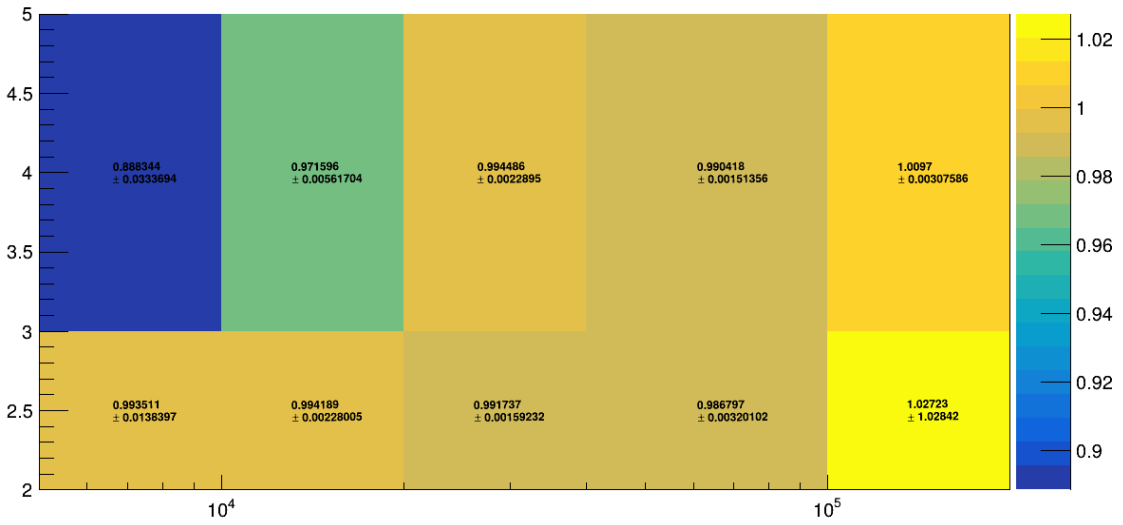


Figure 4.13: Table of tracking efficiency corrections for $2 \leq \eta_{\text{track}} \leq 5$ and $2\ \text{GeV}/c \leq p_{\text{track}} \leq 200\ \text{GeV}/c$ in MagUp pp collisions from 2015.

4.3.3 Corrections to Monte-Carlo

The Monte-Carlo event and candidate reconstruction algorithms generally exhibit strong agreement with the output of the real reconstruction process in collider data. However, small disagreements between Monte-Carlo in how subdetector geometries are modeled, how particles interact with detector material, and physics assumptions regarding track kinematics and multiplicity can manifest into discrepancies in the distributions of the reconstructed signal hadrons. Discrepancies in track interactions with detector material is accounted for in the tracking efficiency corrections from section 4.3.2. To account for discrepancies in reconstructed particles regarding kinematics and occupancy, additional weights are generated to bring the Monte-Carlo distributions into agreement with collider data before calculating the reconstruction and selection efficiencies (see section 4.3.4).

4.3.4 Reconstruction and Selection Efficiency

In order to quantify the effects of the selection cuts and reconstruction algorithms, a reconstruction and selection efficiency, $\varepsilon_{Rec\&Sel}$, is calculated in Monte-Carlo. This efficiency is calculated by comparing the corrected distribution of reconstructed Monte-Carlo yields to the generated Monte-Carlo production in the same acceptance region. The efficiency for a signal species decaying into two charged daughter tracks ($X_{sig} \to D^+D^-$) is described in equation 4.1.

$$\varepsilon_{Rec\&Sel}(\text{mult.}) = \frac{\sum X_{sig,\ \text{Rec}}\ \&\ D^+\ \&\ D^-\ \text{in Acceptance} \times w_{RW}(\text{mult.}) \times w^+_{tracking}(p,\eta) \times w^-_{tracking}(p,\eta)}{\sum X_{sig,\ \text{Gen}}\ \&\ D^+\ \&\ D^-\ \text{in Acceptance} \times w_{RW}(\text{mult.},p,\eta)} \quad (4.1)$$

Here, w_{RW} corresponds to a reweighting correction to account for known discrepancies between Monte-Carlo and collider data, while $w^{\pm}_{tracking}$ is a correction to their Monte-Carlo tracking efficiency for the charged daughter tracks. Since Monte-Carlo simulations are relied on for calculating $\varepsilon_{Rec\&Sel}$ rather than data-driven methods, it is necessary to use these corrections to bring the simulated candidates into agreement with the candidates from collider data in order to accurately represent the true efficiency of the true reconstruction algorithms. The reconstructed Monte-Carlo signal candidates, $X_{sig,\ \text{Rec}}$, have passed the same selection criteria as their corresponding collider candidates. For non-decaying signal particles (p,π^+), it is only necessary for the signal candidate to be in acceptance since there is no daughter track and the tracking correction is applied directly to the signal track.

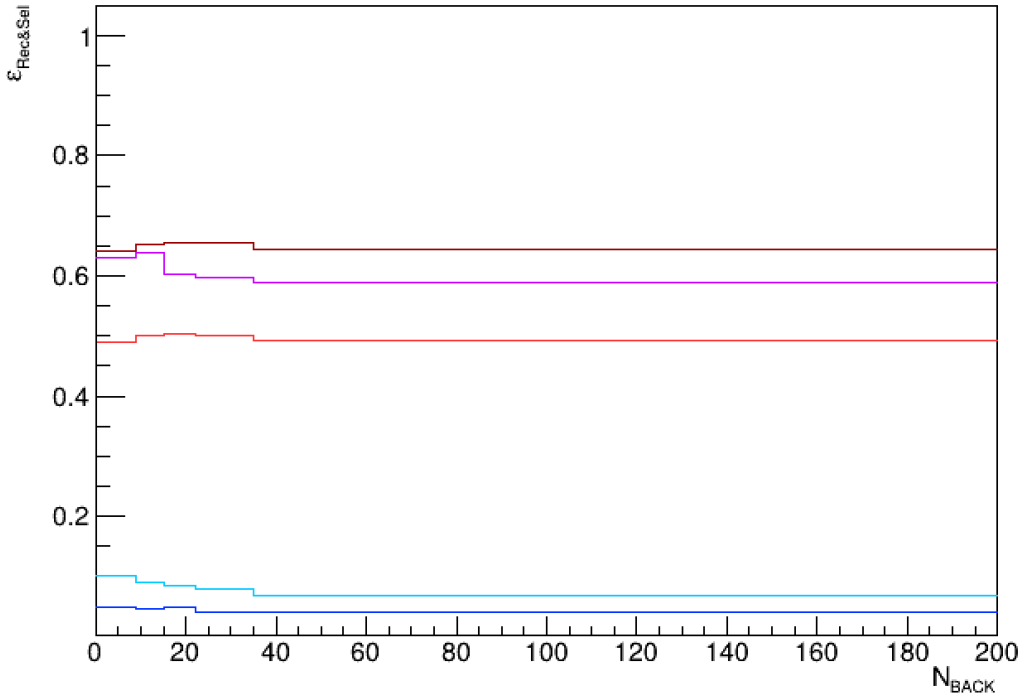


Figure 4.14: Reconstruction and selection efficiencies for signal candidates matching the selection criteria written out in section 3.1. The listed species are the (Red) charged pion, (Dark Red) p, (Cyan) K^0_S, (Blue) Λ, and (Violet) ϕ

$\varepsilon_{Rec\&Sel}$					
Multiplicity Class	π^+	p	Λ	K^0_S	ϕ
V	0.489	0.642	0.050	0.087	0.630
IV	0.501	0.653	0.045	0.082	0.638
III	0.503	0.655	0.050	0.078	0.602
II	0.500	0.654	0.042	0.066	0.597
I	0.492	0.645	0.040	0.051	0.590

Table 4.3: Summary of representative reconstruction and selection efficiencies for signal candidates. The provided efficiencies are for the dataset taken with downward magnet polarity and with respect to N_{BACK} specifically. The complete summary of efficiencies is provided in appendix D.

4.3.5 Acceptance Correction

Due to the geometric and kinematic limitations of the LHCb spectrometer, corrections need to be made to account for hadrons that meet the signal criteria but were not reconstructed due to one or more daughter tracks leaving the phase space covered by the experiment. The geometric coverage for long tracks is $2 \leq \eta \leq 5$, while the minimum (transverse) momentum needed for a charged particle to not bend out of the geometric acceptance is (200 MeV/c) 2 GeV/c. The acceptance efficiency, ε_{acc}, is the ratio described in equation 4.2.

$$\varepsilon_{acc}(\text{mult.}) = \frac{\sum X_{sig} \ \& \ D^+ \ \& \ D^- \text{ in Acceptance}}{\sum X_{sig} \text{ in Acceptance}} \tag{4.2}$$

Where X_{sig} is the reconstructed signal candidate generated in Monte-Carlo and $D^{\pm}$ are the corresponding charged daughter tracks. This ratio is calculated as a function of multiplicity in either N_{VELO} or N_{BACK}. For non-decaying particles (p, π^+), there is no acceptance correction necessary since the signal tracks are directly reconstructed.

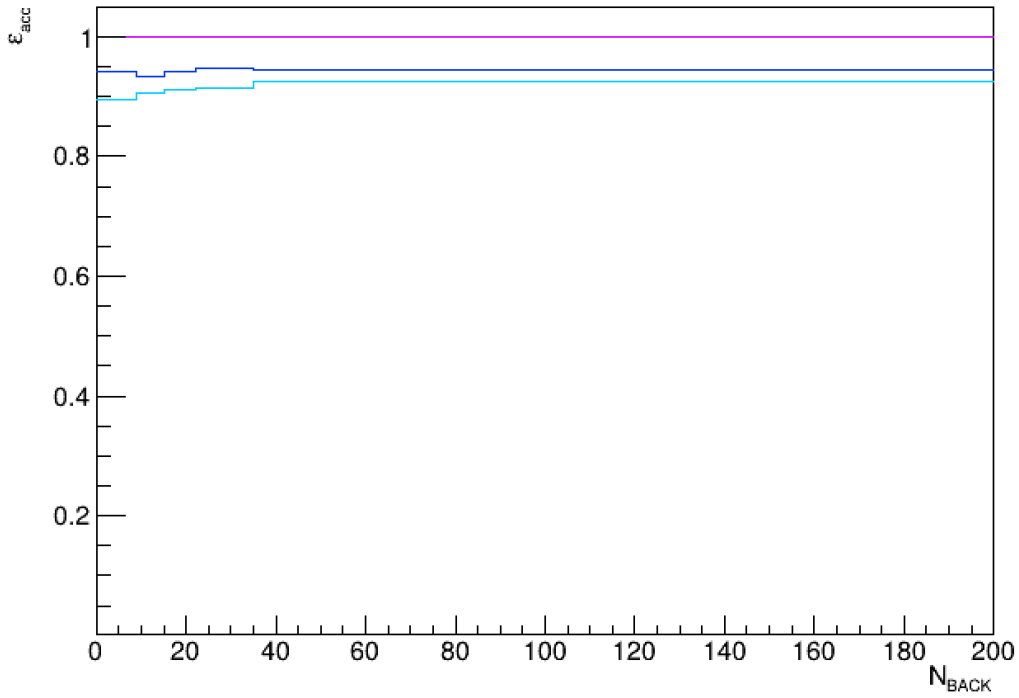


Figure 4.15: Acceptance efficiencies for signal candidates matching the selection criteria written out in section 3.1. The listed species are (Cyan) K^0_S, (Blue) Λ, and (Violet) ϕ

ε_{acc}			
Multiplicity Class	Λ	K^0_S	ϕ
V	0.941	0.896	0.998
IV	0.932	0.907	0.998
III	0.941	0.910	0.999
II	0.946	0.913	0.999
I	0.944	0.925	0.999

Table 4.4: Summary of representative acceptance efficiencies for signal candidates. The provided efficiencies are for the dataset taken with downward magnet polarity and with respect to N_{BACK} specifically. The complete summary of efficiencies is provided in appendix D.

4.4 Systematic Uncertainties

The primary sources of systematic uncertainties in the yield measurements originate from the prompt signal estimation and the efficiency corrections applied. In this section, these uncertainties are quantified. These values are applied to the final results, per multiplicity class.

4.4.1 Signal Extraction

Extracting the prompt signal yield is strongly dependent on the quality of the fit to the mass and/or $\log \chi^2_{\mathrm{IP}}$ distribution(s). To account for error in the fit template, systematic uncertainties are generated for each free fitting parameter in the nominal fits. The nominal results are compared to yields obtained by setting each parameter to its maximally and minimally allowed values based on the fit uncertainty to the Monte-Carlo signal distributions, and the percent errors from the nominal values are taken as the uncertainties. Choice of lineshape uncertainties are also generated by comparing the nominal results to the performance of similar functional forms. For each bin, the largest percent error across all of the alternative fits is taken as the systematic uncertainty. The uncertainties are all strictly below 20%, however most values are consistently below 7%.

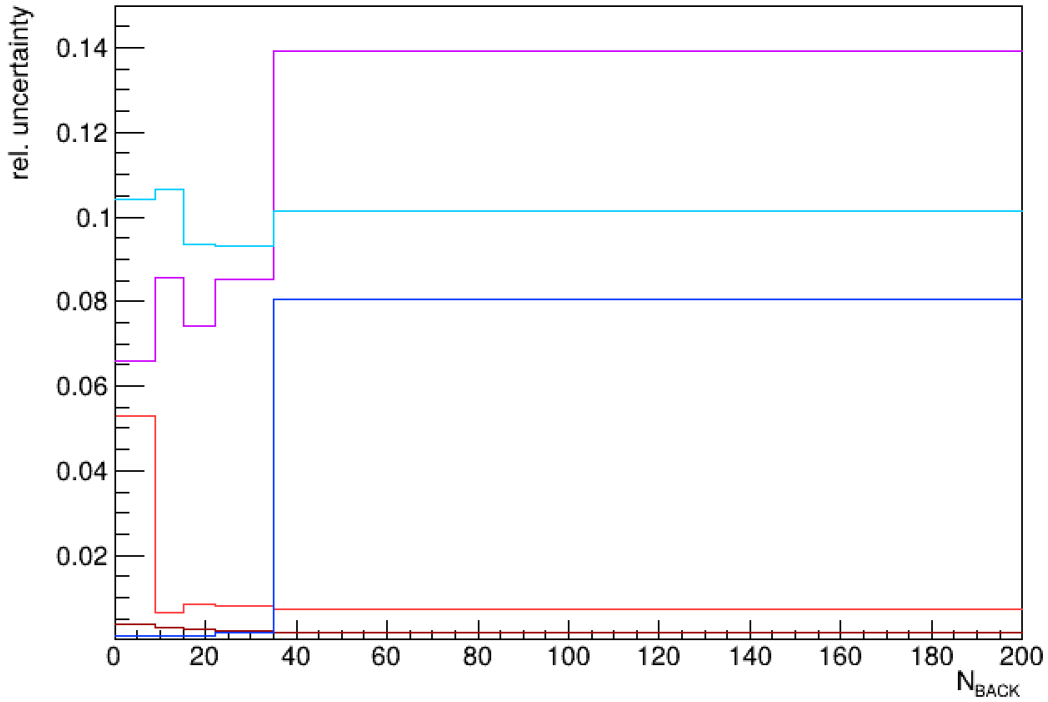


Figure 4.16: Relative systematic errors originating from the fits to the mass and/or log χ^2_{IP} distributions. The listed species are the (Red) charged pion, (Dark Red) p, (Cyan) $\mathrm{K}^0_{\mathrm{S}}$, (Blue) Λ, and (Violet) ϕ

Systematic uncertainties from the Signal Extraction Fits					
Multiplicity Class	π^+	p	Λ	$\mathrm{K}^0_{\mathrm{S}}$	ϕ
V	0.489 %	0.370 %	0.004 %	10.422 %	6.607 %
IV	0.501 %	0.297 %	0.006 %	10.633 %	8.545 %
III	0.503 %	0.244 %	0.003 %	9.335 %	7.419 %
II	0.500 %	0.195 %	0.188 %	9.299 %	8.531 %
I	0.492 %	0.194 %	8.041 %	10.148 %	13.926 %

Table 4.5: Summary of representative systematic uncertainties originating from the fit templates for signal candidates. The provided uncertainties are for the dataset taken with downward magnet polarity and with respect to N_{BACK} specifically. The complete summary of systematic uncertainties is provided in appendix E.

4.4.2 Uncertainties from Efficiencies

There are uncertainties associated with identification and track reconstruction performance. The tracking efficiency correction tables from sec.4.3.2 as well as the PID efficiencies from sec.4.3.1 contain uncertainties produced from the TrackCalib and PIDCalib packages respectively. The uncertainty from the Geometric acceptance efficiency is calculated from generated Monte-Carlo with a binomial error formula. The relative size of their propagated uncertainties are provided here.

4.4.2.1 Tracking Systematics

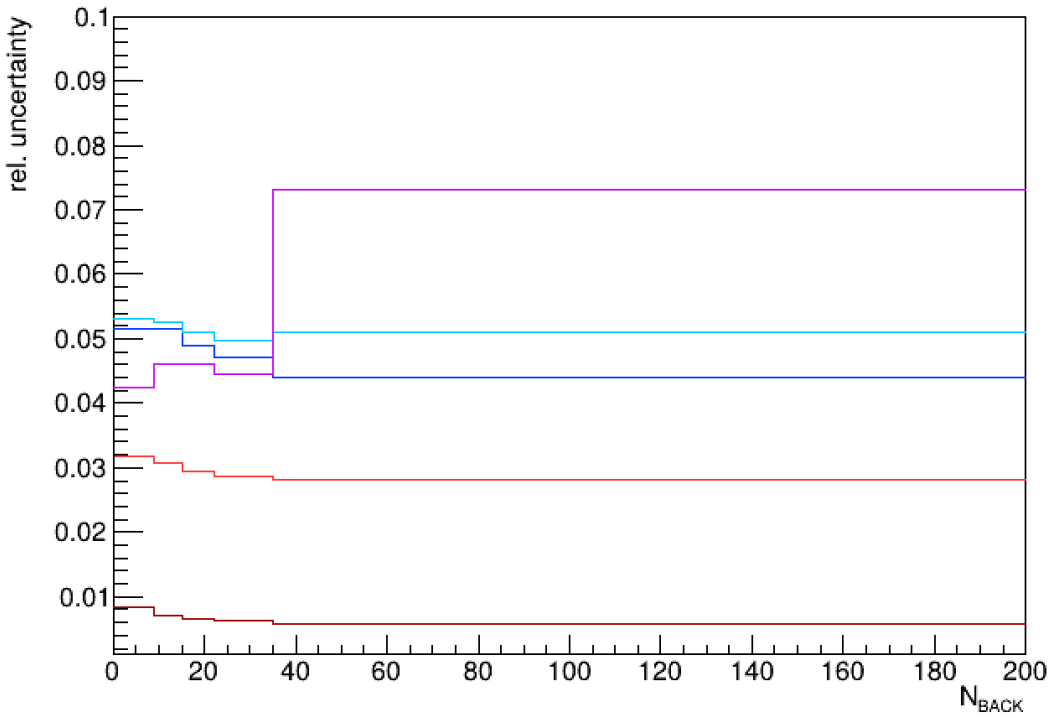


Figure 4.17: Relative systematic errors originating from final state tracking corrections. The listed species are the (Red) charged pion, (Dark Red) p, (Cyan) K^0_S, (Blue) Λ, and (Violet) ϕ

Systematic uncertainties from the Tracking Corrections					
Multiplicity Class	π^+	p	Λ	K^0_S	ϕ
V	3.189 %	0.830 %	5.143 %	5.368 %	4.244 %
IV	3.065 %	0.716 %	5.153 %	5.253 %	4.619 %
III	2.956 %	0.663 %	4.890 %	5.100 %	4.597 %
II	2.868 %	0.622 %	4.712 %	4.964 %	4.444 %
I	2.802 %	0.591 %	4.408 %	5.107 %	7.305 %

Table 4.6: Summary of representative systematic uncertainties originating from tracking efficiency corrections provided by TrackCalib. The provided uncertainties are for the dataset taken with downward magnet polarity and with respect to N_{BACK} specifically. The complete summary of systematic uncertainties is provided in appendix E.

4.4.2.2 Particle Identification Systematics

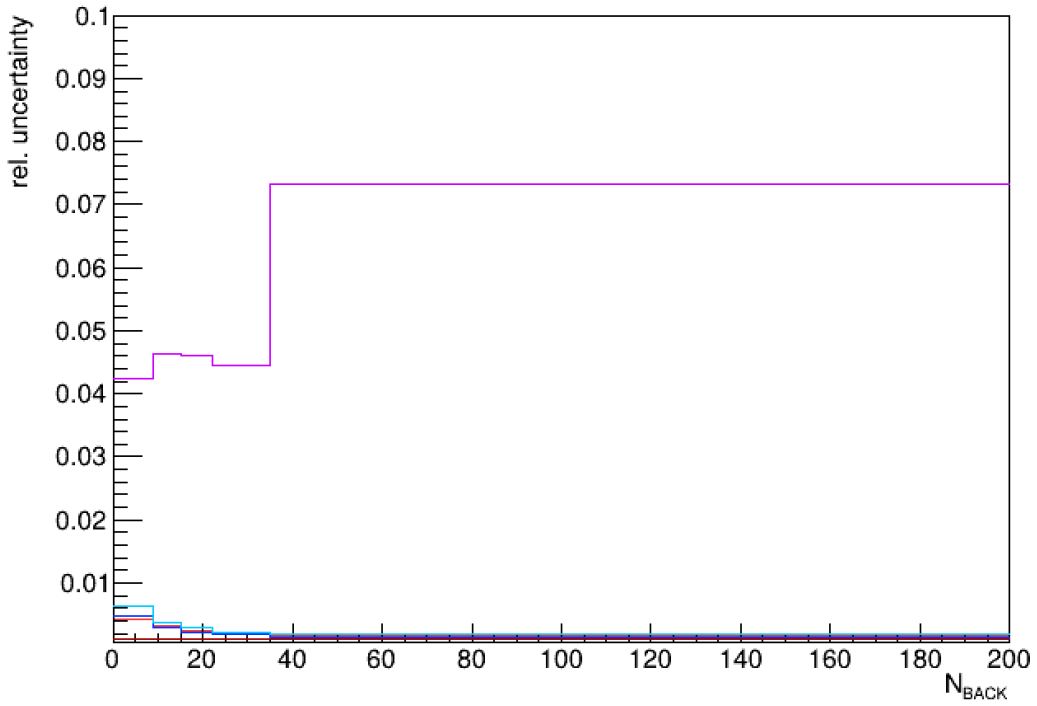


Figure 4.18: Relative systematic errors originating from the uncertainties on the particle identification efficiency from PIDCalib. The listed species are the (Red) charged pion, (Dark Red) p, (Cyan) K^0_S, (Blue) Λ, and (Violet) ϕ

Systematic uncertainties from PID Efficiencies					
Multiplicity Class	π^+	p	Λ	K^0_S	ϕ
V	0.435 %	0.113 %	0.473 %	0.636 %	4.245 %
IV	0.320 %	0.096 %	0.296 %	0.383 %	4.621 %
III	0.255 %	0.084 %	0.228 %	0.287 %	4.600 %
II	0.207 %	0.074 %	0.182 %	0.230 %	4.448 %
I	0.169 %	0.065 %	0.146 %	0.187 %	7.313 %

Table 4.7: Summary of representative systematic uncertainties originating from particle identification efficiencies provided by PIDCalib. The provided uncertainties are for the dataset taken with downward magnet polarity and with respect to N_{BACK} specifically. The complete summary of systematic uncertainties is provided in appendix E.

4.4.3 Acceptance Efficiency Systematics

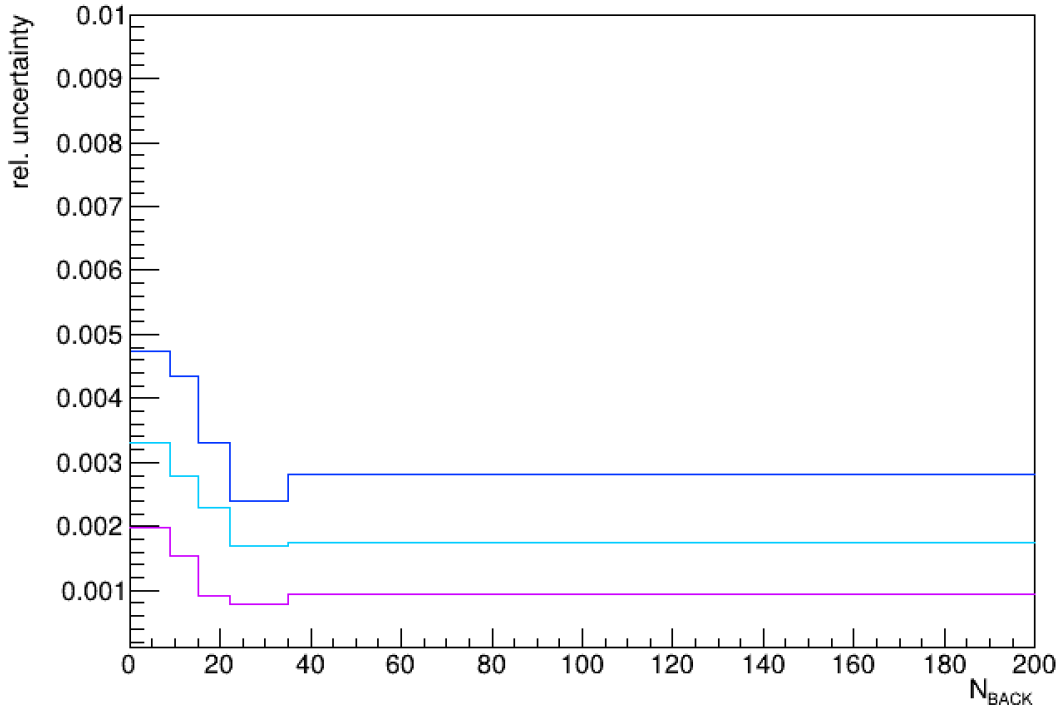


Figure 4.19: Relative systematic errors originating from the uncertainties on the Monte-Carlo acceptance fractions for signal candidates. The listed species are (Cyan) K^0_S, (Blue) Λ, and (Violet) ϕ

ε_{acc}			
Multiplicity Class	Λ	K^0_S	ϕ
V	0.474 %	0.331 %	0.199 %
IV	0.434 %	0.279 %	0.155 %
III	0.332 %	0.230 %	0.092 %
II	0.240 %	0.169 %	0.078 %
I	0.281 %	0.176 %	0.094 %

Table 4.8: Summary of representative systematic errors originating from uncertainties on daughter acceptance fractions. The provided efficiencies are for the dataset taken with downward magnet polarity and with respect to N_{BACK} specifically. The complete summary of efficiencies is provided in appendix E.

CHAPTER 5

Results and Discussion

Following the analysis procedure and corrections outlined in chapter 4, the final yields and ratios shall be reported below. Given that the ultimate goal of this analysis is to compute ratios of the extracted particle yields, no additional corrections regarding the Minimum Bias prescaling factor were necessary, meaning that the following yields do not represent invariant cross-sections for the signal species.

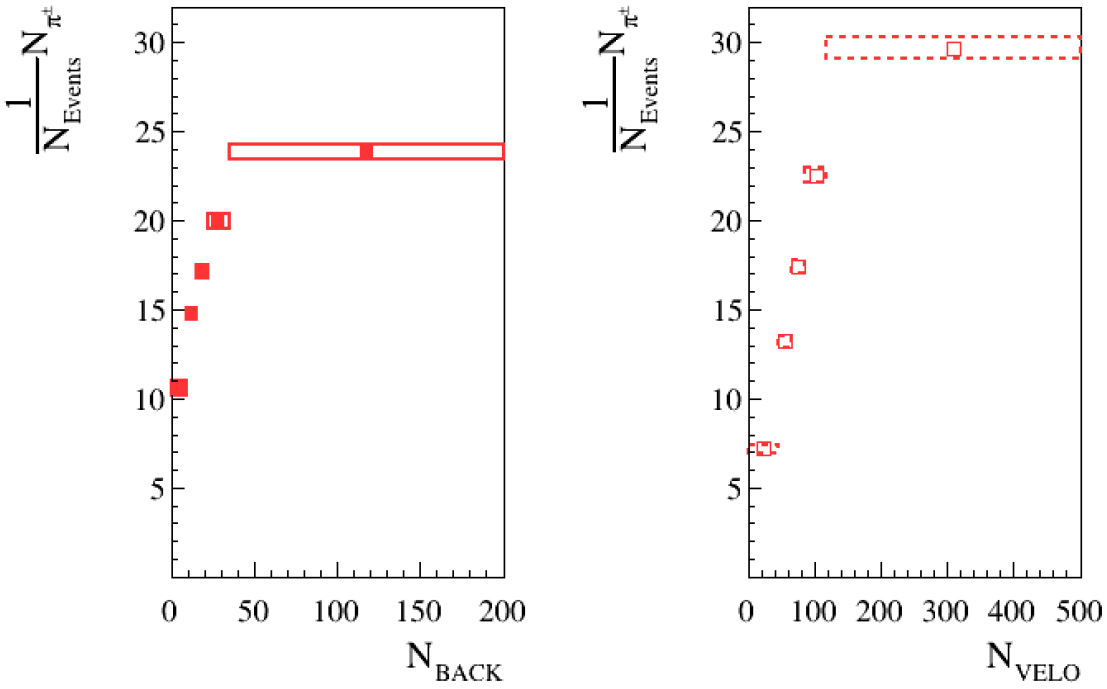


Figure 5.1: Multiplicity-dependent per-event yields of prompt charged pions with respect to (left) backwards tracks and (right) all VELO tracks.

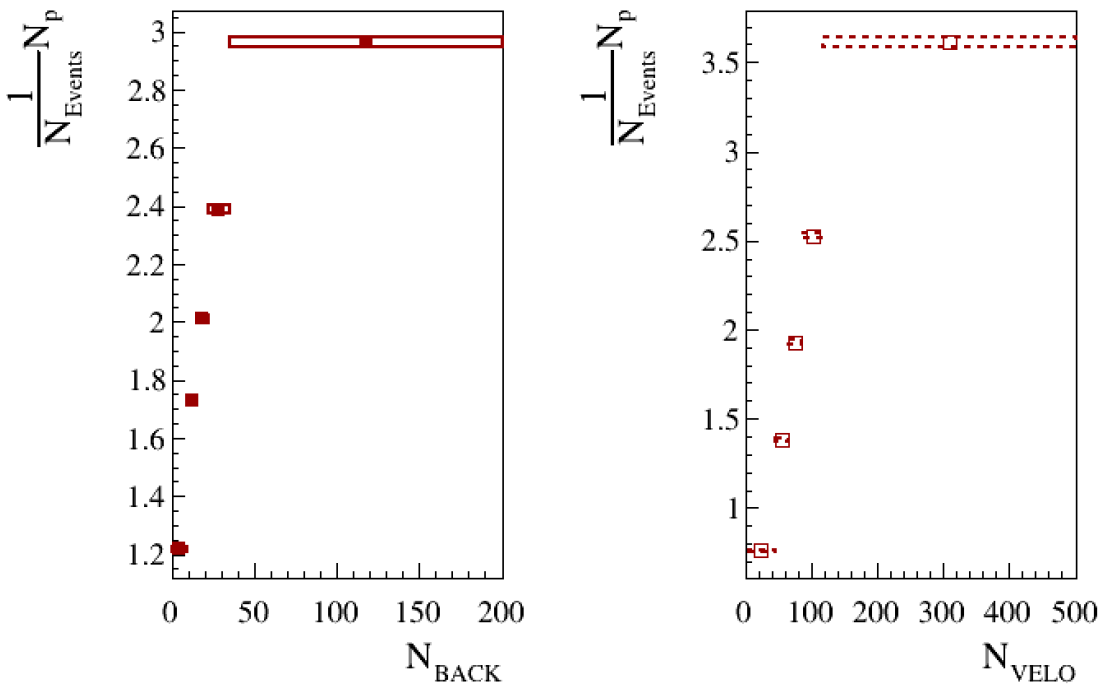


Figure 5.2: Multiplicity-dependent per-event yields of prompt protons with respect to (left) backwards tracks and (right) all VELO tracks.

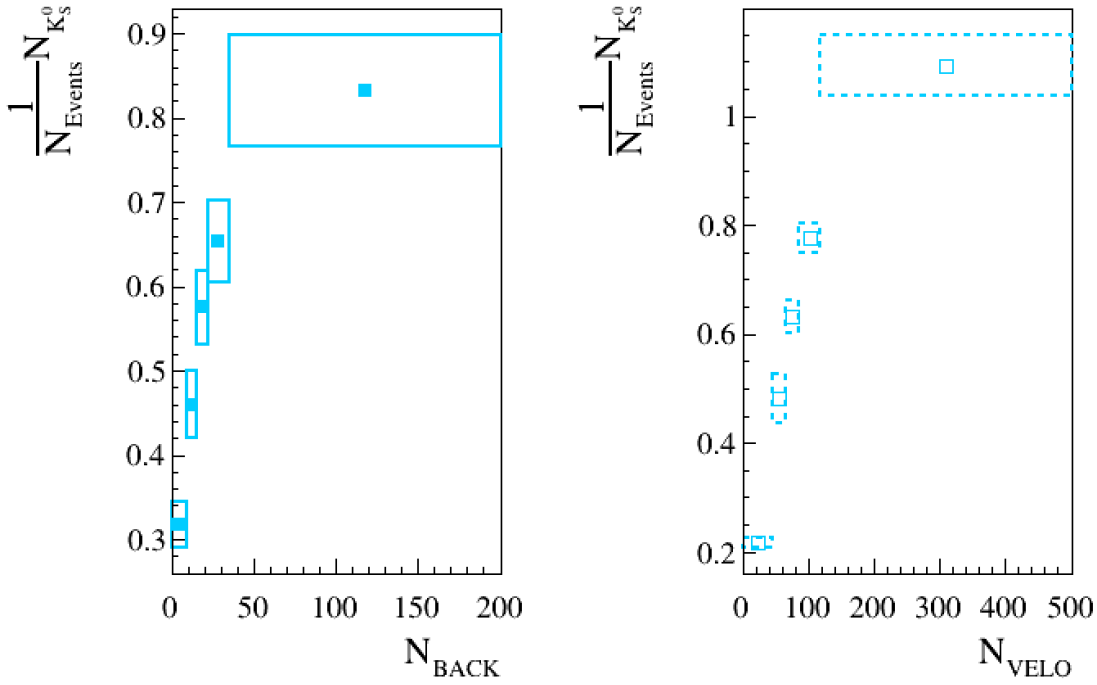


Figure 5.3: Multiplicity-dependent per-event yields of prompt K^0_S mesons with respect to (left) backwards tracks and (right) all VELO tracks.

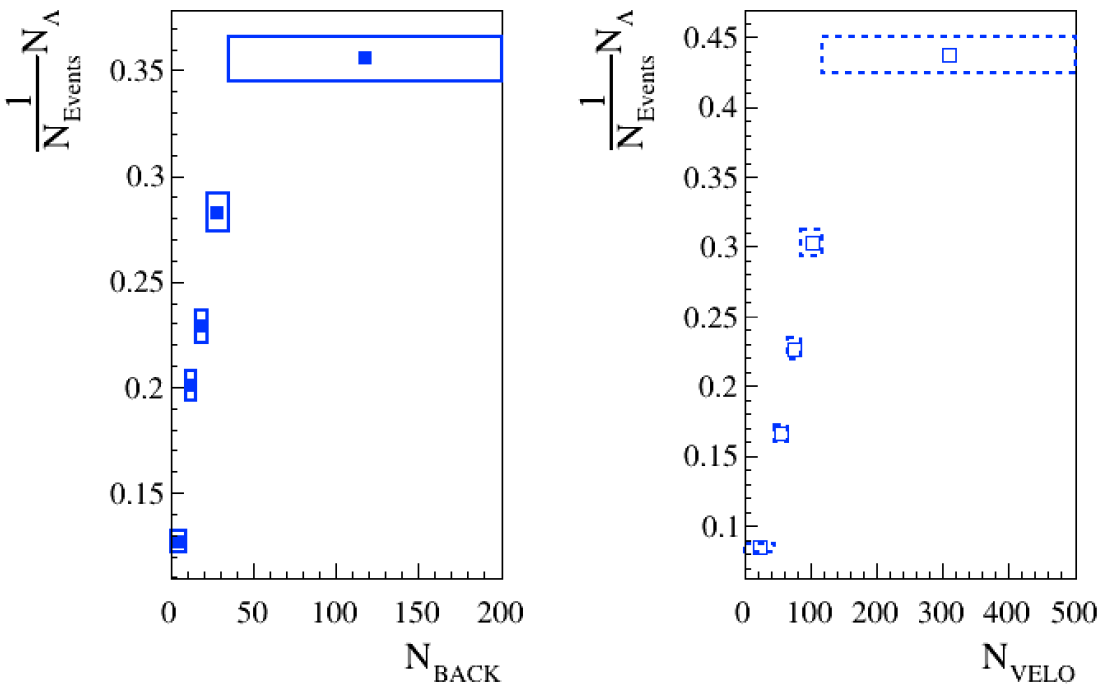


Figure 5.4: Multiplicity-dependent per-event yields of prompt Λs with respect to (left) backwards tracks and (right) all VELO tracks.

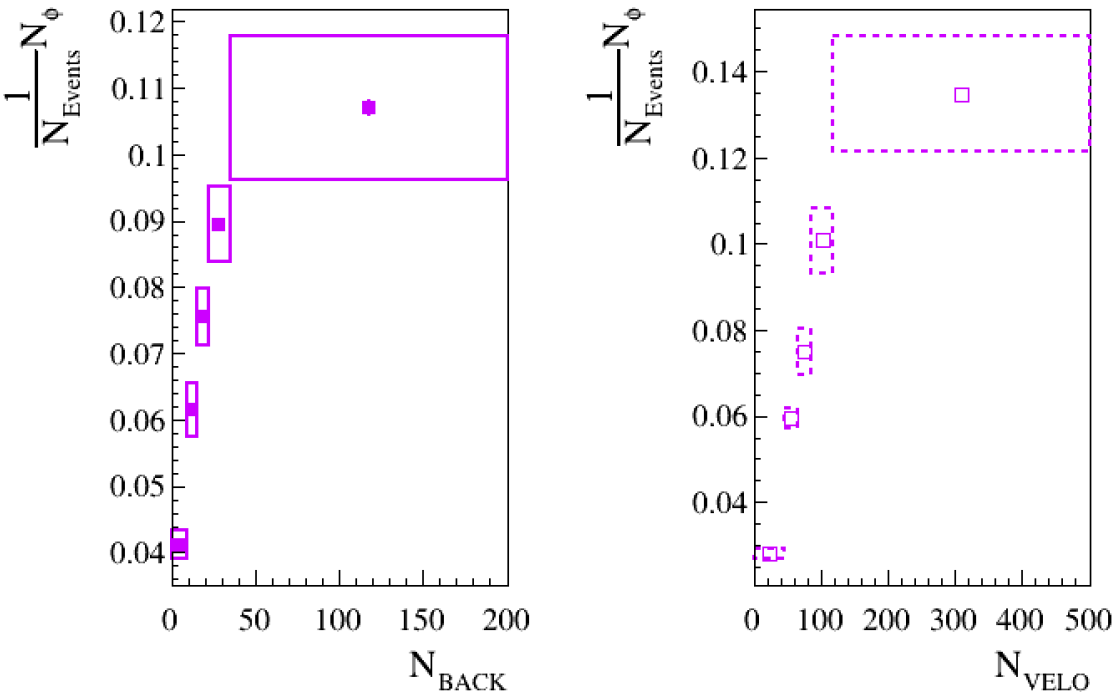


Figure 5.5: Multiplicity-dependent per-event yields of prompt ϕ mesons with respect to (left) backwards tracks and (right) all VELO tracks.

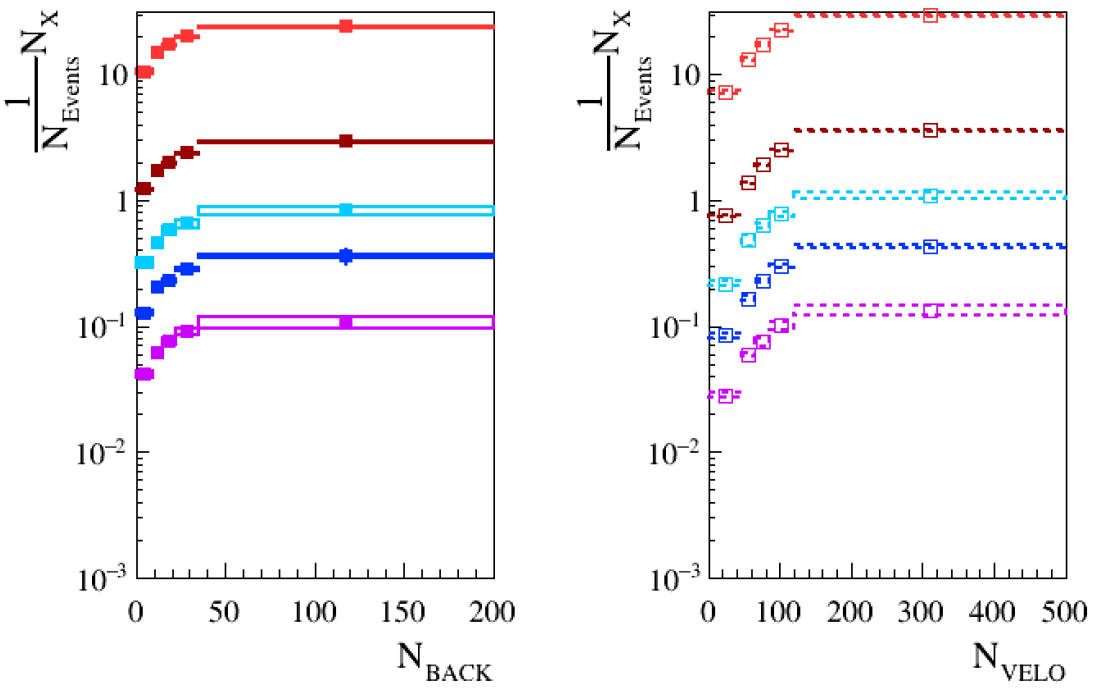


Figure 5.6: Combined multiplicity-dependent per-event yields of prompt hadrons with respect to (left) backwards tracks and (right) all VELO tracks. The listed species are the (Red) charged pion, (Dark Red) p, (Cyan) K^0_S, (Blue) Λ, (Violet) ϕ and the corresponding antiparticles.

It can be seen from figures 5.1,5.2,5.3,5.4,5.5 that hadron yield per event increases with track multiplicity, particularly with respect to the inclusive multiplicity estimator. This, however, is a relatively trivial observation given that an increase in particle production must contribute to an increase in final state charged tracks. This affirms the decision to search for hadronization modification by performing yield ratios from these production rates.

5.1 Search for Strangeness Enhancement in pp at $\sqrt{s}$ = 13 TeV

Recall from chapter 1 that there are two classes of hadronization mechanisms expected to contribute to strangeness enhancement. Lund String-based hadronization modification introduces dynamic interactions between individual color-flux tubes based on the relative flow of color charges, which in turn allows for the emergence of collective behavior among the strings. This collective behavior alters the energy density of the local color field, such that heavier quark pairs have an increased production probability. Coalescence-based hadronization modification utilizes the Statistical Hadronization Model to model the chemical evolution in the interior of a thermalizing QCD medium. Gluon fusion processes allow for strange quark pairs to avoid the chemical potential-dependent suppression that affects the lighter quarks, leading to a relative abundance of strange in the medium prior to hadron clustering. The existence of at least one of these mechanisms in pp collisions can be supported by investigating the production rates of strange hadrons (K^0_S, ϕ, Λ) with respect to a ubiquitous, non-strange hadron (π^+). The ϕ meson is technically an unflavored hadron with a Strangeness quantum number of zero (S = 0), but is included due to being a strange quark-antiquark bound state and thus being sensitive to strange quark production.

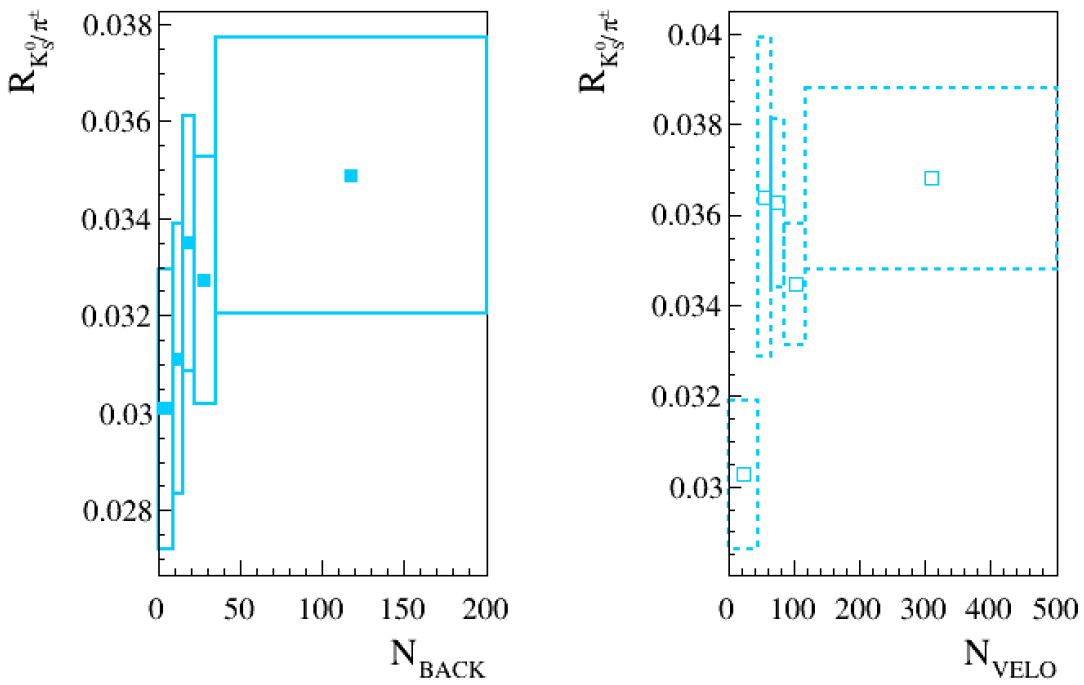


Figure 5.7: Multiplicity-dependent $\frac{K^0_S}{\pi^+ + \pi^-}$ yield ratios with respect to (left) backwards tracks and (right) all VELO tracks.

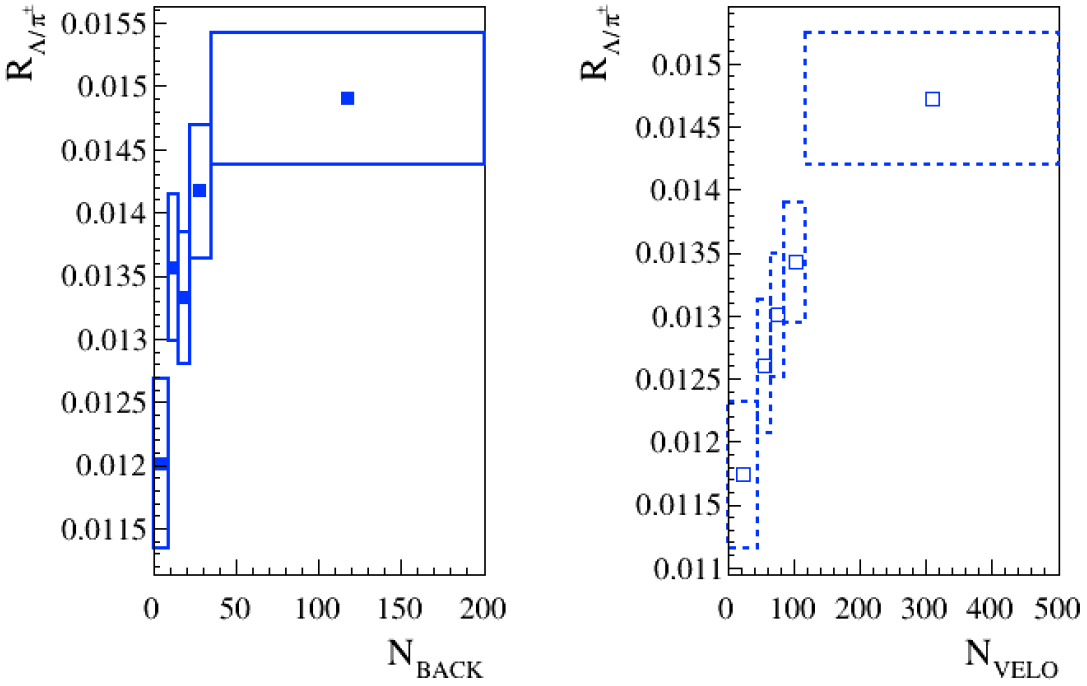


Figure 5.8: Multiplicity-dependent $\frac{\Lambda+\bar{\Lambda}}{\pi^{+}+\pi^{-}}$ yield ratios with respect to (left) backwards tracks and (right) all VELO tracks.

Given that the Λ is a strange baryon, comparisons to the other light-flavor baryon in the analysis (p) are made to confirm that the observed modification is not due exclusively to baryon-enhancement processes. In Figure 5.9 a relative enhancement of strange baryons is observed, confirming the existence of a flavor-dependent contribution to Λ production.

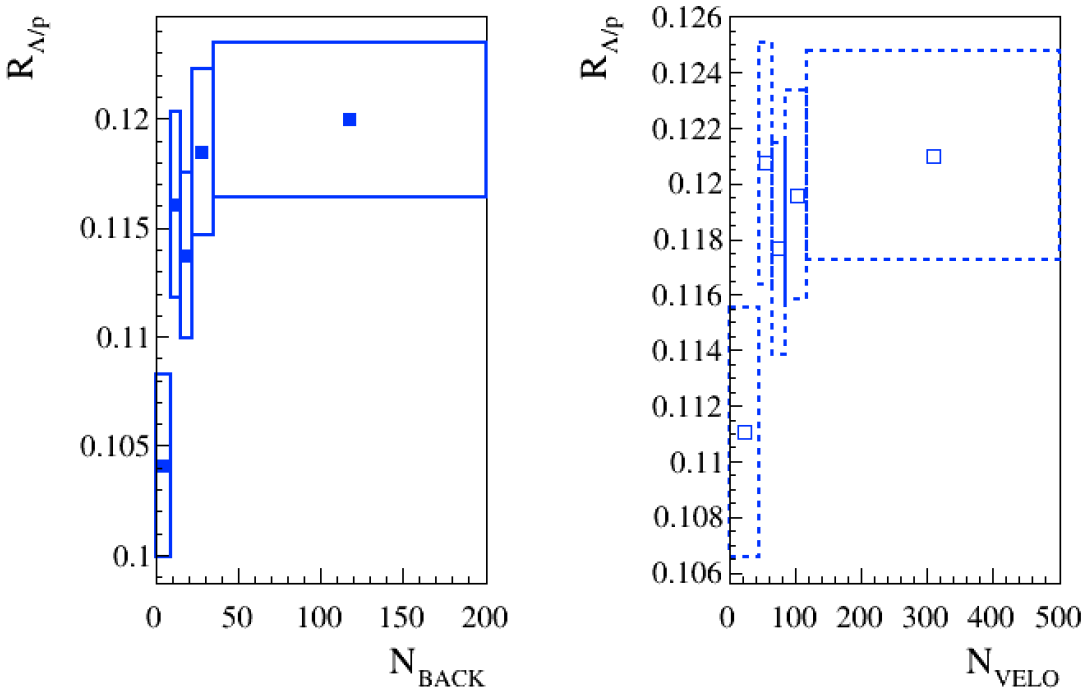


Figure 5.9: Multiplicity-dependent $\frac{\Lambda+\bar{\Lambda}}{p+\bar{p}}$ yield ratios with respect to (left) backwards tracks and (right) all VELO tracks.

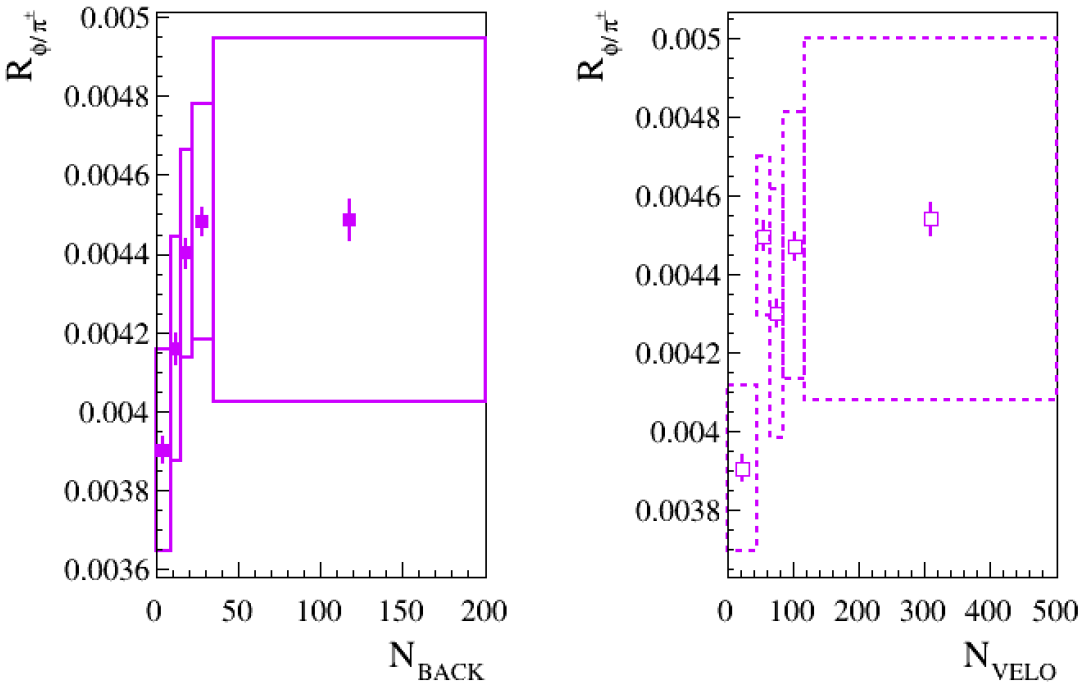


Figure 5.10: Multiplicity-dependent $\frac{\phi}{\pi^+ + \pi^-}$ yield ratios with respect to (left) backwards tracks and (right) all VELO tracks.

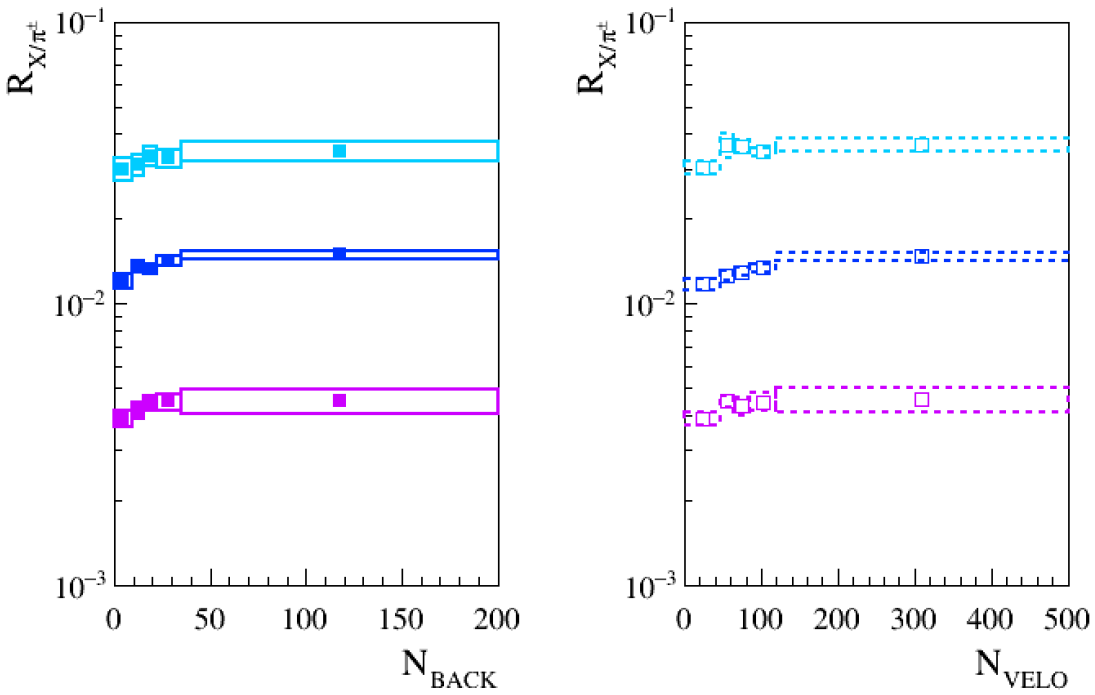


Figure 5.11: Summary of strangeness production ratios to charged pions in pp collisions at $\sqrt{s} = 13$ TeV. The listed species are (Cyan) K^0_S, (Blue) Λ, (Violet) ϕ and the corresponding antiparticles.

Looking at Figures 5.7, 5.8, and 5.10 , it can be seen that non-zero strangeness enhancement is observed in light-flavor hadrons at forward rapidity, affirming previous measurements of QGP-associated hadronization modification signatures in pp collision systems. The choice of multiplicity estimator appears to have minimal effects on the strength of the enhancement. The implication from this feature is that (as it pertains to light flavor hadronization) the hadronization modification mechanism in small systems is not exclusively dependent on local particle density. Similar measurements in heavy-flavor mesons from pp collisions at LHCb displayed a bias towards local event density, since a non-zero enhancement with respect to backwards tracks could not be observed(13). This discrepancy implies that hadronization modification for heavy-flavor particles is more sensitive to local event activity than for light-flavor hadrons.

The production cross-section for heavy quarks (particularly b-quarks) is biased closer to the beam-line due to the asymmetric kinematics in the initial state scatterings that are most likely to produce heavy quarks at LHC energies. This means that the center of mass frame for a signal hadron will likely be boosted for heavy-flavor species (or any daughters of similar momenta) in comparison to lighter hadrons. Coalescence requires the overlap of partonic wavefunctions in phase-space to generate new bound states, which suggests that

heavy-flavor hadronization via coalescence is most probable when the neighboring partons are boosted as well. Referring back to figures 1.13 and 1.14, it can be seen that the strength of the enhancements is maximized at low-p_{T}, where the heavy-quark and neighboring partons are more likely to have significant phase-space overlap. In comparison, light-flavor species will not be biased towards significantly boosted frames with respect to the collision system. This can be seen in the qualitative enhancement discrepancies with respect to backward tracks between heavy and light flavor species. Based on the argument provided, heavy-flavor coalescence is most likely when the heavy quark is in the vicinity of boosted neighbors. When the multiplicity of particles (i.e. tracks) increases in the forward region, the density of partonic phase-space neighbors in the heavy quark boosted frame also increases, therefore biasing enhancement via coalescence towards high local event activity collisions. In light-flavor species, this biasing does not appear to exist due to the more isotropic nature of light quark production (especially when thermal production is considered). The results from this analysis are consistent with coalescence effects, and when combined with the previous small-system results from LHCb imply a coalescence-dependent contribution to the hadronization modification of pp collisions.

5.2 Search for Baryon Enhancement in pp at $\sqrt{s} = 13$ TeV

The two mechanisms expected to play a role in the enhanced generation of the baryons are the generation of color junctions from attractive Lund-string interactions and the coalescence of partons into three-quark states due to the abundance of low-momentum quarks in an equilibrating medium.

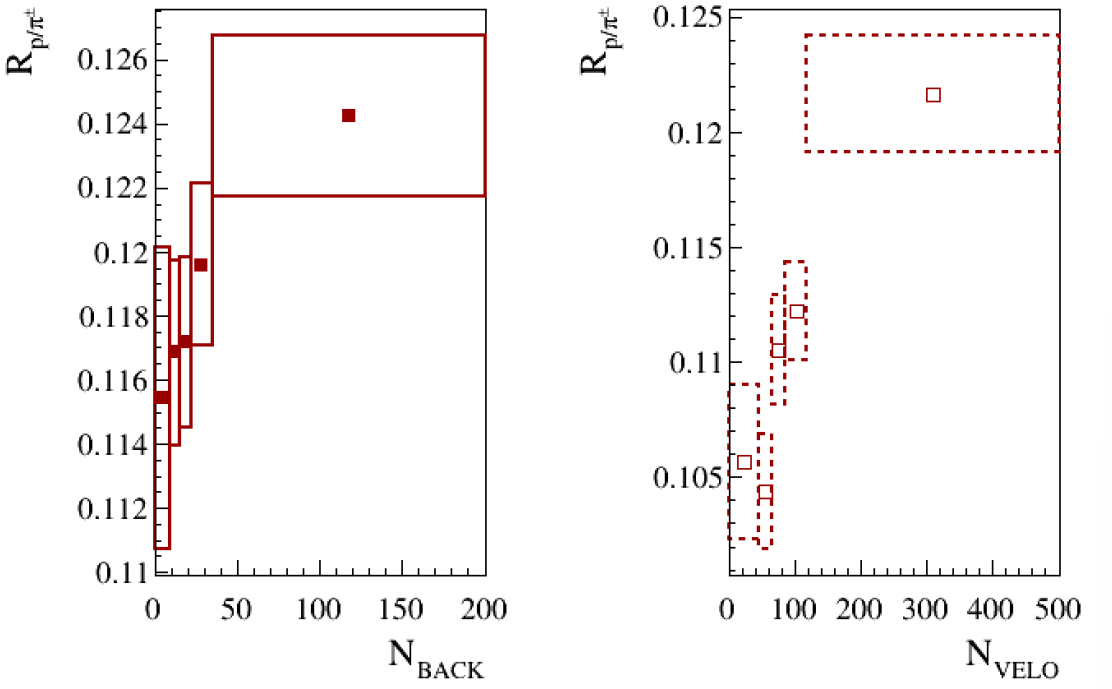


Figure 5.12: Multiplicity-dependent $\frac{p+\bar{p}}{\pi^+ + \pi^-}$ yield ratios with respect to (left) backwards tracks and (right) all VELO tracks.

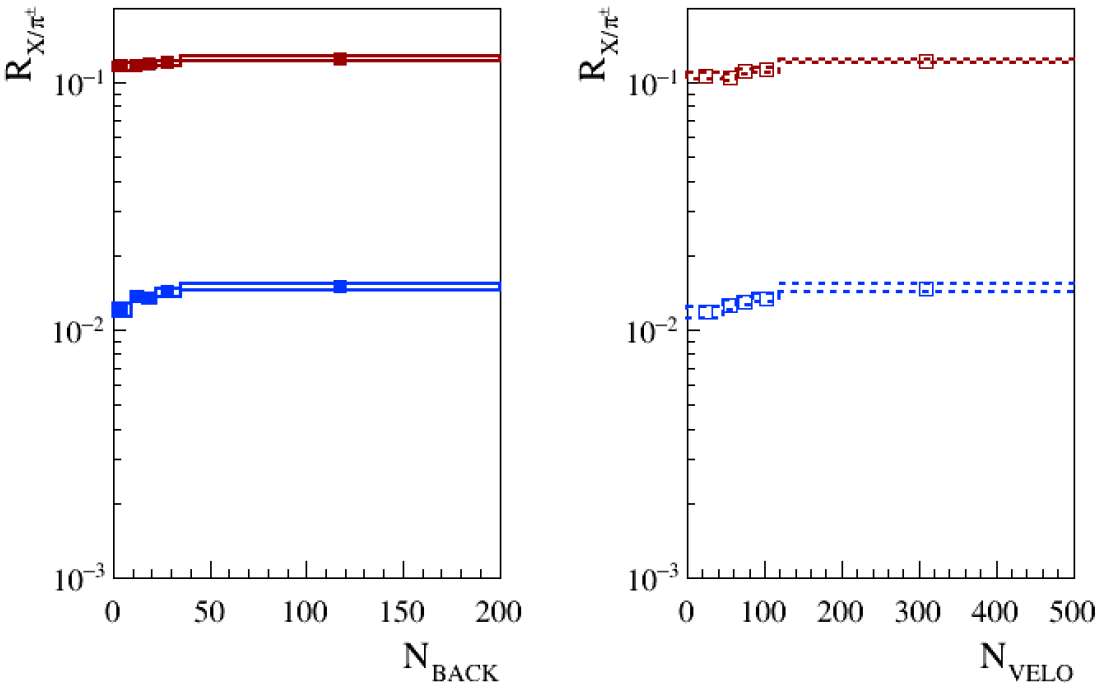


Figure 5.13: Combined multiplicity-dependent baryon-to-meson ratios with respect to (left) backwards tracks and (right) all VELO tracks. The listed species are the (Dark Red) p and (Blue) Λ along with the corresponding antiparticles.

In addition to the observation of strangeness enhancement, baryon enhancement is also measured in light-flavor hadrons in pp collisions at 13 TeV. Similarly to the strangeness enhancement measurements, light-flavor baryon production rates are not greatly impacted by the choice of activity estimator (global vs local) . These results are consistent with the hypothesis that baryon enhancement and strangeness enhancement are generated by the same mechanism in light-flavor species.

In QGP-agnostic Lund-string models (e.g. the model used in the Pythia ANGANTYR Monte-Carlo Event Generator(74; 75)), the color string-densities necessary to see effects from hadronization modifcation are achieved when the majority of the proton collision activity is distributed into distinct angular regions (jets or 'minijets') rather than isotropically. This should generate a local event activity-dependence in events dominated by Lund-string-based hadronization modification with little-to-no QGP contribution. Yet, prior to comparisons with phenomenological models, it cannot be stated definitively whether string junction formation or other Lund-string modifications are excluded as a potential source of the enhancement. Such phenomenological predictions in the kinematic and pseudorapidity range of the LHCb detector are not yet available, due in part to the lack of experimental reference data for light hadrons.

5.3 Discussion

5.3.1 Agreement between Multiplicity Variables

The lack of strong discrepancies between activity estimators are consistent with what can be expected in light-flavor hadron production since the two variables are correlated (backward tracks are inherently a subset of the total VELO tracks) and the majority of charged tracks are left by light hadrons.

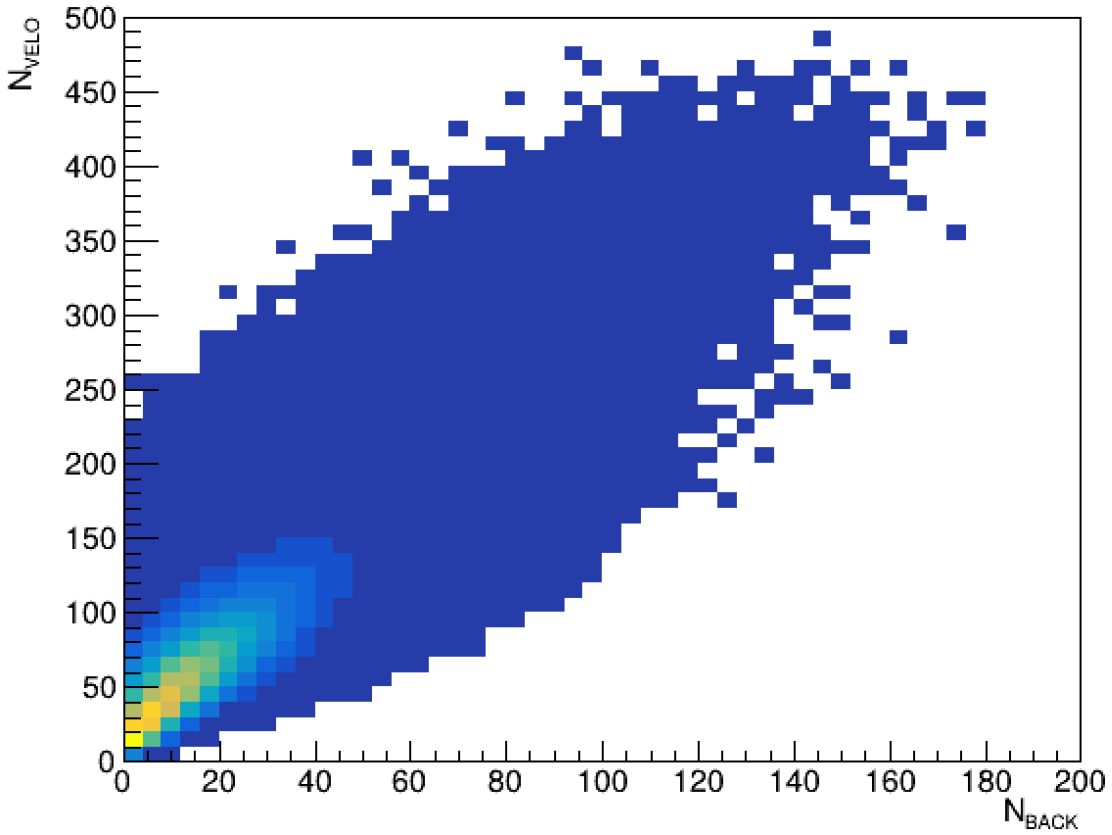


Figure 5.14: Correlation between all VELO tracks and backwards VELO tracks in minimum bias collider events.

Given the correlation, the major distinction between the estimators is their geometric coverage, and sans the boosting effect expected in heavy-flavor hadron production, the hadronization observables should be in strong qualitative agreement.

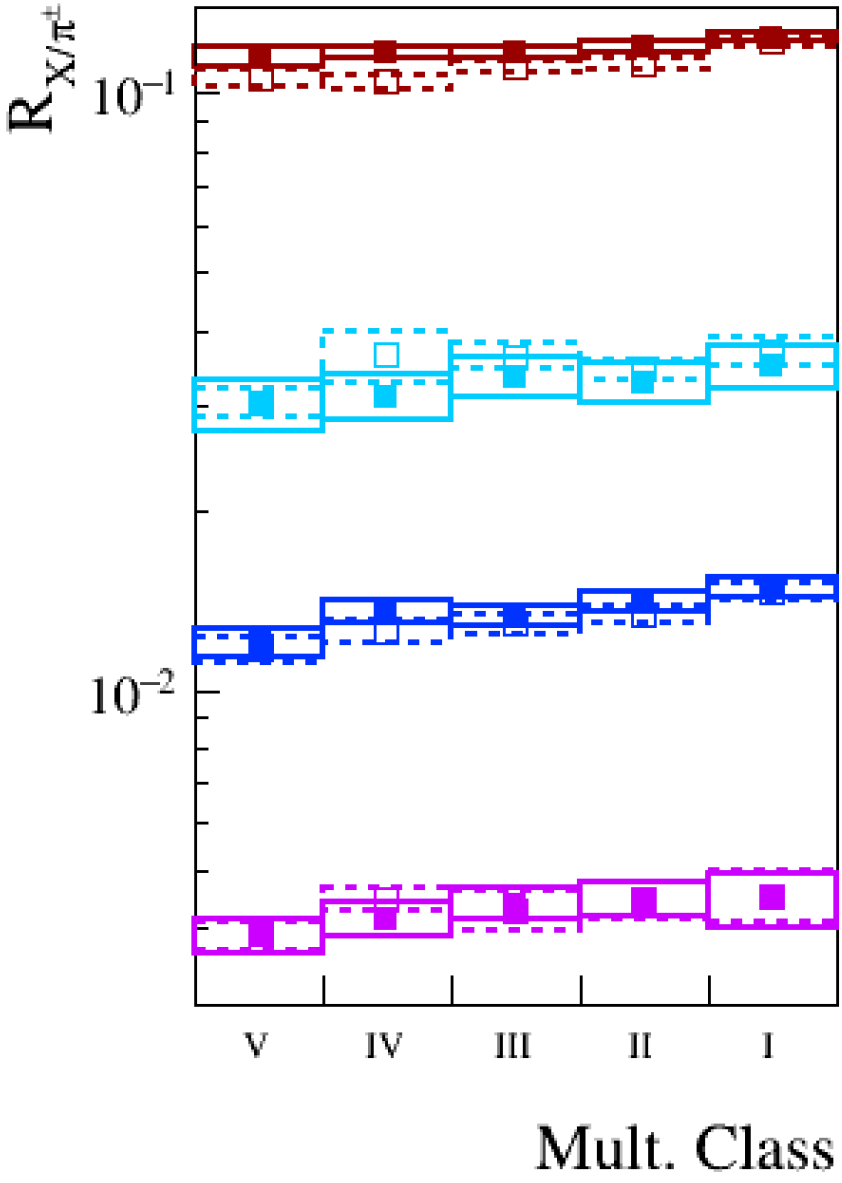


Figure 5.15: Yield ratios to charged pions for (Dark Red) p, (Cyan) K^0_S, (Blue) Λ, (Violet) ϕ binned by multiplicity class. Results with respect to N_{BACK} (solid, filled) and N_{VELO} (open, dashed) are shown.

5.3.2 Experimental Comparisons

ALICE has observed hadronization modification in varying light-flavor species, however, their measurements have been limited by their detector geometries to the central pseudora-

pidity region. ALICE, STAR, and PHENIX have performed a myriad of measurements at mid-rapidity related to strangeness enhancement, baryon enhancement, and other collective phenomena signatures in collisions involving heavy nuclei (pA or AA). The LHCb detector had measured strangeness enhancement in the forward direction and in small systems, but exclusively using heavy flavor mesons (B mesons in pp and D^+ mesons in pPb). The observation of small system strangeness and baryon enhancement in light-flavor hadrons at forward rapidity fills a gap in the experimental landscape thus far, providing data which will be central in generating a universal and consistent framework for the hadronization mechanisms in hadronic collisions.

By comparing these results, information on the nature of the hadronization mechanisms in small systems can be gleaned. Given the difference in track multiplicity estimation by the two experiments, the horizontal axes for all plots are re-framed in terms of the relative multiplicity density to the average ($\langle dN_{\rm ch}/d\eta \rangle$) for each experiment respectively. The yields for charged pions, protons, and Λ baryons from ALICE are reported as having a factor of 1/2 applied to reflect the inclusion of antiparticle candidates in the counting (no such adjustment is made for hadronic species that are their own antiparticle such as K^0_S and ϕ). To make direct comparisons to the LHCb results, these factors are removed in the following figures. The qualitative agreement between LHCb and ALICE verifies that activity-dependent hadronization modifications are present across the rapidity spectrum (at least in what is observable at the LHC).

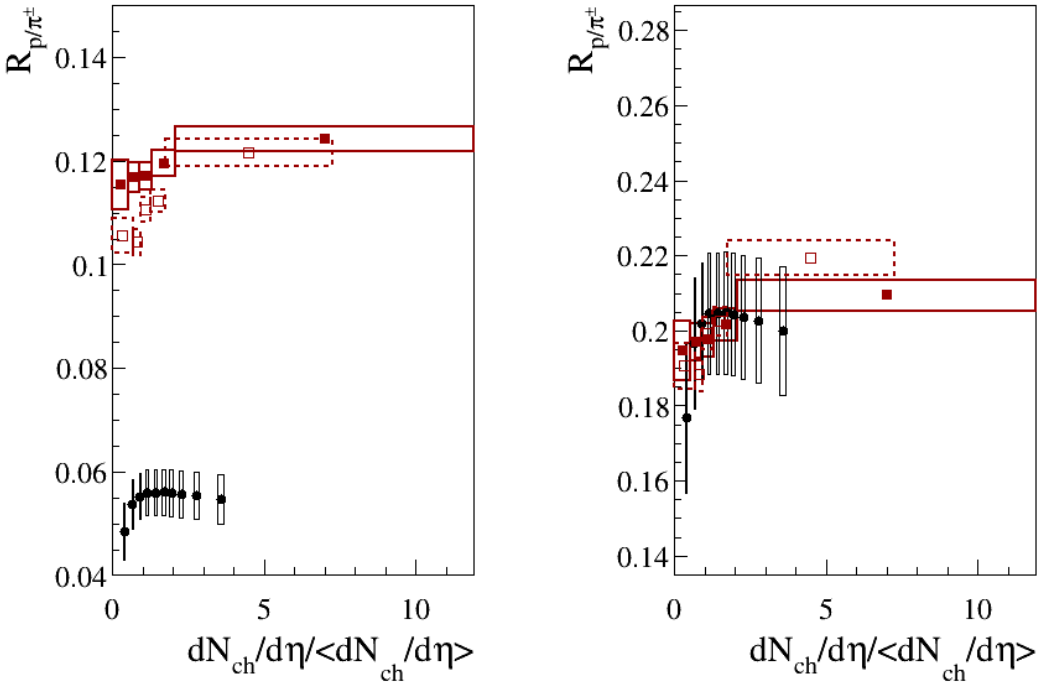


Figure 5.16: Absolute (left) and normalized (right) multiplicity-dependent (Dark Red) $\frac{\mathrm{p}+\bar{\mathrm{p}}}{\pi^+ + \pi^-}$ yield ratios with respect to charged track density. Results with respect to N_{BACK} (solid, filled) and N_{VELO} (open, dashed) are provided along with results from ALICE(12) (Black) in pp collisions at $\sqrt{s} = 13$ TeV.

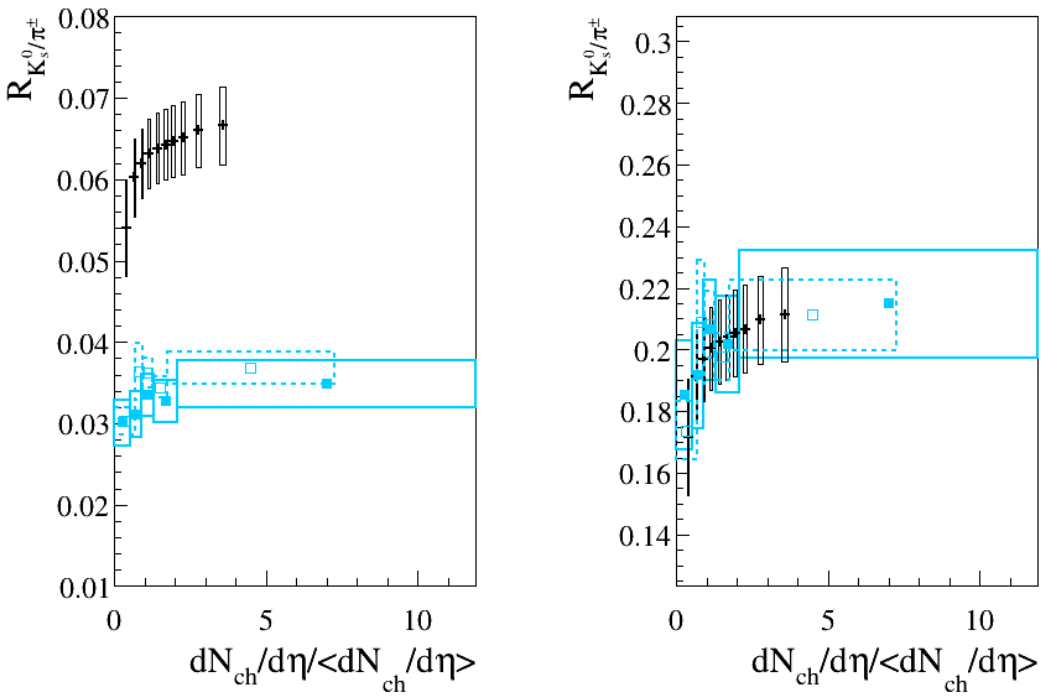


Figure 5.17: Absolute (left) and normalized (right) multiplicity-dependent (Cyan) $\frac{\mathrm{K_S^0}}{\pi^+ + \pi^-}$ yield ratios with respect to charged track density. Results with respect to N_{BACK} (solid, filled) and N_{VELO} (open, dashed) are provided along with results from ALICE(12) (Black) in pp collisions at $\sqrt{s} = 13$ TeV.

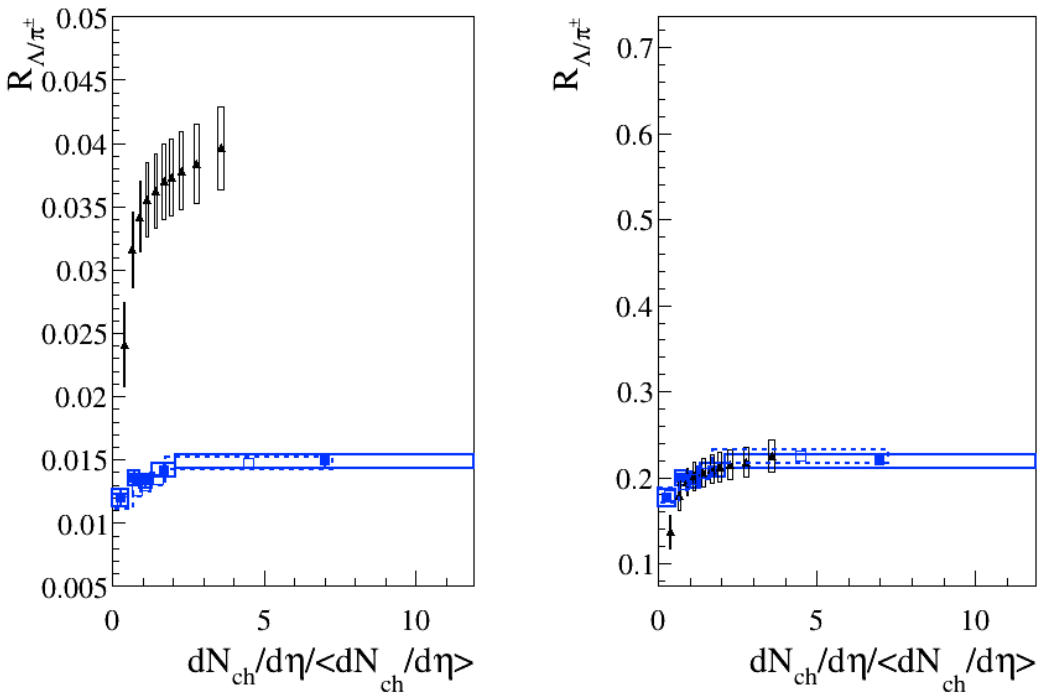


Figure 5.18: Absolute (left) and normalized (right) multiplicity-dependent (Blue) $\frac{\Lambda+\bar{\Lambda}}{\pi^+ + \pi^-}$ yield ratios with respect to charged track density. Results with respect to N_{BACK} (solid, filled) and N_{VELO} (open, dashed) are provided along with results from ALICE(12) (Black) in pp collisions at $\sqrt{s} = 13$ TeV.

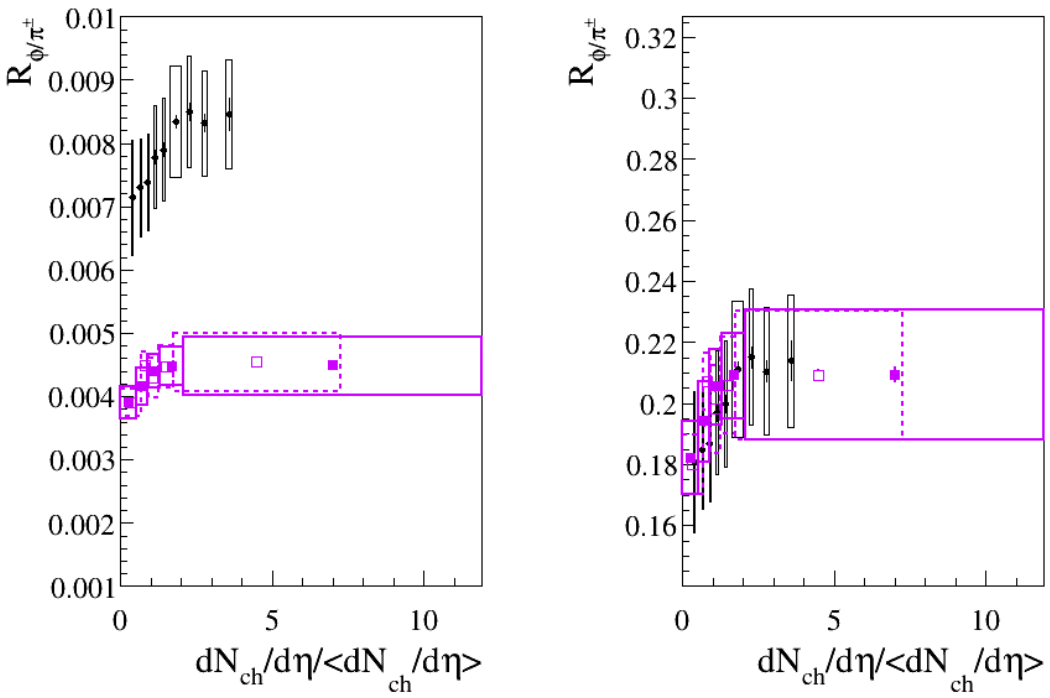


Figure 5.19: Absolute (left) and normalized (right) multiplicity-dependent (Violet) $\frac{\phi}{\pi^+ + \pi^-}$ yield ratios with respect to charged track density. Results with respect to N_{BACK} (solid, filled) and N_{VELO} (open, dashed) are provided along with results from ALICE(15) (Black) in pp collisions at $\sqrt{s} = 7$ TeV.

The slope of $\mathrm{K}^0_{\mathrm{S}}$ enhancements appears to be in strong agreement between experiments when consulting the right plot in Figure 5.17. It should be noted that this is partially due to the large systematic uncertainties on the LHCb $\mathrm{K}^0_{\mathrm{S}}$ yields originating from the fit performance. Future measurements with larger statistics may aid in reducing these uncertainties and utilizing finer binning such that stronger comparative claims can be made. The normalized plots in figures 5.16 and 5.18 show good but weaker agreement between the forward and midrapidity results for protons and Λ baryons respectively. It appears that forward rapidity protons are less consistent with flat or negative slopes at high multiplicity than the results from ALICE, however, given the size of the uncertainties on the midrapidity measurements, positive enhancement across all multiplicity classes would still be consistent with their results. Yet when combined with the observation that the baryon enhancement values for protons at LHCb are systematically higher than at ALICE by approximately a factor of 2 (whereas the strangeness enhancement values at LHCb are lower than ALICE by approximately a factor of 2 across the board), it is possible that strong forward rapidity-bias for baryon-enhancement in protons may exist. A likely candidate for this behavior is a slight

forward boost in protons (not antiprotons) from high-momentum valence quarks from the initial state. Given that antiproton coalescence is dependent on the generation of light-flavor antiquarks, the relevant partons are primarily either sampled from the low-momentum dominated sea-quark distribution of the initial state or thermally (isotropically) produced in the collisions, neither of which would provide a significant boost to higher rapidity. These results and interpretations are in qualitative agreement with previous measurements at the BRAHMS experiment(36; 76; 77; 78), which display relative enhancements for protons with increasing pseudorapidity yet decreasing antiproton ratios to pions and protons as well as low-transverse momentum dominance at forward rapidity (see Figure 5.20).

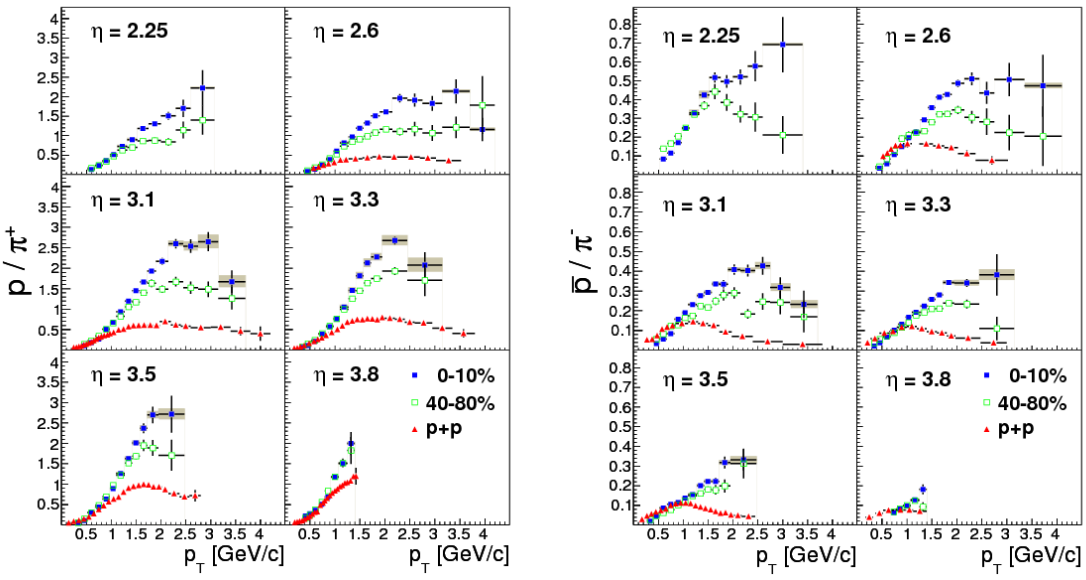


Figure 5.20: Baryon-to-meson ratios measured by BRAHMS at various pseudorapidities(36). Ratios between protons and π^+ (left) as well as antiprotons and π^- (right) are shown in central Au + Au (blue filled square), peripheral Au + Au (green empty square), and multiplicity-integrated pp (red triangle) collisions at $\sqrt{s_{\rm NN}} = 200$ GeV.

Higher precision results from both LHCb and ALICE as well as rapidity-binned and particle-antiparticle separated ratios from LHCb would be useful follow-up measurements to probe these phenomena directly.

In contrast, the Λ enhancement slopes from LHCb and ALICE are in strong agreement aside from a discrepancy in the lowest multiplicity bin. Also, similarly to K^0_S and ϕ but distinct from protons, the numerical values of the Λ enhancement at midrapidity are larger than at forward rapidity. In a coalescence picture this would be a reasonable observation since the Λ production is dependent on thermally generated strange quark-antiquark pairs (like

K^0_S and ϕ), which may dampen any effect from boosted valence quark content. Combining this information with the strong positive slope with respect to multiplicity in the $\frac{\Lambda+\bar{\Lambda}}{p+\bar{p}}$ ratios (see Figure 5.9) provides evidence that the chemical (strangeness-dependent) contribution to the Λ hadronization modification appears to dominate the kinematic (baryon-number dependent) contribution in small systems at forward rapidity. The overall agreement between the normalized ratios from both experiments suggests that the rate of strangeness or baryon enhancement with respect to event activity is not significantly dependent on rapidity and that the production mechanism's dependencies on rapidity and multiplicity are weakly correlated or uncorrelated.

5.3.3 Phenomenological Considerations

The current phenomenological landscape is dominated by theoretical predictions for hadronization modification signatures at midrapidity, largely due to the dearth of light-flavor experimental reference data at forward rapidity. The light-flavor results reported in this thesis along with the recent multiplicity-dependent heavy-flavor measurements from LHCb should instigate more theoretical focus on the forward rapidity region, particularly since it may prove instrumental in discerning the contributions of specific models. In particular, modified Lund-string models appear to display geometric dependencies for the effective string constant as seen in figure. 5.21.

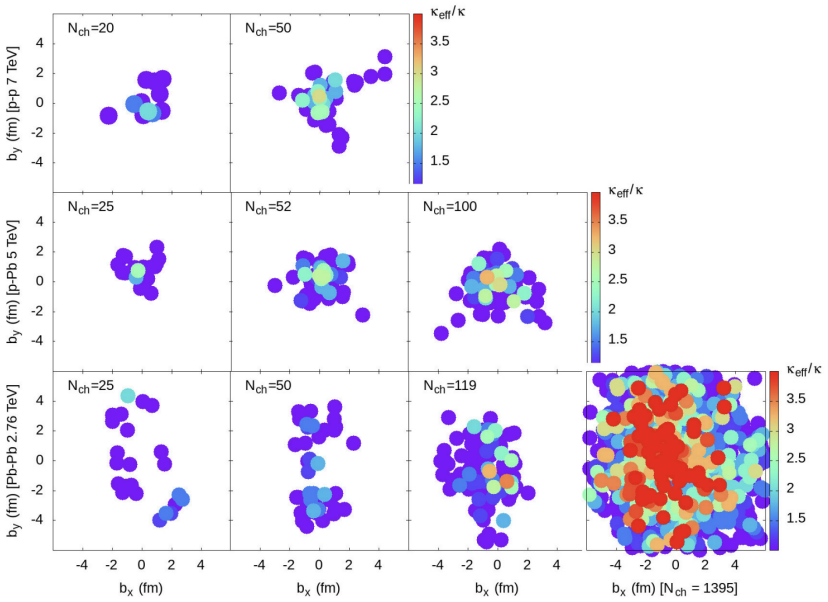


Figure 5.21: Simulations of string fragmentations in Pythia for pp (top), pPb (middle), and PbPb (bottom) collisions. The charged track multiplicity increases to the right, and the value of the effective string constant relative to the nominal string constant is represented by the colormap(37).

Such models also predict small-system hadronization modifications to arise within (mini-)jets and events associated with high-p_{T} hadron production. Follow up measurements which include p_{T}-dependent ratios as well as ratios measured in jet-associated events would provide constraints for Lund-string densities and string constants at forward rapidity.

5.3.4 Evidence for Medium Formation

The motivation of this thesis is to provide experimental data for probing hadronization mechanisms, however, due to the historical role of these observables in searches for QGP production, it must be noted that these results will also be useful for understanding QCD medium transitions and the QCD phase diagram. Unambiguous measurements of chemical (strangeness enhancement) and kinematic (baryon enhancement) signatures for hadronization modification have been reported here for pp collisions at forward pseudorapidity. These results, in combination with previous small collision system measurements at midrapidity and of heavy-flavor species, are in strong qualitative agreement with the existence of hadronization mechanisms associated with QGP formation. What remains to be seen is whether these signatures could possibly be generated without the deconfinement phase transition occurring.

5.3.5 Prospective measurements

Some remaining measurements to perform at the LHCb experiment that would further complete the landscape are: complete the small system strangeness enhancement studies with heavy-flavor mesons (beauty mesons in pPb and charm mesons in pp); measure multiplicity-dependent baryon enhancement in heavy-flavor mesons from pp collisions as well as in all flavors for pA; study strangeness enhancement in higher-mass light-flavor hadrons and excited state resonances (e.g. K^* (892)).

Additionally, revisiting previously measured species and collision systems with higher statistics may provide additional insights. Specifically, higher precision and measurements simultaneously binned in multiplicity and rapidity would serve to discern whether the activity-dependence and rapidity-dependence of the production mechanisms are weakly correlated or completely uncorrelated. Addressing the unique rapidity-dependence of the proton results can be done with charge separated ratios from LHCb to isolate enhancement in particles and antiparticles respectively. A stronger rapidity-dependent enhancement in an antiproton-free sample would be consistent with the coalescence of boosted valence quarks from the initial state. Higher precision comparisons between different multiplicity estimators may reveal stronger enhancement with respect to local event activity (as seen in the heavy-flavor results) depending on the strength of this kinematic biasing.

In addition to measurements at the low edge of the event activity range, additional studies at intermediate multiplicities (collisions involving one or more low mass nuclei) should be performed to verify the smooth transition of hadronization modification from small to large collision systems. Should there be any discontinuities or discrepancies in hadronization observables between small and large collision systems that have gone unnoticed, it is in this regime that such incongruities would be seen. Oxygen nuclei are included in the Run III schedule and in conjunction with the fixed-target module installed in the LHCb detector, measurements populating the intermediate multiplicity regime should be feasible for a variety of hadronic species.

CHAPTER 6

Summary

The investigation of the hadronization processes present in small collision systems remains an active area of research in the modern day due to the absence of a universally cohesive description of how the simplest hadronic collision system behaves at the limits of its event activity. For years, this region of QCD remained under-explored due to assumptions regarding the universality of hadronization mechanisms and the possibility for nuclear phase transitions to exist in very small volumes. Following recent measurements from a variety of experiments, hadronization modification is a generally accepted phenomenon to exist in small collision systems, challenging the field to reckon with its understanding of known hadron production mechanisms and the relevant criteria needed to generate them. To build confidence in the collective understanding of hadronization mechanisms present in LHC collisions, the vast imbalance in the number of measurements of modified hadronization signatures between heavy-ion collisions and small collision systems needs to be addressed with further measurements in pp and pA collisions. Particularly, new measurements with the ability to probe specific geometric or kinematic characteristics of hadronic collisions will generate a more robust landscape of experimental data as well as more specific constraints for prospective models to adhere to.

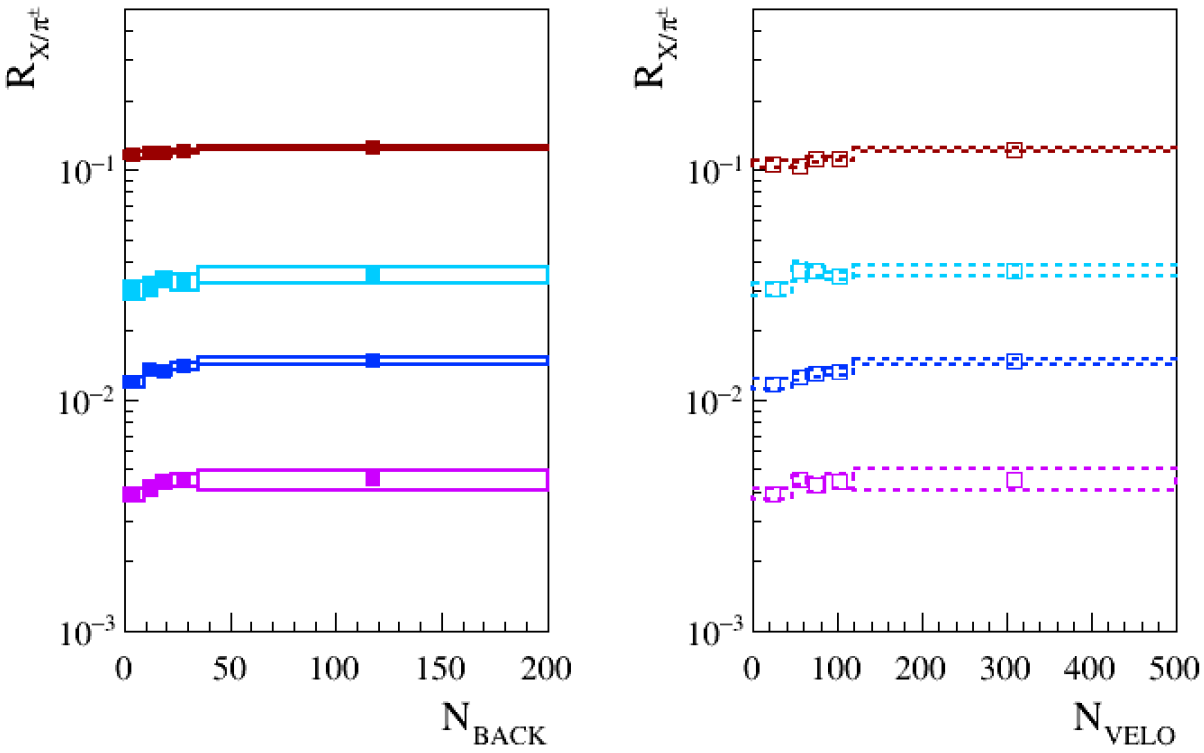


Figure 6.1: Summary of strangeness and baryon enhancement results in pp collisions at $\sqrt{s}$ = 13 TeV from Run II LHCb data. Yield ratios with respect to charged pions are displayed with respect to (left) backwards tracks and (right) all VELO tracks. The listed species are (Dark Red) p, (Cyan) K^0_S, (Blue) Λ, (Violet) ϕ and the corresponding antiparticles.

In this thesis, contributions to this growing effort are made in the form of multiplicity-dependent enhancement studies in pp collisions at the LHCb experiment utilizing the recorded minimum bias data set from Run II of the LHC. Due to the unique forward rapidity coverage of the LHCb detector among the large LHC experiments, a suite of measurements for strangeness and baryon ratios to charged pions was conducted at forward rapidity in small collision systems at the LHC for the first time. It was observed that for light-flavored hadrons (i.e. no beauty or charm quark content) at forward rapidity, strangeness and baryon enhancement were present in pp collisions at 13 TeV. Comparisons of the enhancement slopes to similar light-flavor measurements at midrapidity appear to display a similar event-activity dependence. Measurements at forward rapidity exist systematically below the midrapidity results with the exception of proton enhancement. From this enhancement in forward rapidity it is suggested that high-momentum partons sampled from the valence region of the initial state may contribute significantly to baryon enhancement for protons. Simultaneously, the opposite rapidity-dependence for Λ enhancement is consistent with chemical rather than kinematic effects dominating its production mechanism. Strangeness enhancement was also

recorded in the ϕ meson, which confirms that the strange quark content, not the Strangeness quantum number, is the relevant degree of freedom to consider for multiplicity-dependent hadronization modification. Additionally, no strong preference in the hadronization mechanism for local event activity was measurable, which is consistent with the qualitative picture of a SHM + coalescence-dominant hadronization process. When considering the light masses of the hadronic species studied, it seems reasonable that the observed enhancements would not show significantly stronger slopes for local or isotropic event activity and appear to be in agreement with other experimental data. Similar measurements need to be performed with explicit momentum-binning for light-flavor species to confirm the correlation between observed local activity-dependence and signal hadron kinematics. Additionally, follow-up measurements featuring higher mass light-flavor hadrons with strange quark content (e.g. Ξ, Ω) should be performed to determine if local event activity biasing can be observed in the absence of heavy-quark production. This year sees the first run of Oxygen nuclei in the LHC. Among several other physics goals, one of the aims is to study the behavior of hadronic collision systems at intermediate temperatures and activity levels. This in conjunction with the existence of an upgraded fixed-target system in the LHCb detector, which is capable of storing a wide array of gas targets, emphasizes that follow-up measurements in a variety of collision systems are on the horizon. In the near future, studies similar to the analyses for this thesis will be conducted across a range of event activity levels to pin down the precise microscopic nature of the hadronization mechanisms extant in hadron collisions, particularly in small collision systems.

APPENDIX A

Summary of Yields

Table of Prompt Particle Yields with respect to N_{BACK}			
Multiplicity Class	π^+	p	ϕ
V	$10.84 \pm 0.001 \pm 0.432 \times 10^7$	$12.51 \pm 0.002 \pm 0.107 \times 10^6$	$4.230 \pm 0.039 \pm 0.220 \times 10^5$
IV	$9.485 \pm 0.001 \pm 0.224 \times 10^7$	$11.08 \pm 0.002 \pm 0.090 \times 10^6$	$3.944 \pm 0.038 \pm 0.253 \times 10^5$
III	$10.52 \pm 0.001 \pm 0.229 \times 10^7$	$12.33 \pm 0.002 \pm 0.079 \times 10^6$	$4.630 \pm 0.042 \pm 0.260 \times 10^5$
II	$13.45 \pm 0.001 \pm 0.274 \times 10^7$	$16.09 \pm 0.002 \pm 0.094 \times 10^6$	$6.026 \pm 0.049 \pm 0.383 \times 10^5$
I	$7.838 \pm 0.001 \pm 0.152 \times 10^7$	$9.738 \pm 0.001 \pm 0.053 \times 10^6$	$3.516 \pm 0.042 \pm 0.354 \times 10^5$
Multiplicity Class	K^0_S	Λ	
V	$3.261 \pm 0.007 \pm 0.284 \times 10^6$	$1.302 \pm 0.004 \pm 0.051 \times 10^6$	
IV	$2.951 \pm 0.006 \pm 0.253 \times 10^6$	$1.286 \pm 0.004 \pm 0.046 \times 10^6$	
III	$3.524 \pm 0.006 \pm 0.265 \times 10^6$	$1.402 \pm 0.004 \pm 0.046 \times 10^6$	
II	$4.402 \pm 0.005 \pm 0.328 \times 10^6$	$1.906 \pm 0.004 \pm 0.060 \times 10^6$	
I	$2.734 \pm 0.004 \pm 0.217 \times 10^6$	$1.168 \pm 0.003 \pm 0.034 \times 10^6$	

Table A.1: Summary of corrected yields for signal species with respect to multiplicity (relevant antiparticles are included). For each entry, the first error is from the statistical uncertainty and the second error is from the systematic uncertainty.

Table of Prompt Particle Yields with respect to N_{VELO}			
Multiplicity Class	π^+	p	ϕ
V	$7.053 \pm 0.001 \pm 0.215 \times 10^7$	$7.454 \pm 0.001 \pm 0.068 \times 10^6$	$2.755 \pm 0.025 \pm 0.122 \times 10^5$
IV	$8.889 \pm 0.001 \pm 0.205 \times 10^7$	$9.280 \pm 0.001 \pm 0.063 \times 10^6$	$3.998 \pm 0.036 \pm 0.155 \times 10^5$
III	$11.46 \pm 0.001 \pm 0.238 \times 10^7$	$12.66 \pm 0.002 \pm 0.077 \times 10^6$	$4.927 \pm 0.043 \pm 0.347 \times 10^5$
II	$14.39 \pm 0.001 \pm 0.260 \times 10^7$	$16.15 \pm 0.004 \pm 0.096 \times 10^6$	$6.434 \pm 0.053 \pm 0.474 \times 10^5$
I	$9.923 \pm .0004 \pm 0.192 \times 10^7$	$12.07 \pm 0.002 \pm 0.093 \times 10^6$	$4.505 \pm 0.044 \pm 0.447 \times 10^5$
Multiplicity Class	K_S^0	Λ	
V	$2.134 \pm 0.008 \pm 0.097 \times 10^6$	$0.828 \pm 0.004 \pm 0.033 \times 10^6$	
IV	$3.236 \pm 0.007 \pm 0.304 \times 10^6$	$1.120 \pm 0.004 \pm 0.040 \times 10^6$	
III	$4.156 \pm 0.007 \pm 0.195 \times 10^6$	$1.490 \pm 0.004 \pm 0.047 \times 10^6$	
II	$4.960 \pm 0.007 \pm 0.168 \times 10^6$	$1.932 \pm 0.004 \pm 0.059 \times 10^6$	
I	$3.652 \pm 0.005 \pm 0.186 \times 10^6$	$1.461 \pm 0.003 \pm 0.044 \times 10^6$	

Table A.2: Summary of corrected yields for signal species with respect to multiplicity (relevant antiparticles are included). For each entry, the first error is from the statistical uncertainty and the second error is from the systematic uncertainty.

APPENDIX B

Summary of Yields per Event

Table of Prompt Particle Yields per Event with respect to N_{BACK}			
Multiplicity Class	π^+	p	ϕ
V	$10.59 \pm 0.003 \pm 0.420$	$1.219 \pm .0004 \pm 0.010$	$4.120 \pm 0.038 \pm 0.214 \times 10^{-2}$
IV	$14.79 \pm 0.006 \pm 0.349$	$1.729 \pm 0.001 \pm 0.012$	$6.151 \pm 0.060 \pm 0.394 \times 10^{-2}$
III	$17.17 \pm 0.007 \pm 0.373$	$2.011 \pm 0.001 \pm 0.013$	$7.554 \pm 0.068 \pm 0.424 \times 10^{-2}$
II	$19.96 \pm 0.008 \pm 0.407$	$2.387 \pm 0.001 \pm 0.014$	$8.944 \pm 0.073 \pm 0.568 \times 10^{-2}$
I	$23.86 \pm 0.013 \pm 0.461$	$2.964 \pm 0.002 \pm 0.016$	$10.70 \pm 0.128 \pm 1.077 \times 10^{-2}$
Multiplicity Class	K^0_S	Λ	
V	$3.176 \pm 0.007 \pm 0.277 \times 10^{-1}$	$1.268 \pm 0.004 \pm 0.050 \times 10^{-1}$	
IV	$4.602 \pm 0.010 \pm 0.395 \times 10^{-1}$	$2.006 \pm 0.006 \pm 0.072 \times 10^{-1}$	
III	$5.750 \pm 0.010 \pm 0.433 \times 10^{-1}$	$2.287 \pm 0.007 \pm 0.075 \times 10^{-1}$	
II	$6.533 \pm 0.008 \pm 0.487 \times 10^{-1}$	$2.828 \pm 0.007 \pm 0.089 \times 10^{-1}$	
I	$8.321 \pm 0.012 \pm 0.659 \times 10^{-1}$	$3.555 \pm 0.009 \pm 0.103 \times 10^{-1}$	

Table B.1: Summary of corrected yields per event for signal species with respect to multiplicity (relevant antiparticles are included). For each entry, the first error is from the statistical uncertainty and the second error is from the systematic uncertainty.

Table of Prompt Particle Yields per Event with respect to N_{VELO}			
Multiplicity Class	π^+	p	ϕ
V	$7.190 \pm 0.002 \pm 0.219$	$0.760 \pm .0003 \pm 0.007$	$2.808 \pm 0.025 \pm 0.125 \times 10^{-2}$
IV	$13.21 \pm 0.005 \pm 0.305$	$1.380 \pm 0.001 \pm 0.009$	$5.944 \pm 0.054 \pm 0.230 \times 10^{-2}$
III	$17.44 \pm 0.007 \pm 0.362$	$1.928 \pm 0.001 \pm 0.012$	$7.502 \pm 0.066 \pm 0.528 \times 10^{-2}$
II	$22.53 \pm 0.009 \pm 0.408$	$2.529 \pm 0.001 \pm 0.015$	$10.08 \pm 0.083 \pm 0.743 \times 10^{-2}$
I	$29.69 \pm 0.016 \pm 0.573$	$3.612 \pm 0.002 \pm 0.028$	$13.48 \pm 0.133 \pm 1.337 \times 10^{-2}$
Multiplicity Class	K^0_S	Λ	
V	$2.176 \pm 0.008 \pm 0.099 \times 10^{-1}$	$0.844 \pm 0.004 \pm 0.033 \times 10^{-1}$	
IV	$4.812 \pm 0.010 \pm 0.452 \times 10^{-1}$	$1.666 \pm 0.005 \pm 0.059 \times 10^{-1}$	
III	$6.327 \pm 0.011 \pm 0.297 \times 10^{-1}$	$2.268 \pm 0.006 \pm 0.072 \times 10^{-1}$	
II	$7.768 \pm 0.012 \pm 0.264 \times 10^{-1}$	$3.025 \pm 0.006 \pm 0.093 \times 10^{-1}$	
I	$10.928 \pm 0.015 \pm 0.557 \times 10^{-1}$	$4.371 \pm 0.008 \pm 0.130 \times 10^{-1}$	

Table B.2: Summary of corrected yields per event for signal species with respect to multiplicity (relevant antiparticles are included). For each entry, the first error is from the statistical uncertainty and the second error is from the systematic uncertainty.

APPENDIX C

Summary of Ratios

Table of Prompt Particle Ratios to $\pi^+ + \pi^-$ Yields with respect to N_{BACK}		
Multiplicity Class	p	ϕ
V	$1.154 \pm .0002 \pm 0.047 \times 10^{-1}$	$3.902 \pm 0.036 \pm 0.256 \times 10^{-3}$
IV	$1.169 \pm .0002 \pm 0.029 \times 10^{-1}$	$4.158 \pm 0.041 \pm 0.284 \times 10^{-3}$
III	$1.172 \pm .0002 \pm 0.027 \times 10^{-1}$	$4.401 \pm 0.039 \pm 0.265 \times 10^{-3}$
II	$1.196 \pm .0002 \pm 0.025 \times 10^{-1}$	$4.480 \pm 0.036 \pm 0.299 \times 10^{-3}$
I	$1.252 \pm .0002 \pm 0.025 \times 10^{-1}$	$4.486 \pm 0.054 \pm 0.460 \times 10^{-3}$
Multiplicity Class	K^0_S	Λ
V	$3.008 \pm 0.007 \pm 0.288 \times 10^{-2}$	$1.201 \pm 0.003 \pm 0.067 \times 10^{-2}$
IV	$3.111 \pm 0.006 \pm 0.277 \times 10^{-2}$	$1.356 \pm 0.003 \pm 0.058 \times 10^{-2}$
III	$3.350 \pm 0.006 \pm 0.263 \times 10^{-2}$	$1.332 \pm 0.003 \pm 0.052 \times 10^{-2}$
II	$3.273 \pm 0.004 \pm 0.253 \times 10^{-2}$	$1.417 \pm 0.003 \pm 0.053 \times 10^{-2}$
I	$3.488 \pm 0.005 \pm 0.284 \times 10^{-2}$	$1.490 \pm 0.003 \pm 0.052 \times 10^{-2}$

Table C.1: Summary of corrected yield ratios to charged pions for signal species with respect to multiplicity (relevant antiparticles are included). For each entry, the first error is from the statistical uncertainty and the second error is from the systematic uncertainty.

Table of Prompt Particle Ratios to $\pi^+ + \pi^-$ Yields with respect to N_{VELO}		
Multiplicity Class	p	ϕ
V	$1.057 \pm .0002 \pm 0.034 \times 10^{-1}$	$3.906 \pm 0.035 \pm 0.210 \times 10^{-3}$
IV	$1.044 \pm .0001 \pm 0.025 \times 10^{-1}$	$4.497 \pm 0.040 \pm 0.203 \times 10^{-3}$
III	$1.105 \pm .0002 \pm 0.024 \times 10^{-1}$	$4.301 \pm 0.038 \pm 0.316 \times 10^{-3}$
II	$1.122 \pm .0003 \pm 0.021 \times 10^{-1}$	$4.472 \pm 0.037 \pm 0.339 \times 10^{-3}$
I	$1.217 \pm .0002 \pm 0.025 \times 10^{-1}$	$4.540 \pm 0.045 \pm 0.459 \times 10^{-3}$
Multiplicity Class	K^0_S	Λ
V	$3.026 \pm 0.011 \pm 0.165 \times 10^{-2}$	$1.174 \pm 0.006 \pm 0.058 \times 10^{-2}$
IV	$3.640 \pm 0.008 \pm 0.352 \times 10^{-2}$	$1.260 \pm 0.004 \pm 0.053 \times 10^{-2}$
III	$3.628 \pm 0.006 \pm 0.186 \times 10^{-2}$	$1.301 \pm 0.003 \pm 0.049 \times 10^{-2}$
II	$3.447 \pm 0.005 \pm 0.133 \times 10^{-2}$	$1.342 \pm 0.003 \pm 0.048 \times 10^{-2}$
I	$3.680 \pm 0.005 \pm 0.201 \times 10^{-2}$	$1.472 \pm 0.003 \pm 0.052 \times 10^{-2}$

Table C.2: Summary of corrected yield ratios to charged pions for signal species with respect to multiplicity (relevant antiparticles are included). For each entry, the first error is from the statistical uncertainty and the second error is from the systematic uncertainty.

APPENDIX D

Summary of Efficiencies

D.1 Particle Identification Efficiencies

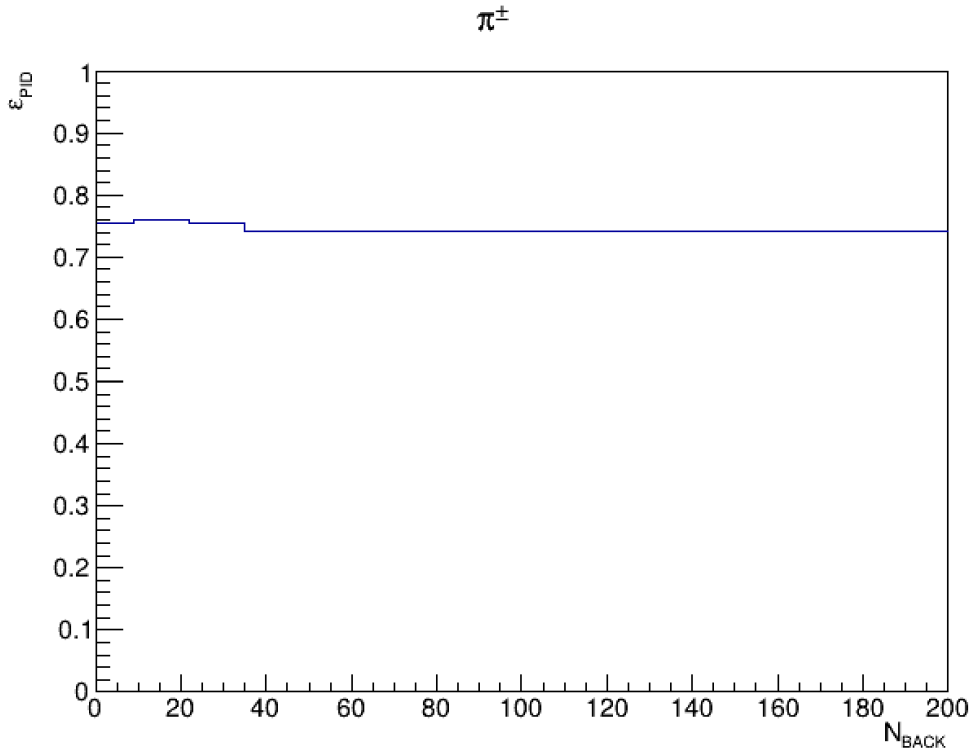


Figure D.1: Rebinned particle identification efficiencies for pion candidates matching the selection criteria written out in section 3.1.

ε_{PID}				
π^+				
Multiplicity Class	MagDown		MagUp	
	N_{BACK}	N_{VELO}	N_{BACK}	N_{VELO}
V	0.754	0.753	0.756	0.755
IV	0.760	0.767	0.764	0.774
III	0.760	0.764	0.764	0.769
II	0.754	0.750	0.759	0.753
I	0.740	0.715	0.745	0.714

Table D.1: Summary of particle identification efficiencies for charged pions.

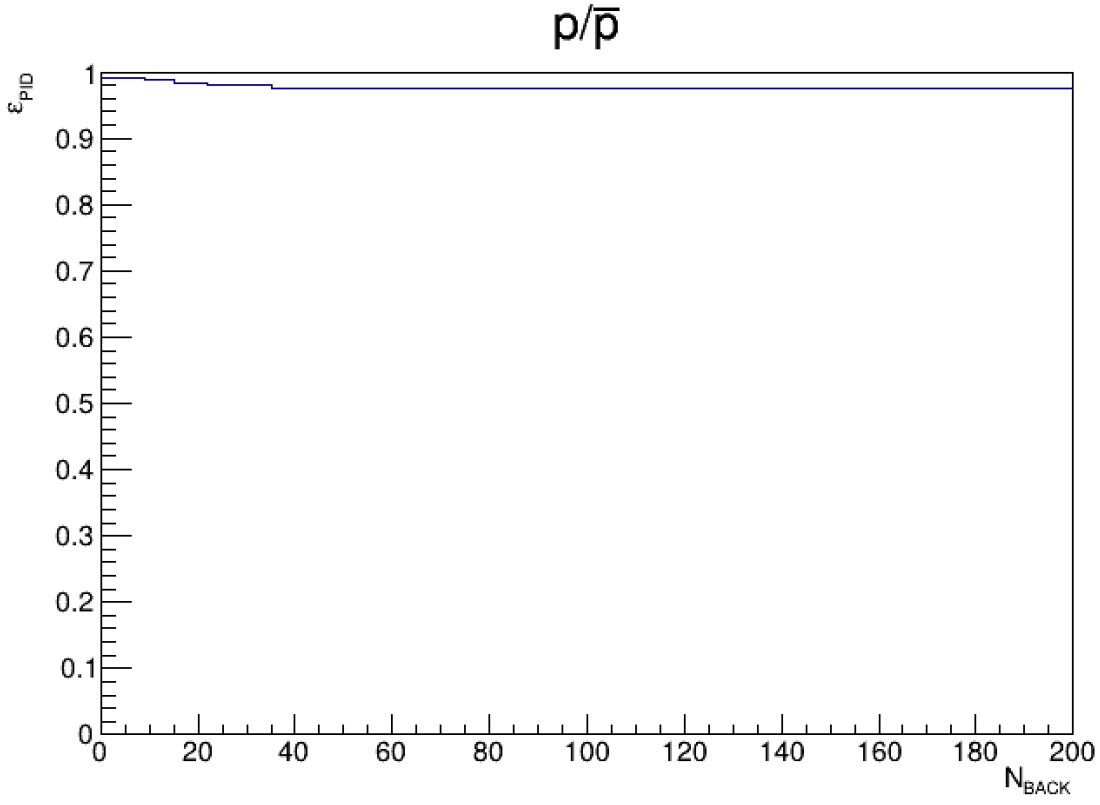


Figure D.2: Rebinned particle identification efficiencies for proton candidates matching the selection criteria written out in section 3.1.

ε_{PID}				
p				
Multiplicity Class	MagDown		MagUp	
	N_{BACK}	N_{VELO}	N_{BACK}	N_{VELO}
V	0.991	0.993	0.995	0.998
IV	0.988	0.987	0.994	0.997
III	0.984	0.982	0.990	0.987
II	0.980	0.976	0.984	0.976
I	0.975	0.967	0.976	0.964

Table D.2: Summary of particle identification efficiencies for protons.

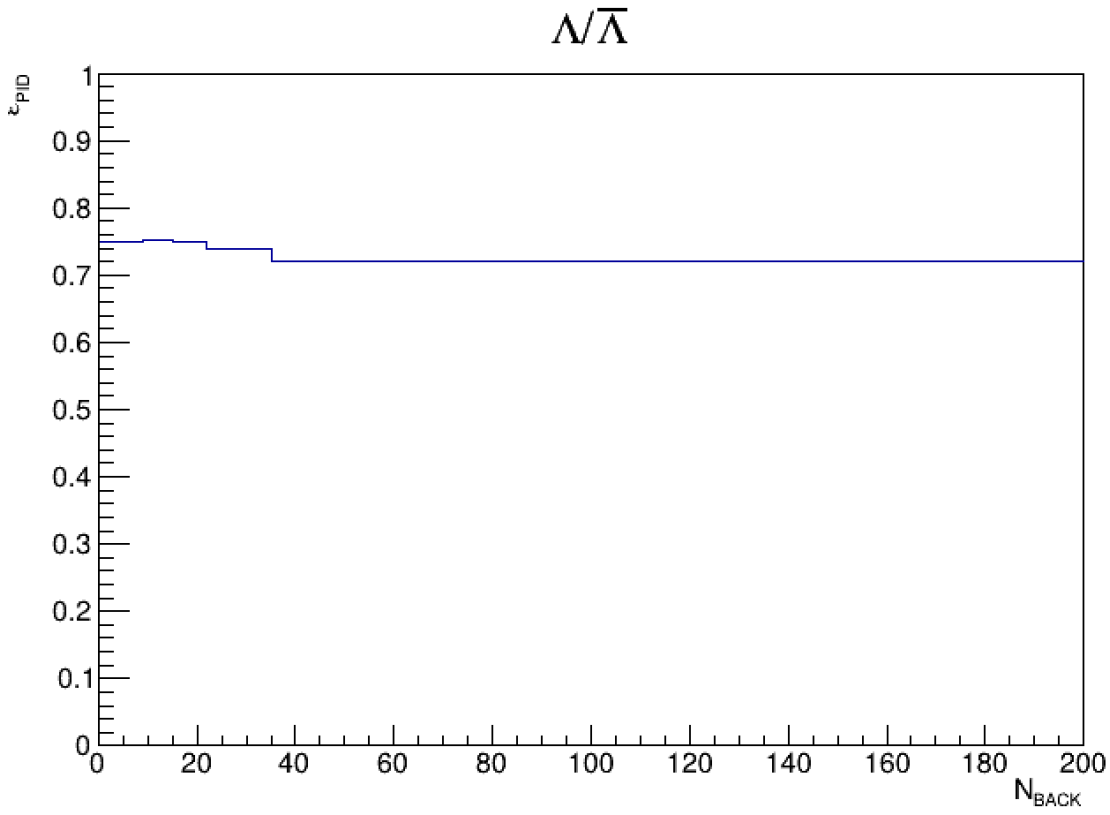


Figure D.3: Rebinned particle identification efficiencies for Λ candidates with daughter particles matching the selection criteria written out in section 3.1.

ε_{PID}				
Λ				
Multiplicity Class	MagDown		MagUp	
	N_{BACK}	N_{VELO}	N_{BACK}	N_{VELO}
V	0.748	0.751	0.753	0.759
IV	0.751	0.759	0.761	0.772
III	0.749	0.745	0.760	0.754
II	0.738	0.735	0.747	0.736
I	0.720	0.692	0.716	0.679

Table D.3: Summary of particle identification efficiencies for reconstructed Λ candidates.

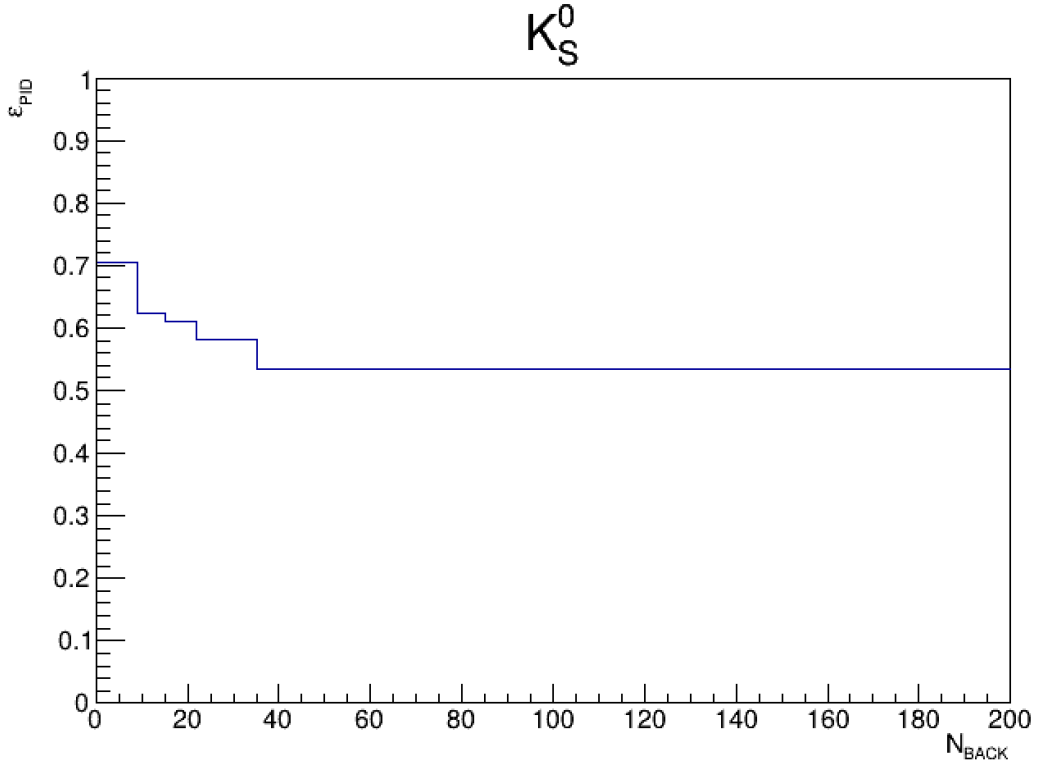


Figure D.4: Rebinned particle identification efficiencies for K^0_S candidates with daughter particles matching the selection criteria written out in section 3.1.

ε_{PID}				
K^0_S				
Multiplicity Class	MagDown		MagUp	
	N_{BACK}	N_{VELO}	N_{BACK}	N_{VELO}
V	0.704	0.672	0.574	0.708
IV	0.623	0.651	0.587	0.638
III	0.612	0.605	0.583	0.600
II	0.581	0.576	0.578	0.518
I	0.535	0.490	0.549	0.411

Table D.4: Summary of particle identification efficiencies for reconstructed K^0_S candidates.

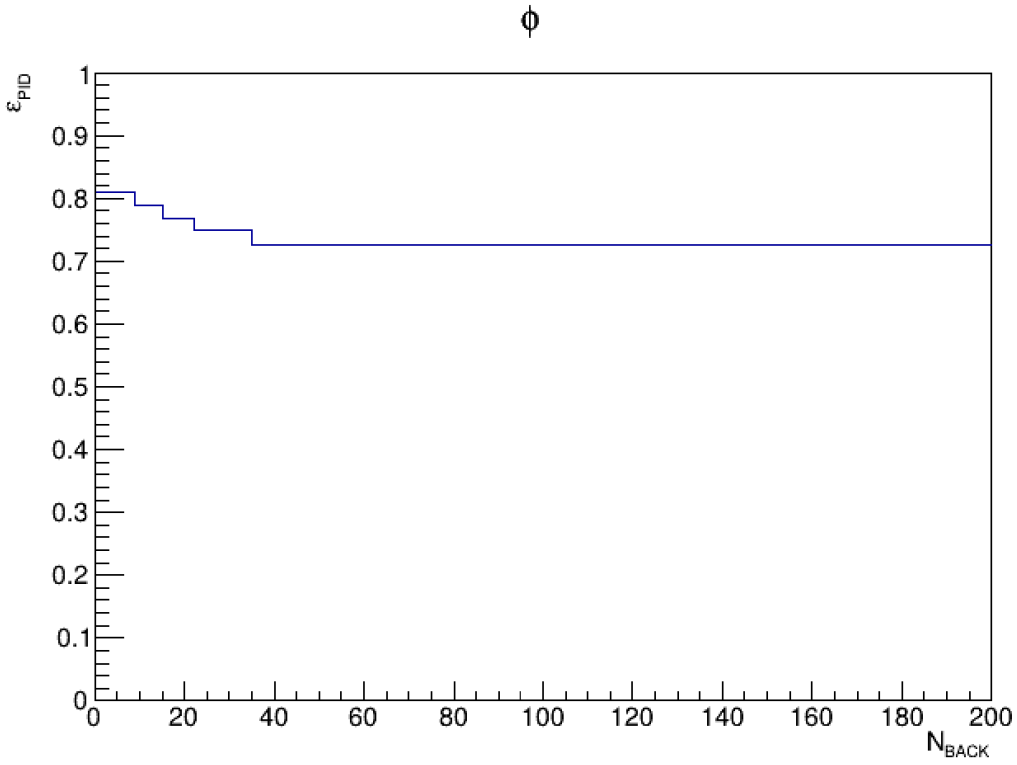


Figure D.5: Rebinned particle identification efficiencies for ϕ candidates with daughter particles matching the selection criteria written out in section 3.1.

ε_{PID}				
ϕ				
Multiplicity Class	MagDown		MagUp	
	N_{BACK}	N_{VELO}	N_{BACK}	N_{VELO}
V	0.811	0.822	0.796	0.822
IV	0.788	0.788	0.767	0.753
III	0.769	0.764	0.749	0.730
II	0.750	0.733	0.733	0.728
I	0.725	0.691	0.717	0.693

Table D.5: Summary of particle identification efficiencies for reconstructed ϕ candidates.

D.2 Reconstruction and Selection Efficiencies

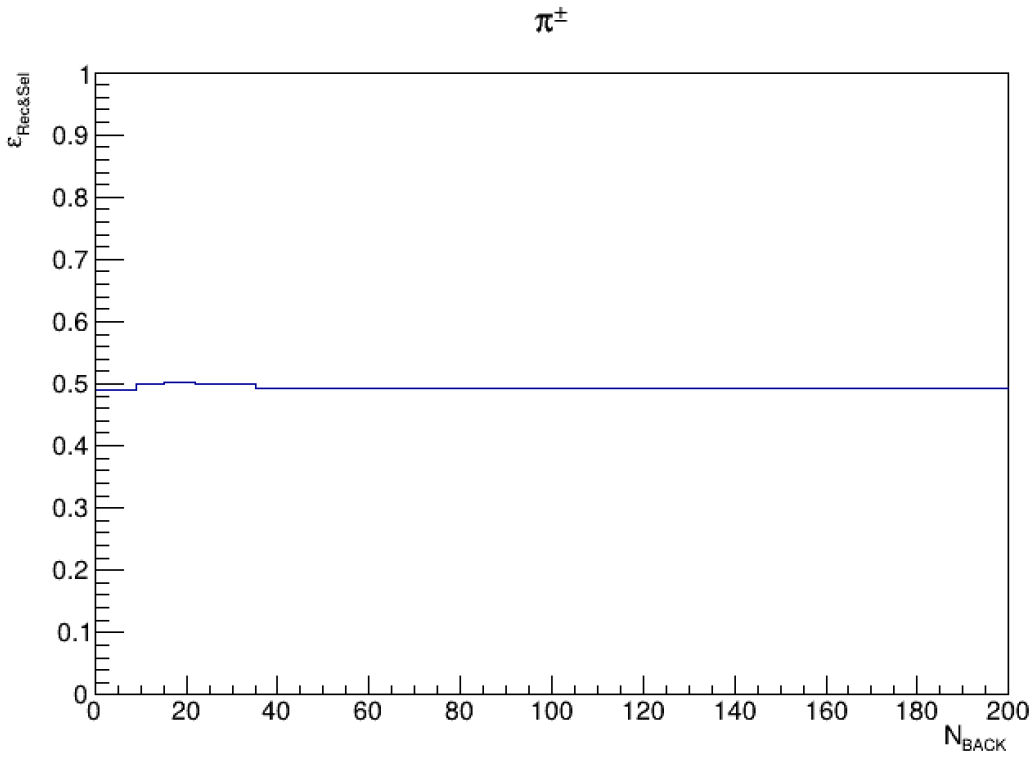


Figure D.6: Reconstruction and selection efficiencies corresponding to the relevant π^+ cuts from section 3.1.

$\varepsilon_{Rec\&Sel}$				
π^+				
Multiplicity Class	MagDown		MagUp	
	N_{BACK}	N_{VELO}	N_{BACK}	N_{VELO}
V	0.489	0.427	0.464	0.536
IV	0.501	0.448	0.500	0.558
III	0.503	0.448	0.507	0.539
II	0.500	0.442	0.508	0.515
I	0.492	0.421	0.498	0.504

Table D.6: Summary of Reconstruction and Selection Efficiencies for π candidates.

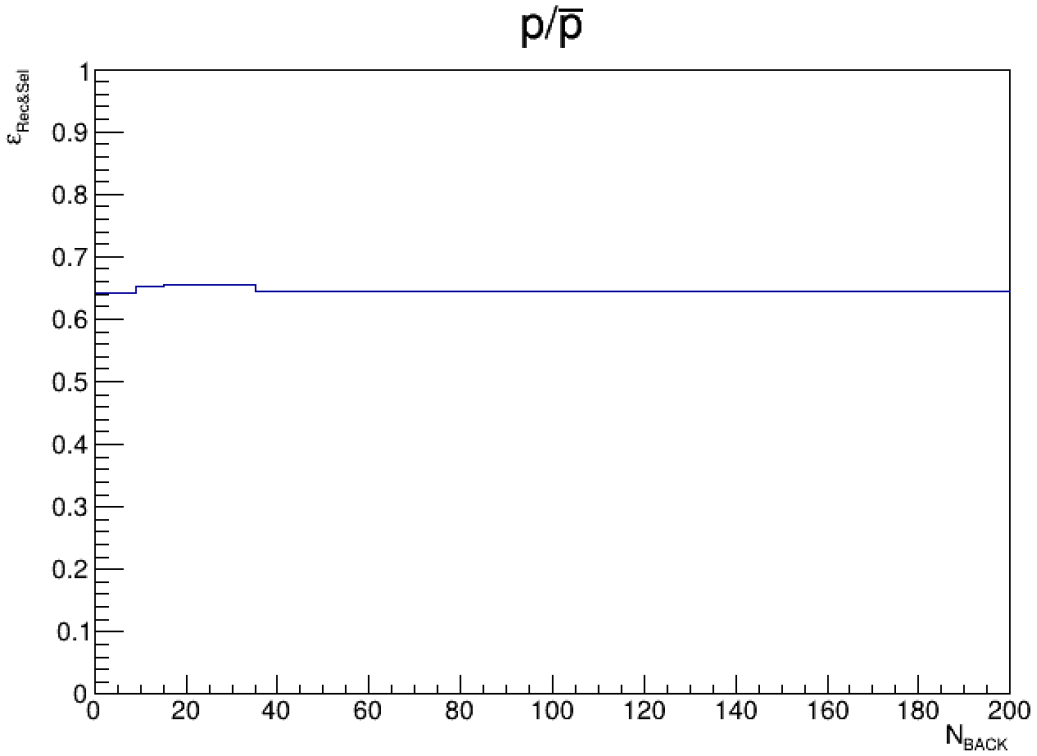


Figure D.7: Reconstruction and selection efficiencies corresponding to the relevant p cuts from section 3.1.

$\varepsilon_{Rec\&Sel}$				
p				
Multiplicity Class	MagDown		MagUp	
	N_{BACK}	N_{VELO}	N_{BACK}	N_{VELO}
V	0.642	0.650	0.657	0.670
IV	0.653	0.658	0.653	0.680
III	0.655	0.646	0.657	0.674
II	0.654	0.634	0.649	0.665
I	0.645	0.616	0.650	0.651

Table D.7: Summary of Reconstruction and Selection Efficiencies for p candidates.

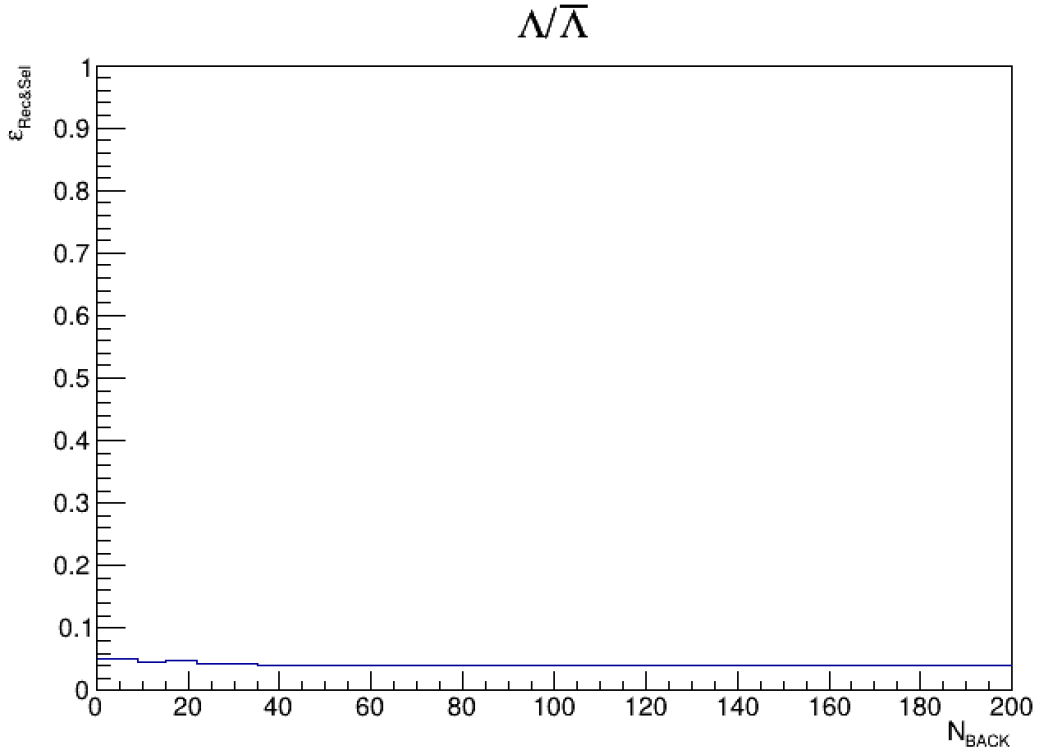


Figure D.8: Reconstruction and selection efficiencies corresponding to the relevant Λ cuts from section 3.1.

$\varepsilon_{Rec\&Sel}$				
Λ				
Multiplicity Class	MagDown		MagUp	
	N_{BACK}	N_{VELO}	N_{BACK}	N_{VELO}
V	0.050	0.045	0.051	0.047
IV	0.045	0.051	0.047	0.050
III	0.050	0.050	0.046	0.047
II	0.042	0.046	0.044	0.044
I	0.040	0.037	0.037	0.039

Table D.8: Summary of Reconstruction and Selection Efficiencies for Λ candidates.

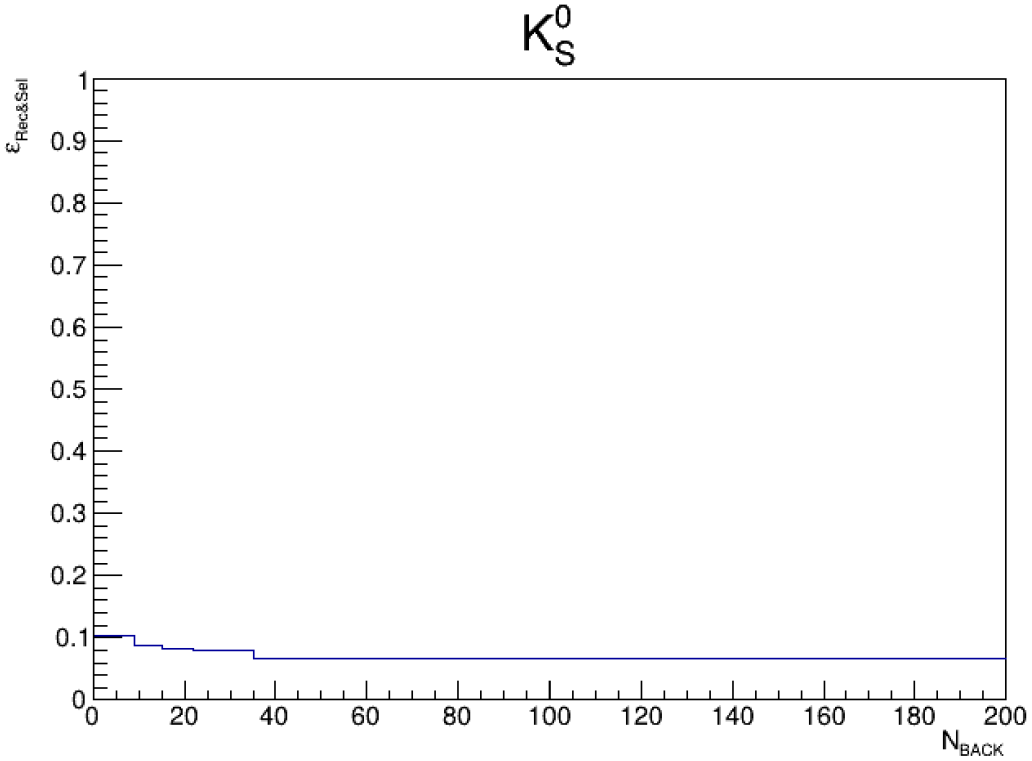


Figure D.9: Reconstruction and selection efficiencies corresponding to the relevant $\mathrm{K}^0_{\mathrm{S}}$ cuts from section 3.1.

$\varepsilon_{Rec\&Sel}$				
K^0_S				
Multiplicity Class	MagDown		MagUp	
	N_{BACK}	N_{VELO}	N_{BACK}	N_{VELO}
V	0.102	0.093	0.091	0.087
IV	0.089	0.089	0.087	0.082
III	0.084	0.082	0.079	0.078
II	0.080	0.071	0.071	0.066
I	0.068	0.061	0.060	0.051

Table D.9: Summary of Reconstruction and Selection Efficiencies for K^0_S candidates.

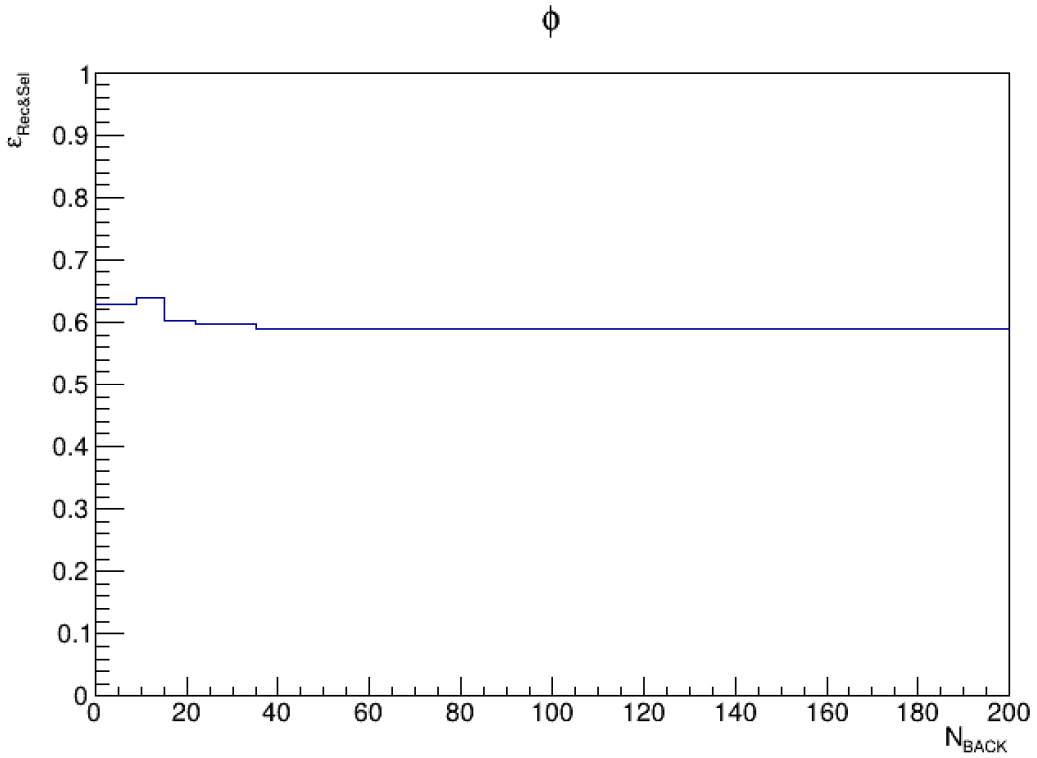


Figure D.10: Reconstruction and selection efficiencies corresponding to the relevant ϕ cuts from section 3.1.

$\varepsilon_{Rec\&Sel}$				
ϕ				
Multiplicity Class	MagDown		MagUp	
	N_{BACK}	N_{VELO}	N_{BACK}	N_{VELO}
V	0.630	0.643	0.588	0.579
IV	0.638	0.602	0.546	0.547
III	0.602	0.633	0.539	0.550
II	0.597	0.592	0.543	0.524
I	0.590	0.541	0.489	0.517

Table D.10: Summary of Reconstruction and Selection Efficiencies for ϕ candidates.

D.3 Acceptance Efficiencies

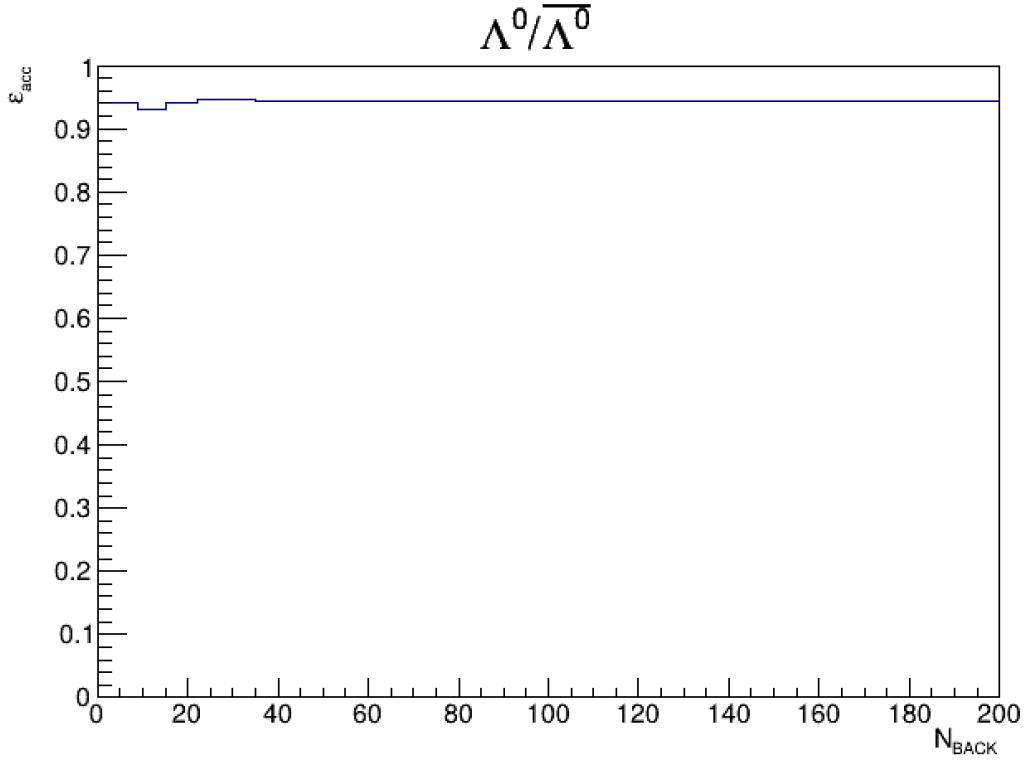


Figure D.11: Acceptance efficiencies corresponding to the daughter track geometric and kinematic distributions for Λ candidates.

ε_{acc}				
Λ				
Multiplicity Class	MagDown		MagUp	
	N_{BACK}	N_{VELO}	N_{BACK}	N_{VELO}
V	0.941	0.933	0.931	0.930
IV	0.932	0.945	0.940	0.946
III	0.941	0.941	0.944	0.942
II	0.946	0.947	0.948	0.949
I	0.944	0.945	0.948	0.949

Table D.11: Summary of Acceptance Efficiencies for Λ candidates.

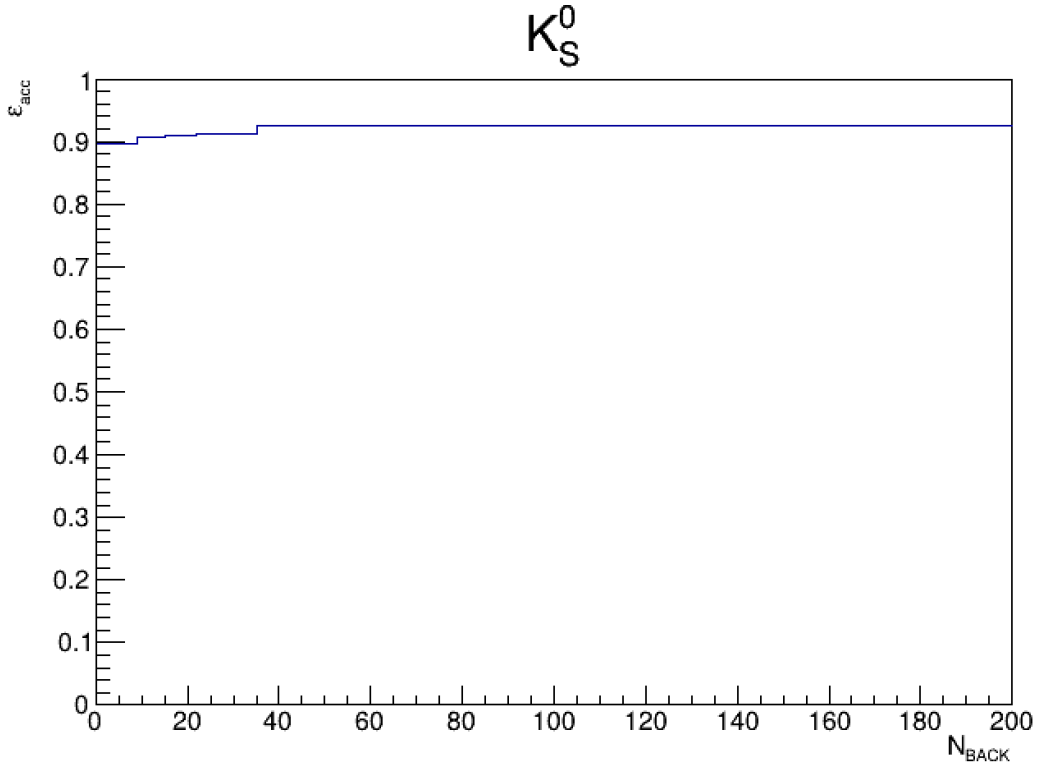


Figure D.12: Acceptance efficiencies corresponding to the daughter track geometric and kinematic distributions for $\mathrm{K}^0_{\mathrm{S}}$ candidates.

ε_{acc}				
K^0_S				
Multiplicity Class	MagDown		MagUp	
	N_{BACK}	N_{VELO}	N_{BACK}	N_{VELO}
V	0.896	0.890	0.900	0.891
IV	0.907	0.905	0.908	0.908
III	0.910	0.907	0.909	0.912
II	0.913	0.917	0.918	0.916
I	0.925	0.921	0.924	0.922

Table D.12: Summary of Acceptance Efficiencies for K^0_S candidates.

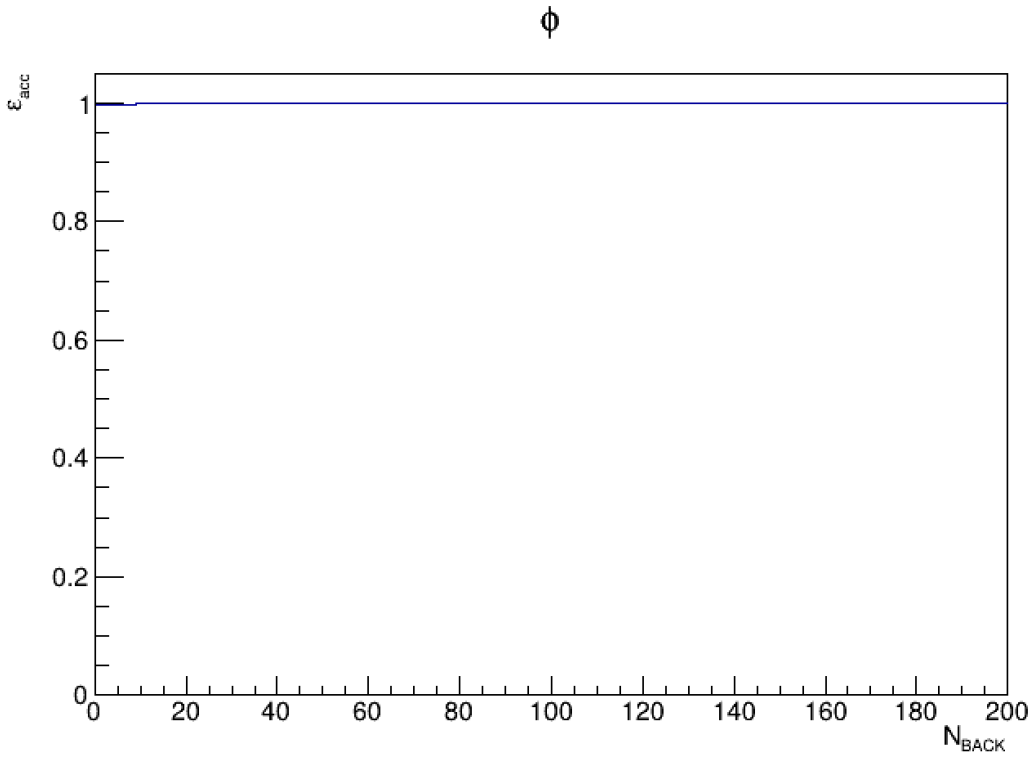


Figure D.13: Acceptance efficiencies corresponding to the daughter track geometric and kinematic distributions for ϕ candidates.

ε_{acc}				
ϕ				
Multiplicity Class	MagDown		MagUp	
	N_{BACK}	N_{VELO}	N_{BACK}	N_{VELO}
V	0.998	0.997	0.999	0.999
IV	0.998	0.999	0.999	0.999
III	0.999	1.000	0.999	0.998
II	0.999	0.999	1.000	1.000
I	0.999	0.996	0.999	1.000

Table D.13: Summary of Acceptance Efficiencies for ϕ candidates.

APPENDIX E

Summary of Systematic Uncertainties

E.1 Signal Extraction Uncertainties

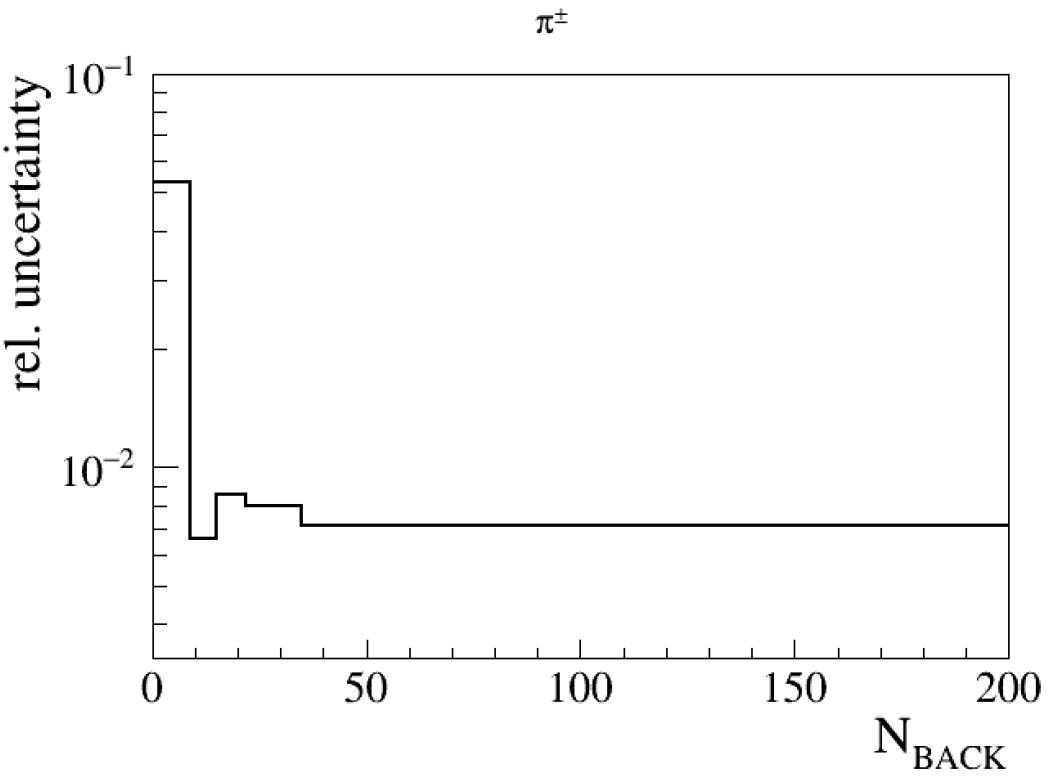


Figure E.1: Relative systematic errors originating from the fits to the charged pion $\log \chi^2_{\mathrm{IP}}$ distributions.

Systematic uncertainties from the Signal Extraction Fits				
π^+				
Multiplicity Class	MagDown		MagUp	
	N_{BACK}	N_{VELO}	N_{BACK}	N_{VELO}
V	5.301 %	0.211 %	0.721 %	3.973 %
IV	0.658 %	1.077 %	1.949 %	0.858 %
III	0.855 %	2.134 %	1.049 %	6.044 %
II	0.801 %	1.183 %	2.001 %	0.238 %
I	0.710 %	1.053 %	1.316 %	0.796 %

Table E.1: Summary of systematic errors from pion candidate signal extraction.

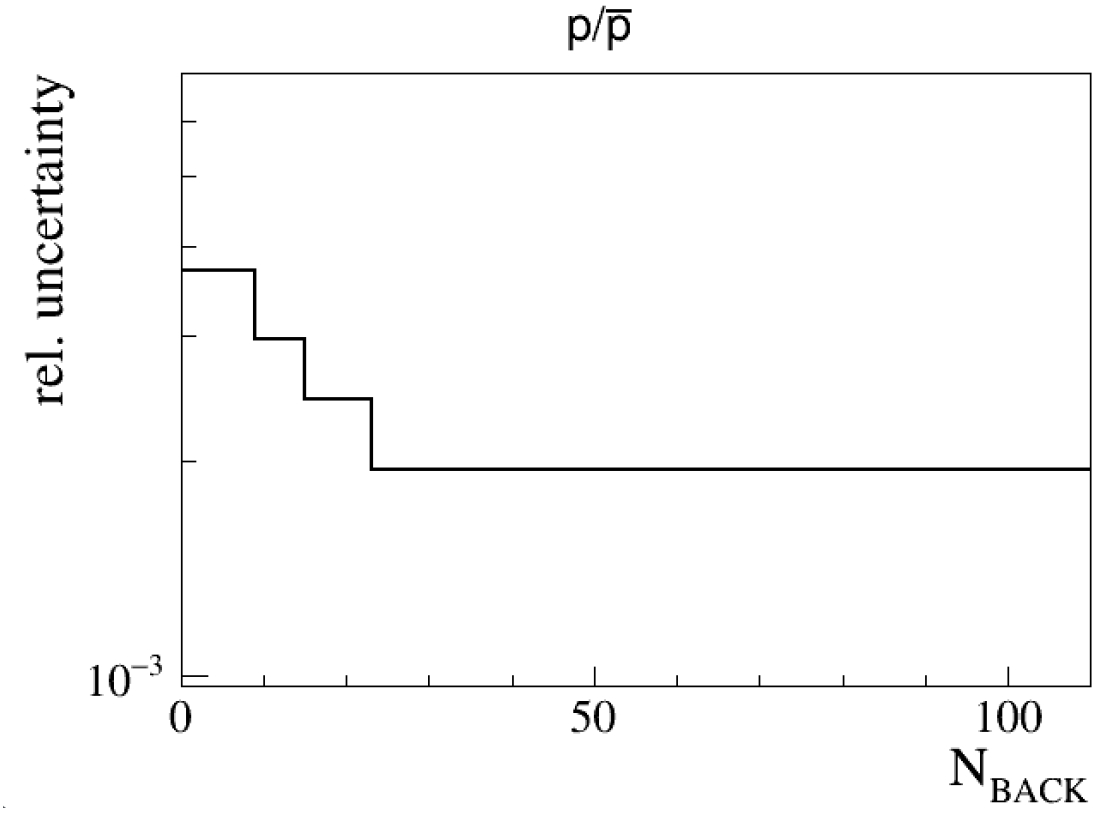


Figure E.2: Relative systematic errors originating from the fits to the p log χ^2_{IP} distributions.

Systematic uncertainties from the Signal Extraction Fits				
p				
Multiplicity Class	MagDown		MagUp	
	N_{BACK}	N_{VELO}	N_{BACK}	N_{VELO}
V	0.370 %	0.522 %	0.117 %	0.004 %
IV	0.297 %	0.181 %	0.0006 %	0.146 %
III	0.244 %	0.252 %	0.205 %	0.220 %
II	0.195 %	0.378 %	0.281 %	.0004 %
I	0.194 %	0.844 %	0.002 %	0.714 %

Table E.2: Summary of systematic errors from p candidate signal extraction.

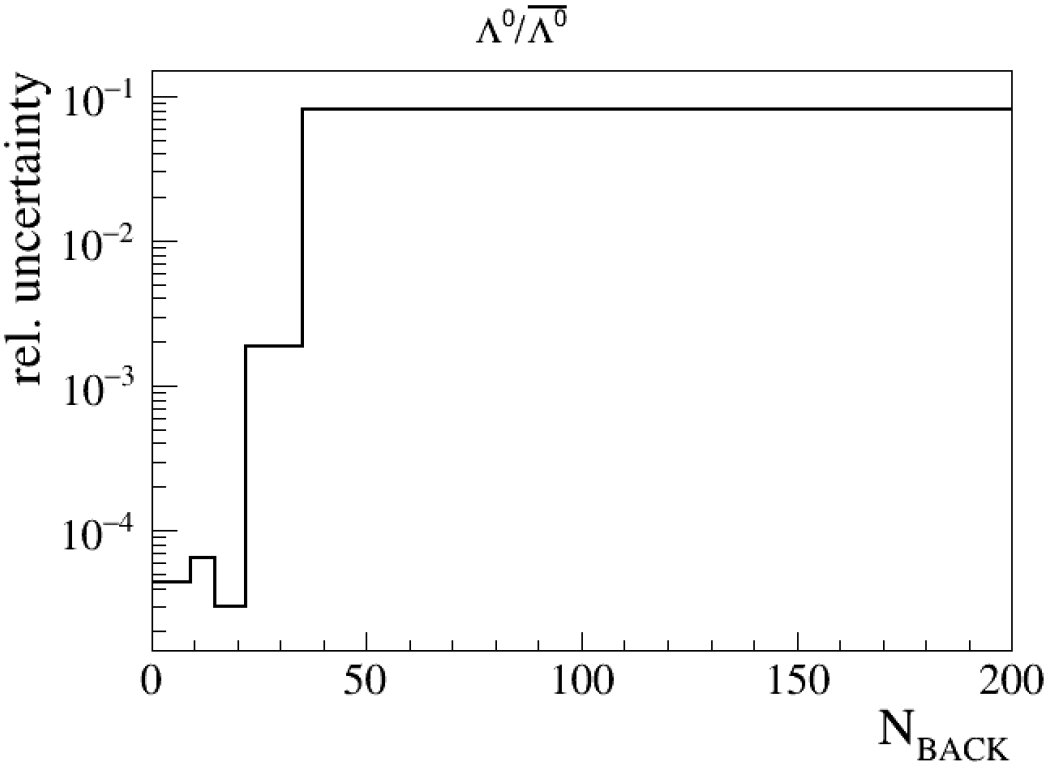


Figure E.3: Relative systematic errors originating from the fits to the Λ mass and $\log \chi^2_{\mathrm{IP}}$ distributions.

Systematic uncertainties from the Signal Extraction Fits				
Λ				
Multiplicity Class	MagDown		MagUp	
	N_{BACK}	N_{VELO}	N_{BACK}	N_{VELO}
V	0.004 %	0.004 %	0.003 %	0.004 %
IV	0.006 %	0.005 %	0.006%	0.005 %
III	0.003 %	0.003 %	0.006 %	0.006 %
II	0.188 %	0.103 %	0.095 %	0.095 %
I	8.041 %	9.456 %	8.130 %	9.091 %

Table E.3: Summary of systematic errors from Λ candidate signal extraction.

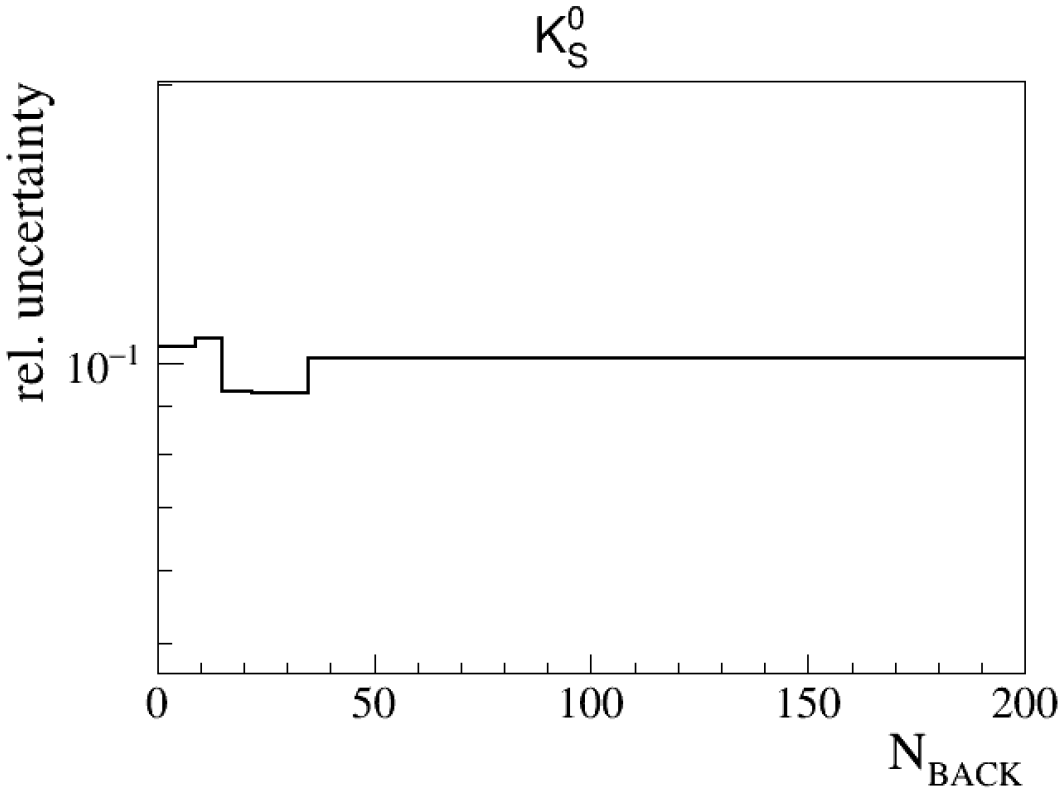


Figure E.4: Relative systematic errors originating from the fits to the K^0_S mass and $\log \chi^2_{IP}$ distributions.

Systematic uncertainties from the Signal Extraction Fits				
K^0_S				
Multiplicity Class	MagDown		MagUp	
	N_{BACK}	N_{VELO}	N_{BACK}	N_{VELO}
V	10.422 %	8.730 %	10.872 %	6.745 %
IV	10.663 %	8.454 %	11.676 %	8.939 %
III	9.335 %	8.285 %	6.200 %	7.800 %
II	9.299 %	7.915 %	9.835 %	8.584 %
I	10.148 %	11.647%	8.187 %	10.391 %

Table E.4: Summary of systematic errors from K^0_S candidate signal extraction.

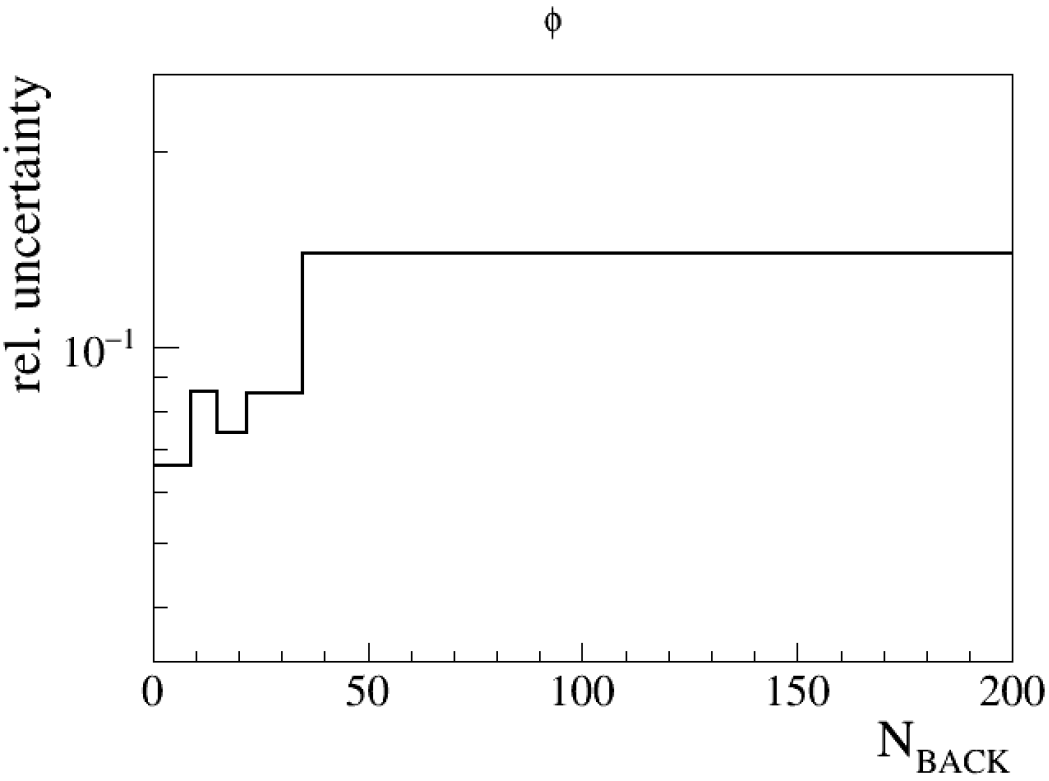


Figure E.5: Relative systematic errors originating from the fits to the ϕ mass and $\log \chi^2_{\mathrm{IP}}$ distributions.

Systematic uncertainties from the Signal Extraction Fits				
ϕ				
Multiplicity Class	MagDown		MagUp	
	N_{BACK}	N_{VELO}	N_{BACK}	N_{VELO}
V	6.607 %	5.275 %	1.882 %	1.781 %
IV	8.545 %	4.712%	0.432 %	2.567 %
III	7.419 %	9.617 %	4.905 %	3.223 %
II	8.531 %	10.109 %	3.290 %	4.347 %
I	13.926 %	13.610 %	9.033 %	7.447 %

Table E.5: Summary of systematic errors from ϕ candidate signal extraction.

E.1.0.1 Tracking Systematics

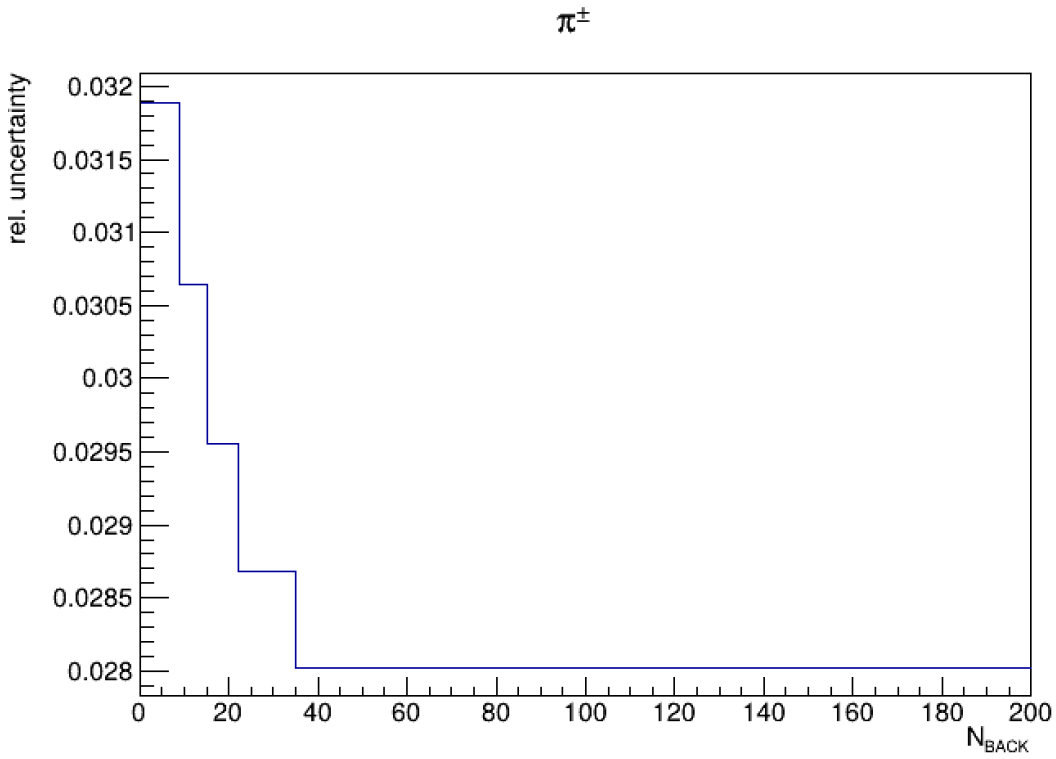


Figure E.6: Relative systematic errors originating from the uncertainties on the tracking efficiency corrections from TrackCalib.

Systematic uncertainties from the Tracking Corrections				
π^+				
Multiplicity Class	MagDown		MagUp	
	N_{BACK}	N_{VELO}	N_{BACK}	N_{VELO}
V	3.189 %	3.259 %	1.232 %	1.265 %
IV	3.065 %	3.005 %	1.148 %	1.114 %
III	2.956 %	2.865 %	1.099 %	1.062 %
II	2.868 %	2.756 %	1.055 %	1.016 %
I	2.802 %	2.669 %	1.013 %	0.975 %

Table E.6: Summary of systematic errors corresponding to tracking corrections on π^+ Long Tracks.

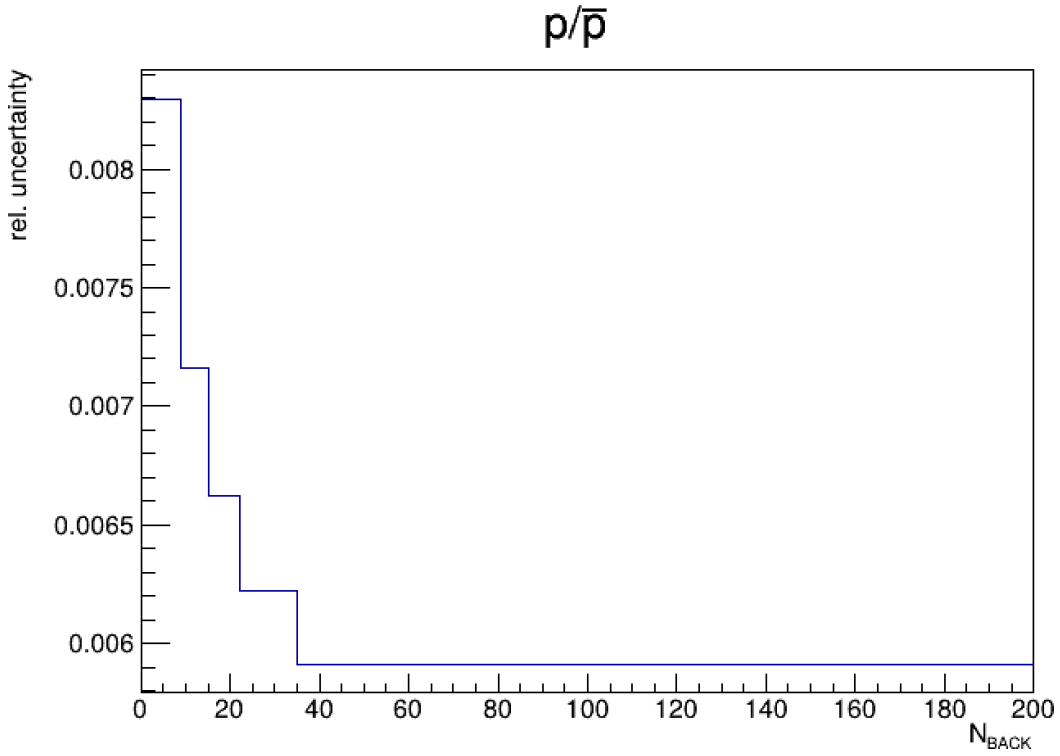


Figure E.7: Relative systematic errors originating from the uncertainties on the tracking efficiency corrections from TrackCalib.

Systematic uncertainties from the Tracking Corrections				
p				
Multiplicity Class	MagDown		MagUp	
	N_{BACK}	N_{VELO}	N_{BACK}	N_{VELO}
V	0.830 %	0.848 %	0.786 %	0.841 %
IV	0.716 %	0.677 %	0.693 %	0.672 %
III	0.663 %	0.625 %	0.639 %	0.620 %
II	0.622 %	0.591 %	0.610 %	0.580 %
I	0.591 %	0.556 %	0.575 %	0.553 %

Table E.7: Summary of systematic errors corresponding to tracking corrections on p Long Tracks.

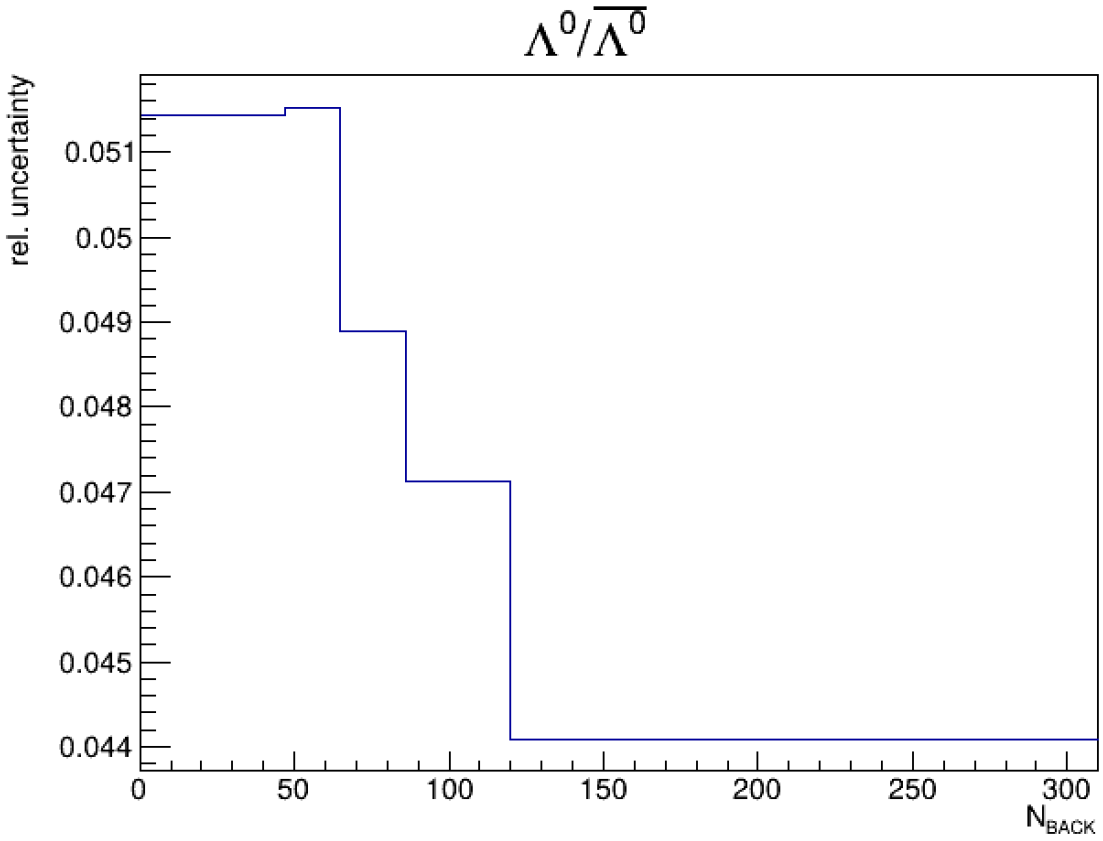


Figure E.8: Relative systematic errors originating from the uncertainties on the tracking efficiency corrections from TrackCalib.

Systematic uncertainties from the Tracking Corrections				
Λ				
Multiplicity Class	MagDown		MagUp	
	N_{BACK}	N_{VELO}	N_{BACK}	N_{VELO}
V	5.143 %	5.143 %	2.836 %	2.835 %
IV	5.153 %	5.153 %	2.725 %	2.733 %
III	4.890 %	4.893 %	2.651 %	2.651 %
II	4.712 %	4.718 %	2.550 %	2.549 %
I	4.408 %	4.456 %	2.357 %	2.366 %

Table E.8: Summary of systematic errors corresponding to tracking corrections on Λ candidates from the p and π^+ daughters.

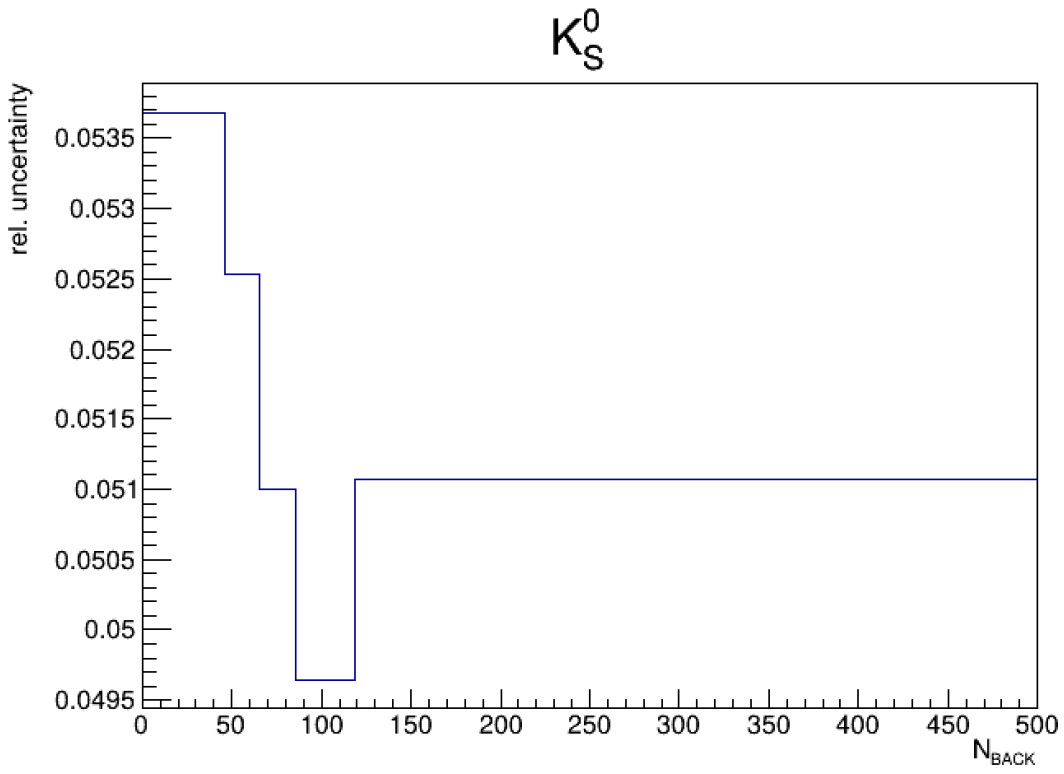


Figure E.9: Relative systematic errors originating from the uncertainties on the tracking efficiency corrections from TrackCalib.

Systematic uncertainties from the Tracking Corrections				
K^0_S				
Multiplicity Class	MagDown		MagUp	
	N_{BACK}	N_{VELO}	N_{BACK}	N_{VELO}
V	5.368 %	5.368 %	2.818 %	2.685 %
IV	5.253 %	5.253 %	2.528 %	2.598 %
III	5.100 %	5.100 %	2.409 %	2.552 %
II	4.964 %	4.964 %	2.267 %	2.349 %
I	5.107 %	5.107 %	2.100 %	2.326 %

Table E.9: Summary of systematic errors corresponding to tracking corrections on K^0_S candidates from the charged pion daughters.

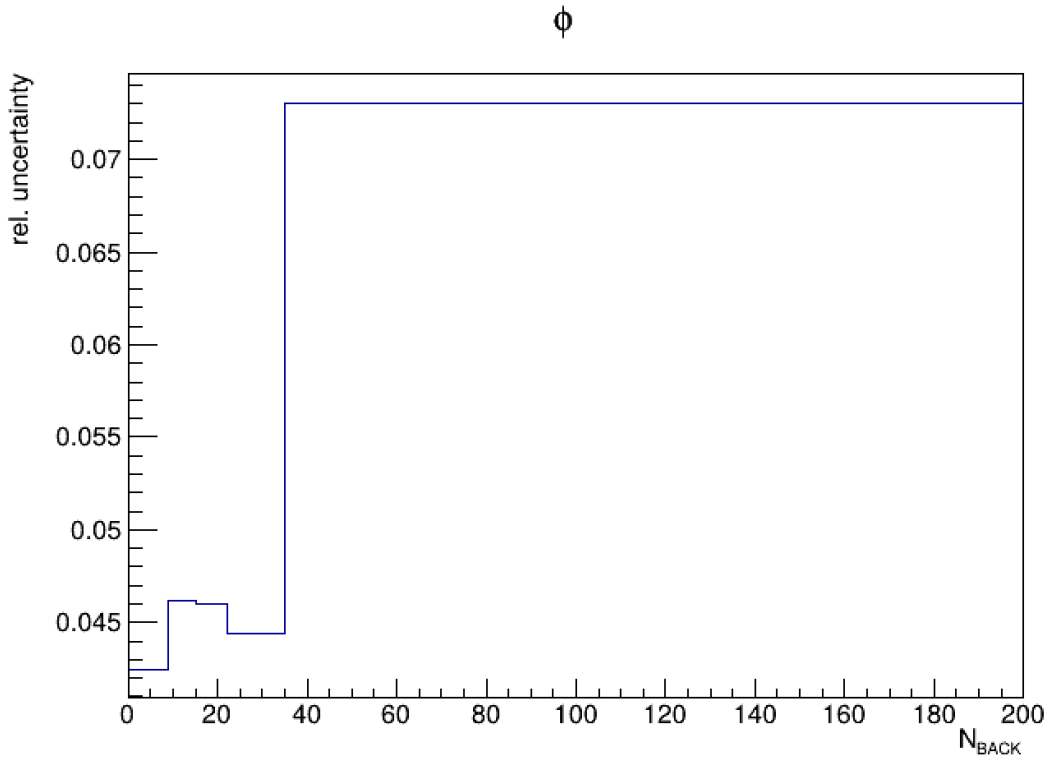


Figure E.10: Relative systematic errors originating from the uncertainties on the tracking efficiency corrections from TrackCalib.

Systematic uncertainties from the Tracking Corrections				
ϕ				
Multiplicity Class	MagDown		MagUp	
	N_{BACK}	N_{VELO}	N_{BACK}	N_{VELO}
V	4.244 %	3.856 %	3.932 %	3.877 %
IV	4.619 %	4.669 %	4.651 %	4.445 %
III	4.597 %	4.703 %	4.787 %	4.685 %
II	4.444 %	4.685 %	4.678 %	4.885 %
I	7.305 %	8.147 %	7.526 %	8.685 %

Table E.10: Summary of systematic errors corresponding to tracking corrections on ϕ candidates from the charged kaon daughters.

E.1.0.2 Particle Identification Systematics

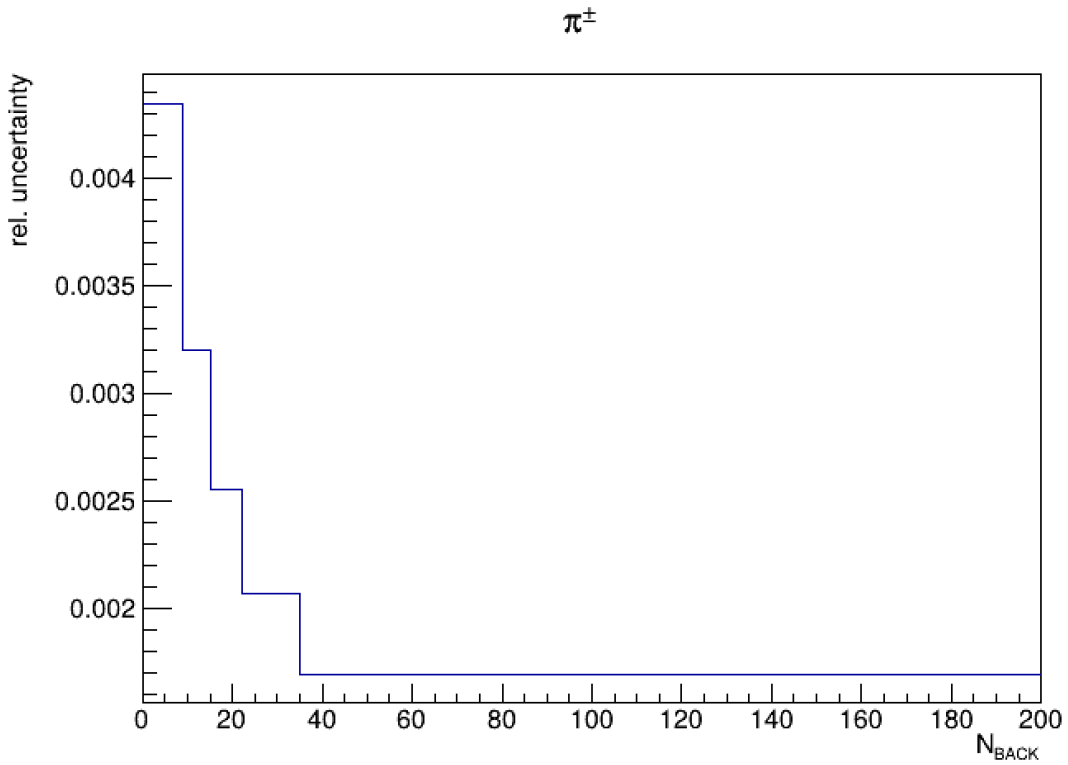


Figure E.11: Relative systematic errors originating from the uncertainties on the particle identification efficiency from PIDCalib.

Systematic uncertainties from PID Efficiencies				
π^+				
Multiplicity Class	MagDown		MagUp	
	N_{BACK}	N_{VELO}	N_{BACK}	N_{VELO}
V	0.435 %	0.461 %	4.485 %	4.964 %
IV	0.320 %	0.270 %	3.325 %	2.709 %
III	0.255 %	0.204 %	2.628 %	2.042 %
II	0.207 %	0.163 %	2.098 %	1.614 %
I	0.169 %	0.131 %	1.710 %	1.285 %

Table E.11: Summary of systematic errors corresponding to PID efficiencies on π^+ candidates.

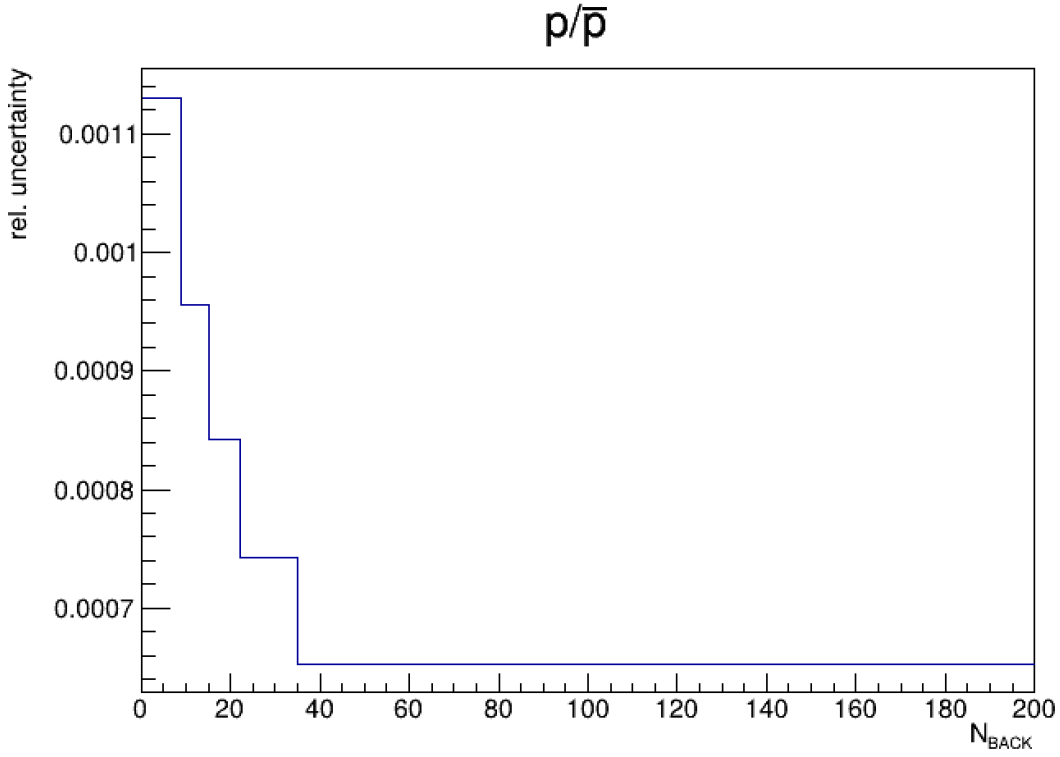


Figure E.12: Relative systematic errors originating from the uncertainties on the particle identification efficiency from PIDCalib.

Systematic uncertainties from PID Efficiencies				
p				
Multiplicity Class	MagDown		MagUp	
	N_{BACK}	N_{VELO}	N_{BACK}	N_{VELO}
V	0.113 %	0.118 %	1.226 %	1.340 %
IV	0.096 %	0.089 %	1.079 %	1.063 %
III	0.084 %	0.075 %	0.959 %	0.890 %
II	0.074 %	0.065 %	0.850 %	0.763 %
I	0.065 %	0.055 %	0.752 %	0.648 %

Table E.12: Summary of systematic errors corresponding to PID efficiencies on p candidates.

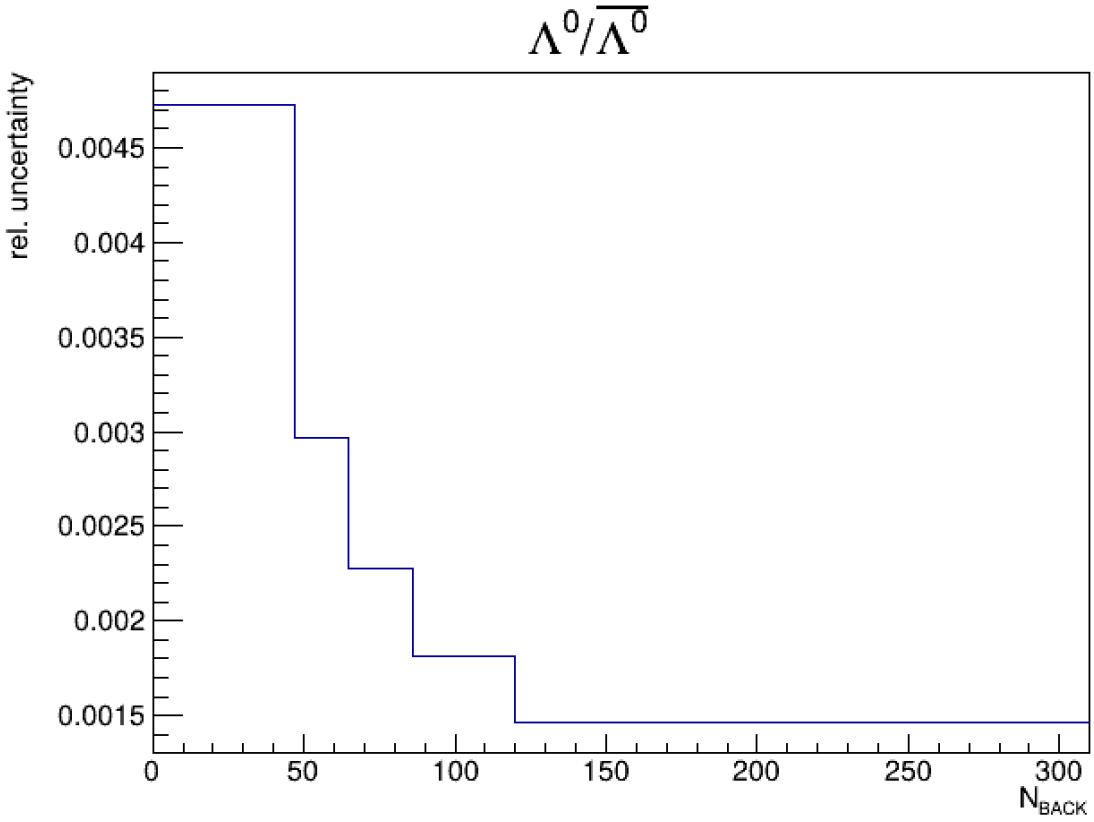


Figure E.13: Relative systematic errors originating from the uncertainties on the particle identification efficiency from PIDCalib.

Systematic uncertainties from PID Efficiencies				
Λ				
Multiplicity Class	MagDown		MagUp	
	N_{BACK}	N_{VELO}	N_{BACK}	N_{VELO}
V	0.473 %	0.473 %	0.393 %	0.452 %
IV	0.296 %	0.296 %	0.306 %	0.272 %
III	0.228 %	0.228 %	0.245 %	0.209 %
II	0.182 %	0.182 %	0.213 %	0.175 %
I	0.146 %	0.148 %	0.177 %	0.138 %

Table E.13: Summary of systematic errors corresponding to PID efficiencies on Λ candidates from the p and π^+ daughters.

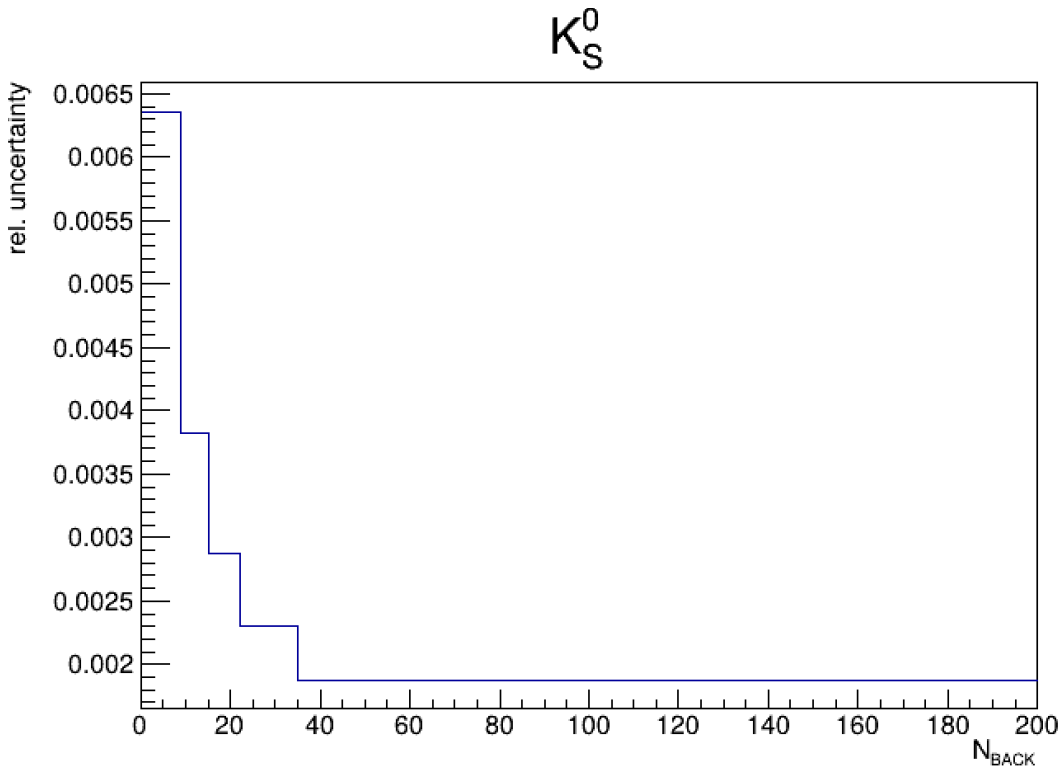


Figure E.14: Relative systematic errors originating from the uncertainties on the particle identification efficiency from PIDCalib.

Systematic uncertainties from PID Efficiencies				
K^0_S				
Multiplicity Class	MagDown		MagUp	
	N_{BACK}	N_{VELO}	N_{BACK}	N_{VELO}
V	0.636 %	0.636 %	7.236 %	6.749 %
IV	0.383 %	0.383 %	4.201 %	3.847 %
III	0.287 %	0.287 %	3.139 %	2.849 %
II	0.230 %	0.230 %	2.416 %	2.265 %
I	0.187 %	0.187 %	1.907 %	1.836 %

Table E.14: Summary of systematic errors corresponding to PID efficiencies on K^0_S candidates from the π^+ and π^- daughters.

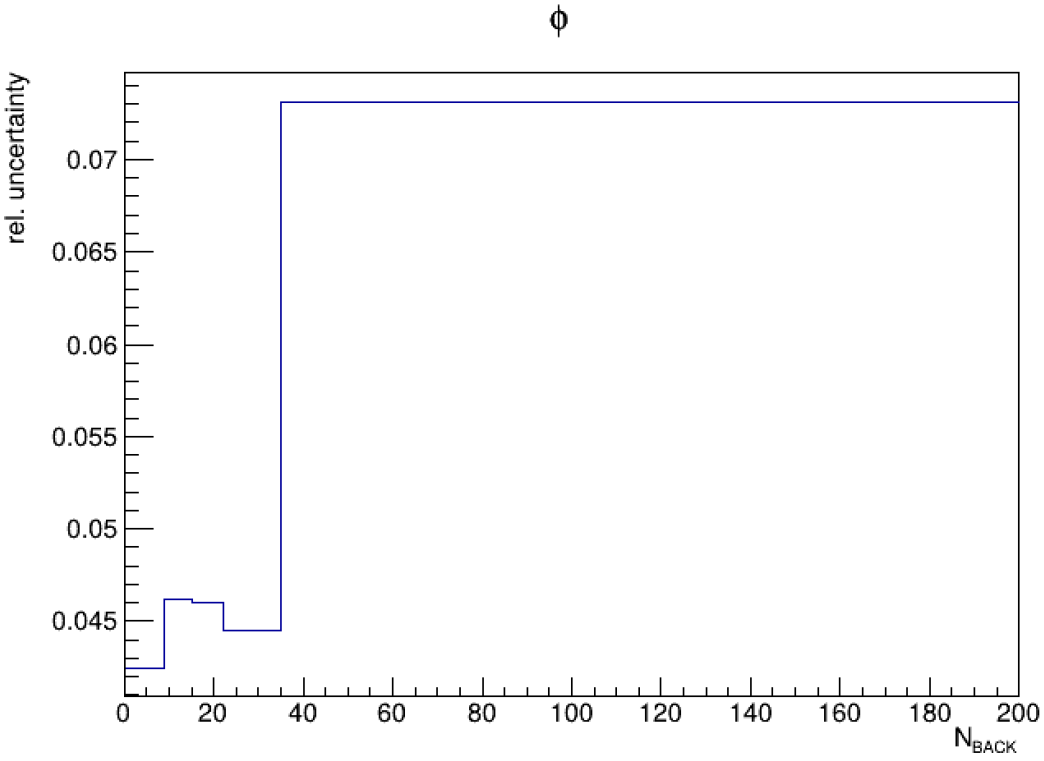


Figure E.15: Relative systematic errors originating from the uncertainties on the particle identification efficiency from PIDCalib.

Systematic uncertainties from PID Efficiencies				
ϕ				
Multiplicity Class	MagDown		MagUp	
	N_{BACK}	N_{VELO}	N_{BACK}	N_{VELO}
V	4.245 %	3.856 %	3.935 %	3.877 %
IV	4.621 %	4.669 %	4.654 %	4.445 %
III	4.600 %	4.703 %	4.789 %	4.685 %
II	4.448 %	4.685 %	4.680 %	4.885 %
I	7.313 %	8.147 %	7.528 %	8.685 %

Table E.15: Summary of systematic errors corresponding to PID efficiencies on ϕ candidates from the K^+ and K^- daughters.

E.1.1 Acceptance Efficiency Systematics

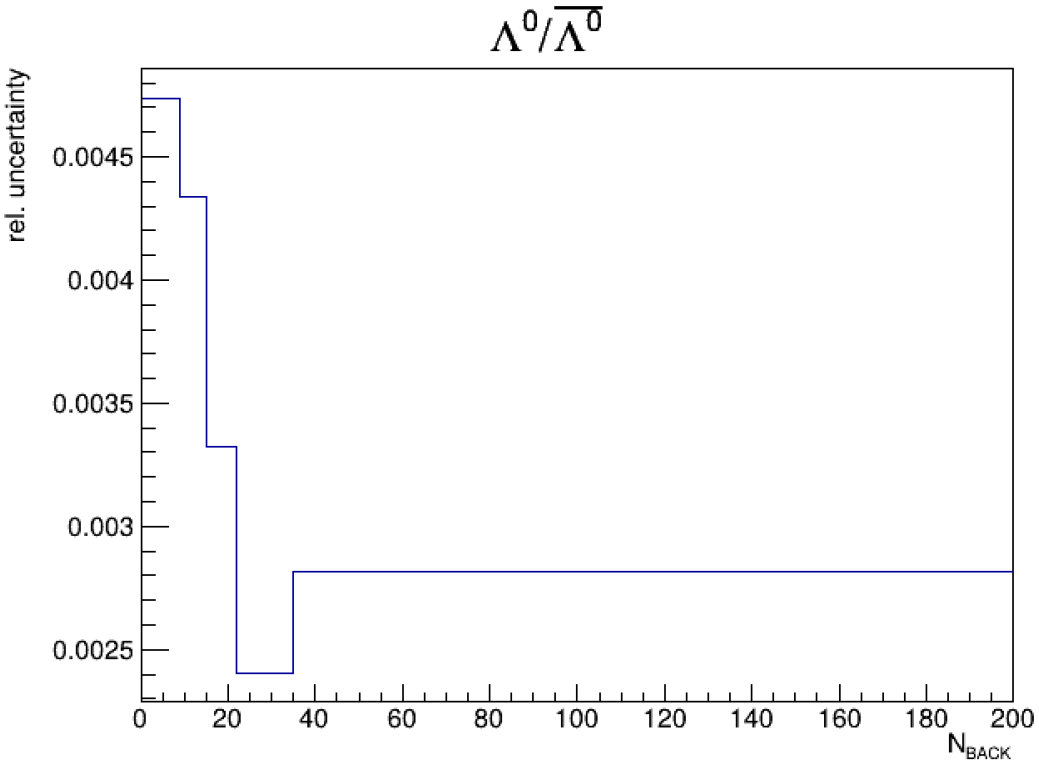


Figure E.16: Relative systematic errors originating from the uncertainties on the Monte-Carlo acceptance fractions for Λ candidates.

Systematic uncertainties from ε_{acc}				
Λ				
Multiplicity Class	MagDown		MagUp	
	N_{BACK}	N_{VELO}	N_{BACK}	N_{VELO}
V	0.474 %	0.594 %	0.500 %	0.628 %
IV	0.434 %	0.418 %	0.417 %	0.420 %
III	0.332 %	0.350 %	0.341 %	0.351 %
II	0.240 %	0.254 %	0.253 %	0.255 %
I	0.281 %	0.244 %	0.296 %	0.257 %

Table E.16: Summary of systematic errors originating from uncertainties on p and π^+ daughter acceptance fractions.

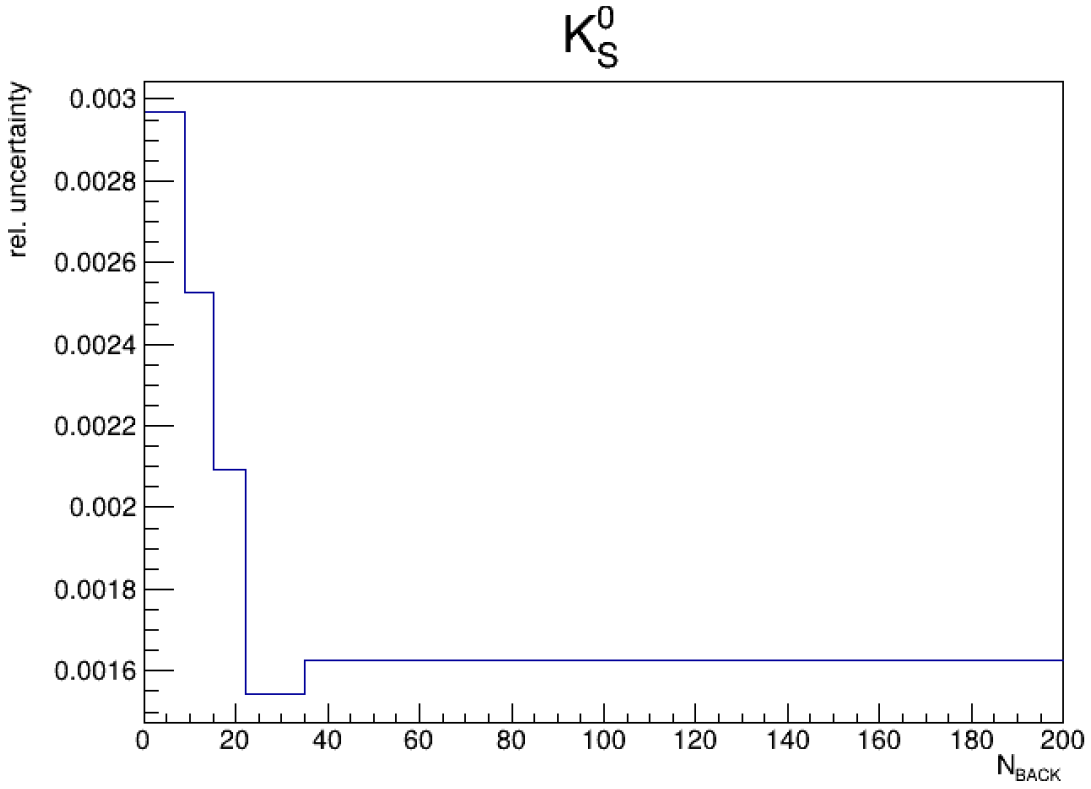


Figure E.17: Relative systematic errors originating from the uncertainties on the Monte-Carlo acceptance fractions for $\mathrm{K}^0_{\mathrm{S}}$ candidates.

Systematic uncertainties from ε_{acc}				
K^0_S				
Multiplicity Class	MagDown		MagUp	
	N_{BACK}	N_{VELO}	N_{BACK}	N_{VELO}
V	0.331 %	0.383 %	0.281 %	0.386 %
IV	0.279 %	0.287 %	0.257 %	0.286 %
III	0.230 %	0.226 %	0.220 %	0.220 %
II	0.169 %	0.170 %	0.156 %	0.173 %
I	0.176 %	0.159%	0.172 %	0.169 %

Table E.17: Summary of systematic errors originating from uncertainties on π^+ and π^- daughter acceptance fractions.

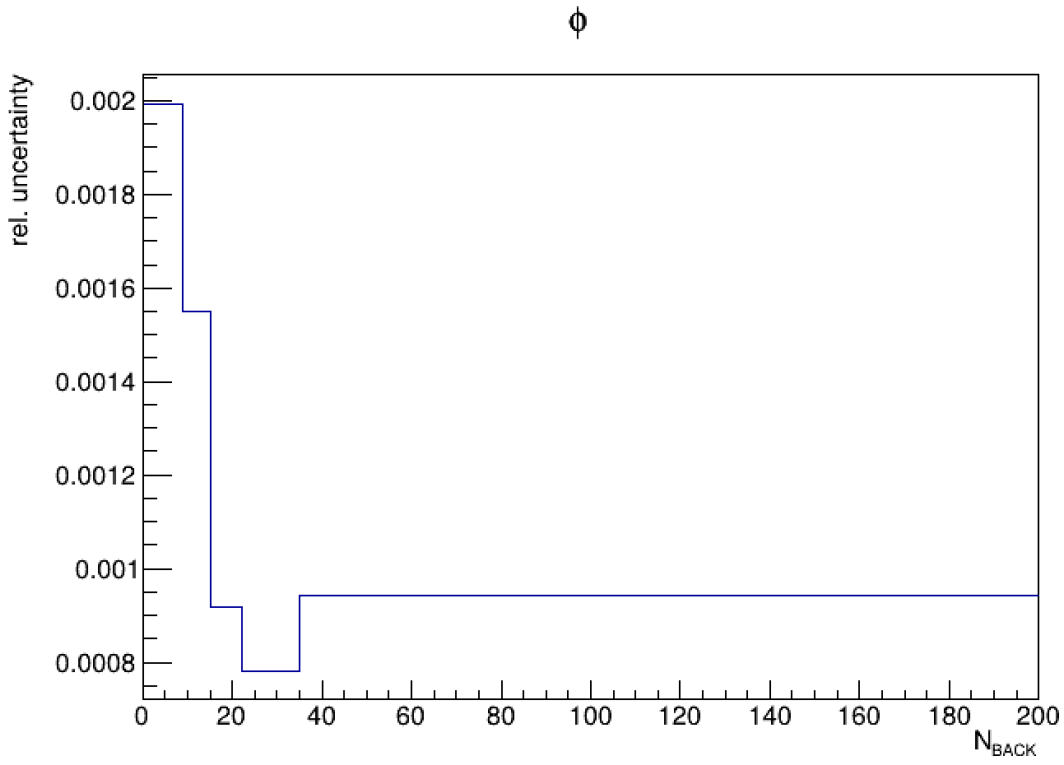


Figure E.18: Relative systematic errors originating from the uncertainties on the Monte-Carlo acceptance fractions for ϕ candidates.

Systematic uncertainties from ε_{acc}				
ϕ				
Multiplicity Class	MagDown		MagUp	
	N_{BACK}	N_{VELO}	N_{BACK}	N_{VELO}
V	0.199 %	0.244 %	0.094 %	0.130 %
IV	0.155 %	0.108 %	0.160 %	0.114 %
III	0.092 %	0.060 %	0.109 %	0.134 %
II	0.078 %	0.069 %	0.103 %	0.049 %
I	0.094 %	0.167%	0.120 %	1.021 %

Table E.18: Summary of systematic errors originating from uncertainties on K^+ and K^- daughter acceptance fractions.

APPENDIX F

ALICE Comparison Plots With Respect to Multiplicity Percentile

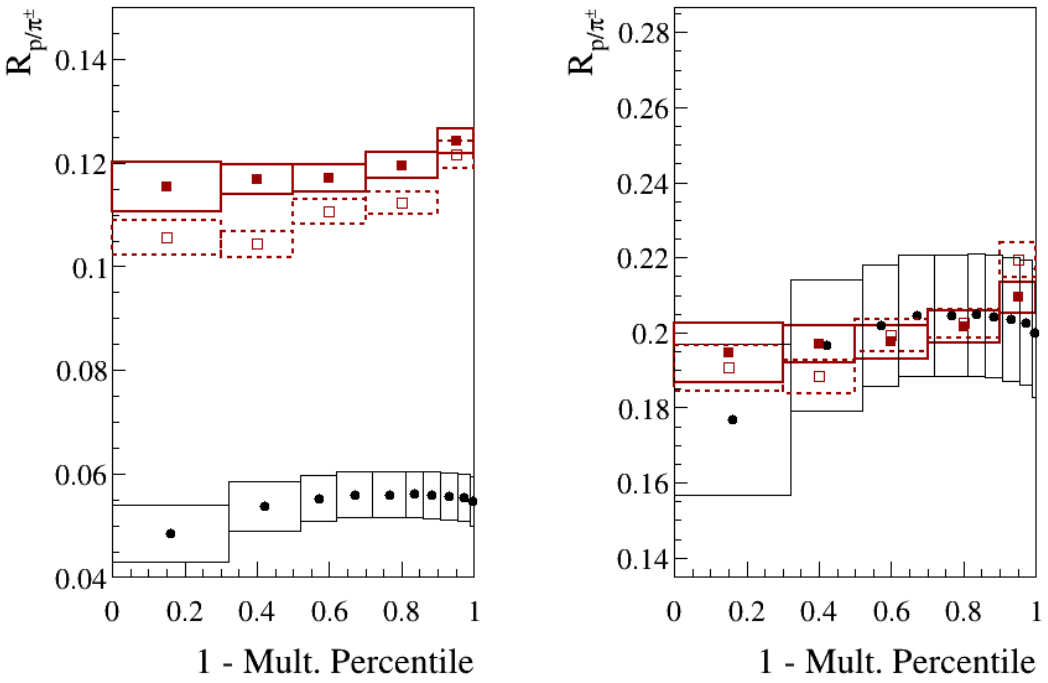


Figure F.1: Absolute (left) and normalized (right) multiplicity-dependent (Dark Red) $\frac{p+\bar{p}}{\pi^{+}+\pi^{-}}$ yield ratios with respect to multiplicity percentile. Results with respect to N_{BACK} (solid, filled) and N_{VELO} (open, dashed) are provided along with results from ALICE(12) (Black) in pp collisions at $\sqrt{s} = 13$ TeV. Charged track density and average event activity is increasing from left to right.

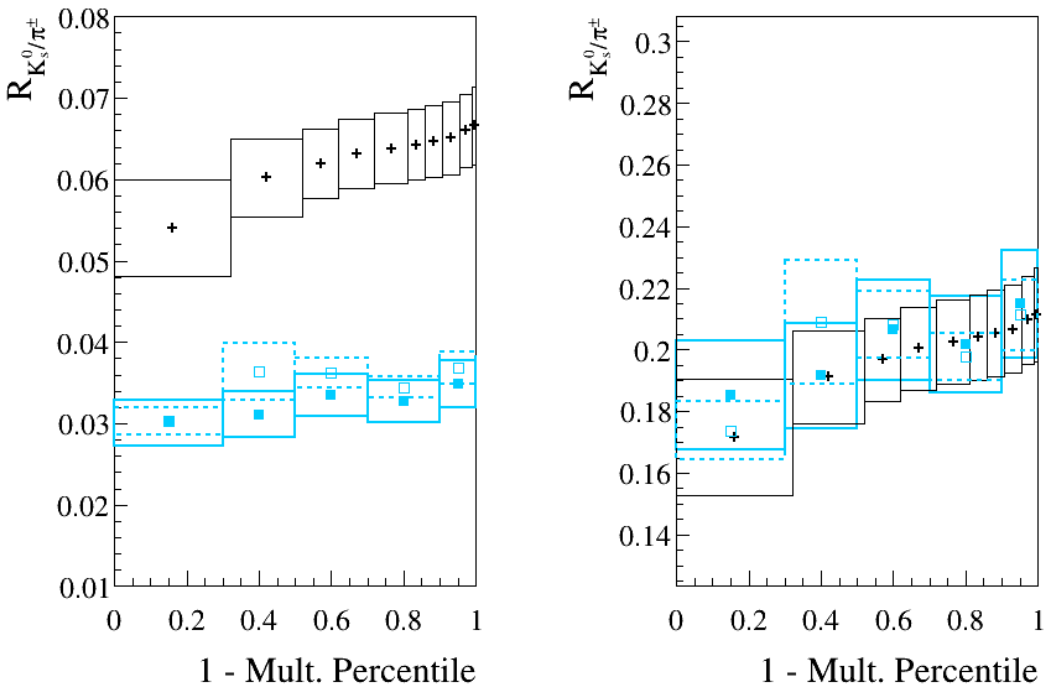


Figure F.2: Absolute (left) and normalized (right) multiplicity-dependent (Cyan) $\frac{\mathrm{K_S^0}}{\pi^+ + \pi^-}$ yield ratios with respect to multiplicity percentile. Results with respect to N_{BACK} (solid, filled) and N_{VELO} (open, dashed) are provided along with results from ALICE(12) (Black) in pp collisions at $\sqrt{s} = 13$ TeV. Charged track density and average event activity is increasing from left to right.

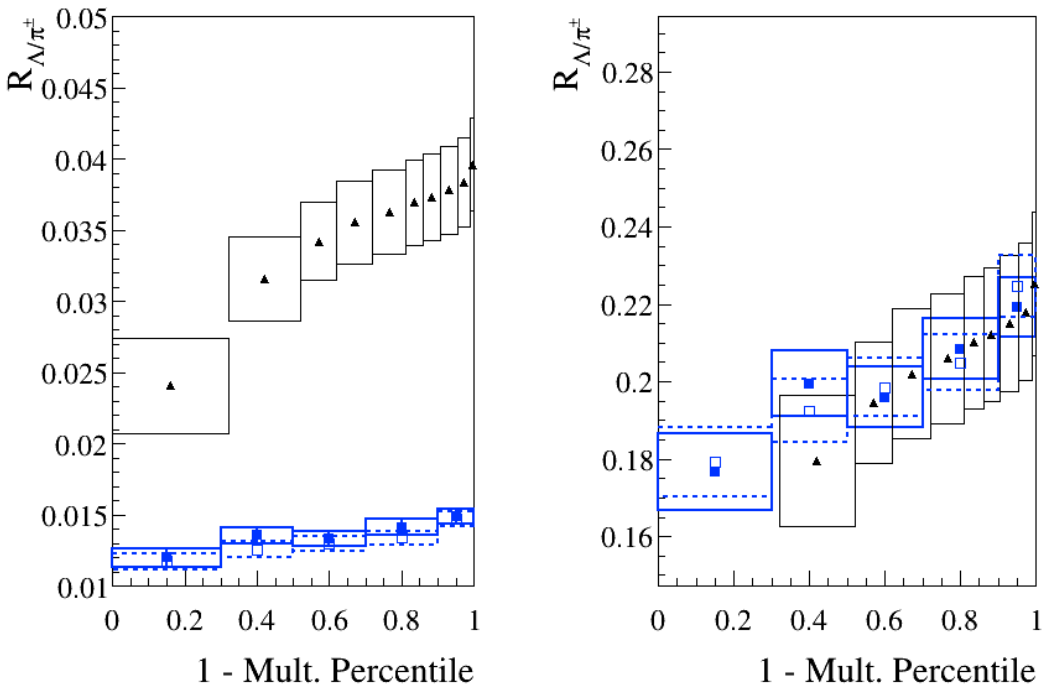


Figure F.3: Absolute (left) and normalized (right) multiplicity-dependent (Blue) $\frac{\Lambda+\bar{\Lambda}}{\pi^+ + \pi^-}$ yield ratios with respect to multiplicity percentile. Results with respect to N_{BACK} (solid, filled) and N_{VELO} (open, dashed) are provided along with results from ALICE(12) (Black) in pp collisions at $\sqrt{s} = 13$ TeV. Charged track density and average event activity is increasing from left to right.

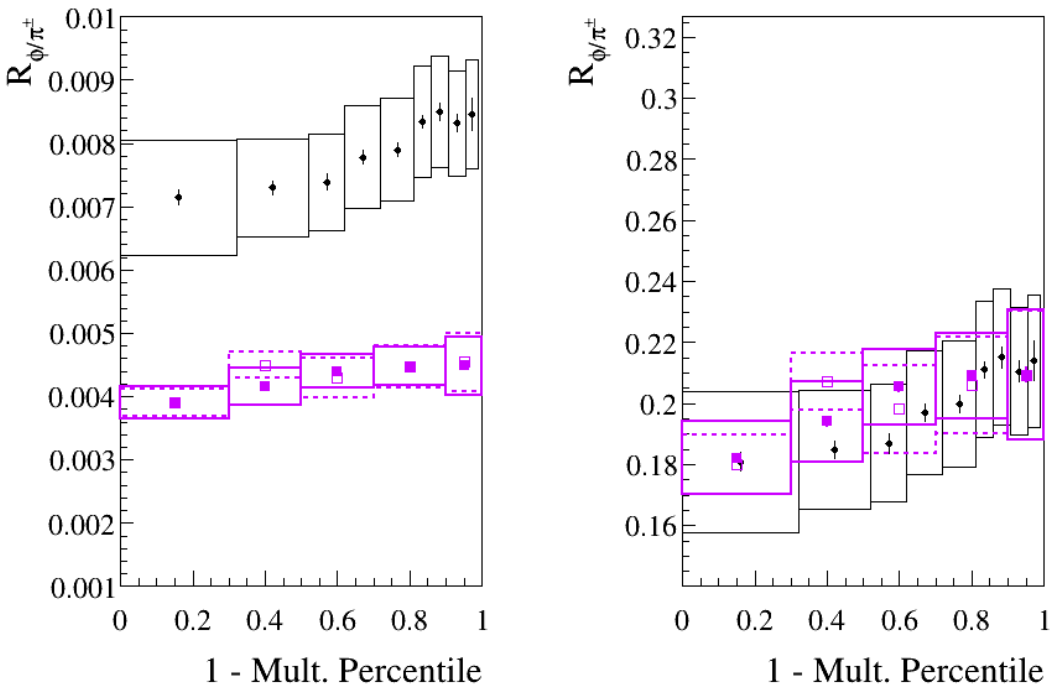


Figure F.4: Absolute (left) and normalized (right) multiplicity-dependent (Cyan) $\frac{\phi}{\pi^{+}+\pi^{-}}$ yield ratios with respect to multiplicity percentile. Results with respect to N_{BACK} (solid, filled) and N_{VELO} (open, dashed) are provided along with results from ALICE(15) (Black) in pp collisions at $\sqrt{s} = 7$ TeV. Charged track density and average event activity is increasing from left to right.

BIBLIOGRAPHY

[1] S. Navas *et al.*, "Review of Particle Physics," *Phys. Rev. D*, vol. 110, p. 030001, Aug 2024.

[2] P. Senger, *The Compressed Baryonic Matter Experiment at FAIR.* Fair UK meeting talks, Jan 2006.

[3] R. Kumar *et al.*, "Theoretical and experimental constraints for the equation of state of dense and hot matter," *Living Reviews in Relativity*, vol. 27, June 2024.

[4] R. Aaij *et al.*, "Centrality determination in heavy-ion collisions with the LHCb detector," *JINST*, vol. 17, no. 05, p. P05009, 2022.

[5] M. L. Miller, K. Reygers, S. J. Sanders, and P. Steinberg, "Glauber modeling in high-energy nuclear collisions," *Annual Review of Nuclear and Particle Science*, vol. 57, p. 205–243, Nov. 2007.

[6] T. Niida and Y. Miake, "Signatures of QGP at RHIC and the LHC," *AAPPS Bull.*, vol. 31, no. 1, p. 12, 2021.

[7] T. Sakaguchi, "Overview of latest results from PHENIX," *PoS*, vol. HardProbes2018, p. 035, 2019.

[8] B. Abelev *et al.*, "Centrality Dependence of Charged Particle Production at Large Transverse Momentum in Pb–Pb Collisions at $\sqrt{s_{\rm NN}} = 2.76$ TeV," *Phys. Lett. B*, vol. 720, pp. 52–62, 2013.

[9] G. Bencedi, "Nuclear modification factor of charged particles and light-flavour hadrons in p-Pb collisions measured by ALICE," in *51st Rencontres de Moriond on QCD and High Energy Interactions*, pp. 285–288, 9 2016.

[10] J. Rafelski and B. Muller, "Strangeness Production in the Quark - Gluon Plasma," *Phys. Rev. Lett.*, vol. 48, p. 1066, 1982. [Erratum: Phys.Rev.Lett. 56, 2334 (1986)].

[11] C. Bierlich and J. R. Christiansen, "Effects of color reconnection on hadron flavor observables," *Phys. Rev. D*, vol. 92, no. 9, p. 094010, 2015.

[12] J. Adam *et al.*, "Enhanced production of multi-strange hadrons in high-multiplicity proton-proton collisions," *Nature Phys.*, vol. 13, pp. 535–539, 2017.

[13] R. Aaij *et al.*, "Evidence for modification of b quark hadronization in high-multiplicity pp collisions at $\sqrt{s} = 13$ TeV," *Phys. Rev. Lett.*, vol. 131, p. 061901, 2023.

[14] R. Aaij *et al.*, "Observation of strangeness enhancement with charmed mesons in high-multiplicity pPb collisions at $\sqrt{s_{\rm NN}} = 8.16$ TeV," *Phys. Rev. D*, vol. 110, p. L031105, Aug 2024.

[15] S. Acharya *et al.*, "Measurement of prompt $\rm D^0$, $\rm D^+$, $\rm D^{*+}$, and $\rm D_S^+$ production in p–Pb collisions at $\sqrt{\rm s_{NN}} = 5.02$ TeV," *JHEP*, vol. 12, p. 092, 2019.

[16] S. Acharya *et al.*, "Measurement of $\rm D^0$, $\rm D^+$, $\rm D^{*+}$ and $\rm D_s^+$ production in Pb-Pb collisions at $\sqrt{\rm s_{NN}} = 5.02$ TeV," *JHEP*, vol. 10, p. 174, 2018.

[17] R. Aaij *et al.*, "Measurements of prompt charm production cross-sections in pp collisions at $\sqrt{s} = 5$ TeV," *JHEP*, vol. 06, p. 147, 2017.

[18] S. Acharya *et al.*, "Charm production and fragmentation fractions at midrapidity in pp collisions at $\sqrt{\rm s} = 13$ TeV," *JHEP*, vol. 12, p. 086, 2023.

[19] M. Lisovyi, A. Verbytskyi, and O. Zenaiev, "Combined analysis of charm-quark fragmentation-fraction measurements," *Eur. Phys. J. C*, vol. 76, no. 7, p. 397, 2016.

[20] J. Adam *et al.*, "First measurement of Λ_c baryon production in Au+Au collisions at $\sqrt{s_{\rm NN}} = 200$ GeV," *Phys. Rev. Lett.*, vol. 124, no. 17, p. 172301, 2020.

[21] R. Aaij *et al.*, "Enhanced Production of Λ_b^0 Baryons in High-Multiplicity pp Collisions at $\sqrt{s} = 13$ TeV," *Phys. Rev. Lett.*, vol. 132, p. 081901, Feb 2024.

[22] Y. S. Amhis *et al.*, "Averages of b-hadron, c-hadron, and τ-lepton properties as of 2018," *Eur. Phys. J. C*, vol. 81, no. 3, p. 226, 2021.

[23] A. Adare *et al.*, "Spectra and ratios of identified particles in Au+Au and d+Au collisions at $\sqrt{s_{NN}} = 200$ GeV," *Phys. Rev. C*, vol. 88, p. 024906, Aug 2013.

[24] LHCb Collaboration, "LHCb Detector Performance," *International Journal of Modern Physics A*, vol. 30, p. 1530022, Mar 2015.

[25] R. Aaij *et al.*, "Performance of the LHCb Vertex Locator," *JINST*, vol. 9, p. P09007, 2014.

[26] "Framework TDR for the LHCb Upgrade II: Opportunities in flavour physics, and beyond, in the HL-LHC era," 2021.

[27] M. Adinolfi *et al.*, "Performance of the LHCb RICH detector at the LHC," *Eur. Phys. J. C*, vol. 73, p. 2431, 2013.

[28] R. Aaij *et al.*, "The LHCb Upgrade I," *JINST*, vol. 19, no. 05, p. P05065, 2024.

[29] B. Pietrzyk, "End of successful proton-proton collision data taking period," Oct 2024. URL: https://lhcb-outreach.web.cern.ch/2024/10/18/end-of-successful-proton-proton-collision-data-taking-period/.

[30] C. Abellan Beteta *et al.*, "Monitoring radiation damage in the LHCb Tracker Turicensis," *JINST*, vol. 15, no. 08, p. P08016, 2020.

[31] C. Abellan Beteta, "Progress on the Upstream Tracker Electronics for the LHCb Upgrade," *Springer Proc. Phys.*, vol. 213, pp. 390–394, 2018.

[32] D. W. Scott, *Multivariate density estimation: Theory, practice, and visualization*. Wiley, 1992.

[33] K. S. Cranmer, "Kernel estimation in high-energy physics," *Comput. Phys. Commun.*, vol. 136, pp. 198–207, 2001.

[34] B. Jann, "KDENS: Stata module for univariate kernel density estimation." Statistical Software Components, Boston College Department of Economics, Oct. 2005.

[35] W. K. Härdle, M. Müller, S. Sperlich, and A. Werwatz, *Nonparametric and Semiparametric Models*. 01 2006.

[36] I. G. Arsene *et al.*, "Rapidity dependence of the proton-to-pion ratio in Au+Au and p+p collisions at s(NN)**(1/2) = 62.4-GeV and 200-GeV," *Phys. Lett. B*, vol. 684, pp. 22–27, 2010.

[37] C. Bierlich, S. Chakraborty, G. Gustafson, and L. Lönnblad, "Strangeness enhancement across collision systems without a plasma," *Physics Letters B*, vol. 835, p. 137571, 2022.

[38] D. J. Gross and F. Wilczek, "Ultraviolet Behavior of Non-Abelian Gauge Theories," *Phys. Rev. Lett.*, vol. 30, pp. 1343–1346, Jun 1973.

[39] H. D. Politzer, "Reliable Perturbative Results for Strong Interactions?," *Phys. Rev. Lett.*, vol. 30, pp. 1346–1349, Jun 1973.

[40] B. Andersson, G. Gustafson, and B. Soderberg, "A General Model for Jet Fragmentation," *Z. Phys. C*, vol. 20, p. 317, 1983.

[41] B. Andersson, G. Gustafson, and B. Nilsson-Almqvist, "A Model for Low p(t) Hadronic Reactions, with Generalizations to Hadron - Nucleus and Nucleus-Nucleus Collisions," *Nucl. Phys. B*, vol. 281, pp. 289–309, 1987.

[42] R. Hagedorn, "Statistical thermodynamics of strong interactions at high-energies," *Nuovo Cim. Suppl.*, vol. 3, pp. 147–186, 1965.

[43] R. Hagedorn and J. Rafelski, "From Hadron Gas to Quark Matter. 1.," in *International Conference on Nuclear Physics*, pp. 237–251, 9 1980.

[44] R. J. Glauber, *Lectures in Theoretical Physics: Lectures Delivered at the Summer Institute for Theoretical Physics, University of Colorado, Boulder*. No. v. 1 in Lectures in Theoretical Physics: Lectures Delivered at the Summer Institute for Theoretical Physics, University of Colorado, Boulder, Interscience, 1958.

[45] J. Rafelski, "Discovery of Quark-Gluon-Plasma: Strangeness Diaries," *Eur. Phys. J. ST*, vol. 229, no. 1, pp. 1–140, 2020.

[46] J. Rafelski, "Strangeness Production in the Quark Gluon Plasma," *Nucl. Phys. A*, vol. 418, pp. 215C–235C, 1984.

[47] J. Rafelski, "Redistribution of Strangeness Between Quark - Gluon Plasma and Hadronic Gas," *Phys. Lett. B*, vol. 190, pp. 167–172, 1987.

[48] M. Jacob and J. Tran Thanh Van, "Quark matter formation and heavy ion collisions: A general review and status report," *Physics Reports*, vol. 88, no. 5, pp. 321–413, 1982.

[49] F. Becattini and L. Ferroni, "Statistical hadronization and hadronic microcanonical ensemble. 2.," *Eur. Phys. J. C*, vol. 38, pp. 225–246, 2004. [Erratum: Eur.Phys.J. 66, 341 (2010)].

[50] T. Biro and J. Zimanyi, "Quarkochemistry in Relativistic Heavy Ion Collisions," *Phys. Lett. B*, vol. 113, p. 6, 1982.

[51] I. Montvay and J. Zimanyi, "Hadron Chemistry in Heavy Ion Collisions," *Nucl. Phys. A*, vol. 316, p. 490, 1979.

[52] J. Rafelski and R. Hagedorn, "From Hadron Gas to Quark Matter. 2.," in *International Symposium on Statistical Mechanics of Quarks and Hadrons*, 10 1980.

[53] P. Koch, B. Muller, and J. Rafelski, "Strangeness Production and Evolution in Quark Gluon Plasma," *Z. Phys. A*, vol. 324, pp. 453–463, 1986.

[54] R. Baier, Y. L. Dokshitzer, A. H. Mueller, and D. Schiff, "Radiative energy loss of high energy partons traversing an expanding QCD plasma," *Phys. Rev. C*, vol. 58, pp. 1706–1713, Sep 1998.

[55] X.-N. Wang, "Effect of jet quenching on high p_T hadron spectra in high-energy nuclear collisions," *Phys. Rev. C*, vol. 58, p. 2321, 1998.

[56] X.-N. Wang, *The Myth of Large P_t Hadron Spectra in High-Energy Heavy-Ion Collisions*, pp. 241–252. Boston, MA: Springer US, 1999.

[57] R. Baier, D. Schiff, and B. G. Zakharov, "Energy loss in perturbative QCD," *Ann. Rev. Nucl. Part. Sci.*, vol. 50, pp. 37–69, 2000.

[58] S. S. Adler *et al.*, "Suppressed π^0 production at large transverse momentum in central Au+ Au collisions at $\sqrt{s_{NN}} = 200$ GeV," *Phys. Rev. Lett.*, vol. 91, p. 072301, 2003.

[59] S. Acharya *et al.*, "Constraining hadronization mechanisms with Λ_c^+/D^0 production ratios in Pb–Pb collisions at $\sqrt{s_{NN}}$=5.02 TeV," *Phys. Lett. B*, vol. 839, p. 137796, 2023.

[60] T. S. Biro, H. B. Nielsen, and J. Knoll, "Color Rope Model for Extreme Relativistic Heavy Ion Collisions," *Nucl. Phys. B*, vol. 245, pp. 449–468, 1984.

[61] C. Bierlich, S. Chakraborty, G. Gustafson, and L. Lönnblad, "Jet modifications from colour rope formation in dense systems of non-parallel strings," *SciPost Phys.*, vol. 13, p. 023, 2022.

[62] C. Bierlich, G. Gustafson, L. Lönnblad, and A. Tarasov, "Effects of Overlapping Strings in pp Collisions," *JHEP*, vol. 03, p. 148, 2015.

[63] J. R. Christiansen and P. Z. Skands, "String Formation Beyond Leading Colour," *JHEP*, vol. 08, p. 003, 2015.

[64] Y. Kanakubo, Y. Tachibana, and T. Hirano, "Unified description of hadron yield ratios from dynamical core-corona initialization," *Phys. Rev. C*, vol. 101, no. 2, p. 024912, 2020.

[65] K. Werner, "Core-corona procedure and microcanonical hadronization to understand strangeness enhancement in proton-proton and heavy ion collisions in the EPOS4 framework," *Phys. Rev. C*, vol. 109, no. 1, p. 014910, 2024.

[66] V. Minissale, F. Scardina, and V. Greco, "Hadrons from coalescence plus fragmentation in AA collisions at energies available at the BNL Relativistic Heavy Ion Collider to the CERN Large Hadron Collider," *Phys. Rev. C*, vol. 92, no. 5, p. 054904, 2015.

[67] R. J. Fries, B. Muller, C. Nonaka, and S. A. Bass, "Hadron production in heavy ion collisions: Fragmentation and recombination from a dense parton phase," *Phys. Rev. C*, vol. 68, p. 044902, 2003.

[68] R. J. Fries, V. Greco, and P. Sorensen, "Coalescence Models For Hadron Formation From Quark Gluon Plasma," *Ann. Rev. Nucl. Part. Sci.*, vol. 58, pp. 177–205, 2008.

[69] M. Aaboud *et al.*, "Measurement of the nuclear modification factor for inclusive jets in Pb+Pb collisions at $\sqrt{s_{\mathrm{NN}}} = 5.02$ TeV with the ATLAS detector," *Phys. Lett. B*, vol. 790, pp. 108–128, 2019.

[70] G. Aad *et al.*, "Medium-Induced Modification of Z-Tagged Charged Particle Yields in $Pb + Pb$ Collisions at 5.02 TeV with the ATLAS Detector," *Phys. Rev. Lett.*, vol. 126, no. 7, p. 072301, 2021.

[71] S. Acharya *et al.*, "Constraints on jet quenching in p-Pb collisions at $\sqrt{\mathbf{s_{NN}}} = 5.02$ TeV measured by the event-activity dependence of semi-inclusive hadron-jet distributions," *Phys. Lett. B*, vol. 783, pp. 95–113, 2018.

[72] R. Aaij *et al.*, "Precise measurement of the f_s/f_d ratio of fragmentation fractions and of B^0_s decay branching fractions," *Phys. Rev. D*, vol. 104, no. 3, p. 032005, 2021.

[73] O. Callot, *Online Pattern Recognition*, Oct 2004. LHCb-2004-094, CERN-LHCb-2004-094.

[74] C. Bierlich *et al.*, "A comprehensive guide to the physics and usage of PYTHIA 8.3," *SciPost Phys. Codeb.*, vol. 2022, p. 8, 2022.

[75] C. Bierlich, G. Gustafson, L. Lönnblad, and H. Shah, "The Angantyr model for Heavy-Ion Collisions in PYTHIA8," *JHEP*, vol. 10, p. 134, 2018.

[76] I. Arsene *et al.*, "Production of mesons and baryons at high rapidity and high P(T) in proton-proton collisions at s**(1/2) = 200-GeV," *Phys. Rev. Lett.*, vol. 98, p. 252001, 2007.

[77] I. G. Bearden *et al.*, "Forward and midrapidity like-particle ratios from p + p collisions at $\sqrt{s}$ = 200-GeV," *Phys. Lett. B*, vol. 607, pp. 42–50, 2005.

[78] I. G. Bearden *et al.*, "Rapidity Dependence of Charged Antiparticle-to-Particle Ratios in Au+Au Collisions at $\sqrt{s_{NN}} = 200$ GeV," *Phys. Rev. Lett.*, vol. 90, p. 102301, 2003.